Lehigh University
Lehigh Preserve

Theses and Dissertations

2018

Investigation of Wear Mechanism of Gallium Nitride

Guosong Zeng
Lehigh University

Follow this and additional works at: https://preserve.lehigh.edu/etd

Part of the Mechanical Engineering Commons

Recommended Citation

Zeng, Guosong, "Investigation of Wear Mechanism of Gallium Nitride" (2018). *Theses and Dissertations*. 2995.
https://preserve.lehigh.edu/etd/2995

This Dissertation is brought to you for free and open access by Lehigh Preserve. It has been accepted for inclusion in Theses and Dissertations by an authorized administrator of Lehigh Preserve. For more information, please contact preserve@lehigh.edu.

Investigation of Wear Mechanism of Gallium Nitride

by

Guosong Zeng

Presented to the Graduate and Research Committee

of Lehigh University

in Candidacy for the Degree of

Doctor of Philosophy

in

Mechanical Engineering

Lehigh University

January 2018

Copyright by Guosong Zeng

2018

Approved and recommended for acceptance as a dissertation in partial fulfillment of the requirements for the degree of Doctor of Philosophy.

Date

Accepted Date

Committee Members:

Primary advisor: Dr. Brandon Krick, Mechanical Engineering and Mechanics

Co-advisor: Dr. Nelson Tansu, Electrical Engineering and Computer

Dr. Herman Nied, Mechanical Engineering and Mechanics

Dr. Edmund Webb, Mechanical Engineering and Mechanics

Dr. Richard Vinci, Materials Science and Engineering

Acknowledgements

I want to thank Nelson Tansu to bring me into this III-Nitrides world. I still remember the first time we met, you asked me why not try the wear measurement of GaN? Then I started my almost three years PhD study of tribological properties of III-Nitrides. This is an astounding adventure to witness each single exciting finding coming up from these amazing materials. I'm really appreciate that you opened up the door for me and let me get into the world of III-Nitrides.

I would like to thank Xiaofang Yang and Bruce Koel. Both of you are very talented, knowledgeable and responsible. And your rigorous attitudes on research teach me what the real scientist should look like. Furthermore, the chance of working with Dr. Koel and Dr. Yang let me accumulate tremendous experience and knowledge in surface science and some advanced characterizations techniques.

I would like to thank Richard Vinci for your kindly help in my research. I still remember that at the very beginning, it was you who spent a lot of time finding diamond tips for my experiments. It is also you who set up the independent study of SEM, trained me and eventually let me become proficient in operating electron microscopes. All the skillsets in characterization techniques eventually lead to several important discoveries in my research.

I would like to thank Edmund Webb for your time and effort in MD simulation and taught me an excellent class of FEA. All the knowledge I got from you directly contributes to my research of GaN and even other projects.

I would like to thank Herman Nied. As my master advisor, I gained necessary background in MEMS and FEA from him. It was also you who strongly recommended me to my PhD advisor and let me have this precious opportunity to get into the tribology world.

I would like to thank Chee-Keong Tan and Damir Borovac for helping me running DFT simulations. I would like to thank Wei Sun and Renbo Song for the sample growth. I want to express my appreciation to Justin Goodrich, who spent lot of time helping me with proofreading of my thesis. I would like to thank Yijie Jiang, Kevin Turner, and Lisa Mariani for their kindly help in nanoindentation training. I would like to thank Chris Marvel for the ARM experiment. I would like to thank William Mushock and Robert Keyse for their training on SEM, FIB and TEM. I appreciate your patient in answering my numerous questions so that I can well understand all these amazing techniques. I would like to thank Nick Strandwitz, Gregory Sawyer, Robert Carpick, Chris Junk, for their kindly discussions on my research. All your valuable opinions not only help me to better understand the newly discovered phenomena, but also directly contribute to the development of the hypothesis in explaining them.

I want to thank my dear friends Mark Sidebottom, John Curry, Haolin Ma, Wei Sun, Chee-Keong Tan, Ling Ju, for all your supports, comfort, help, as well as countless suggestions. Without your companion, I won't be able to get through my PhD study.

I would give a special acknowledgement to my family, my parents, Senrong Zeng and Yuxiu Nie, and my wife Mengni Cao, who have been wonderfully supportive throughout my entire education. My parents are my first teachers in my life, and let me become passionate in science when I was a little boy. Although, both of you are not highly educated, you still keep reminding me how important the knowledge is. You always cheer up with me for any little achievement I have made, and hide the bad news from me to let me stay in a quiet environment and focus on my work. Thank you so much my Mom and Dad for all the sacrifices you have made in the past years. To me, you are the best parents in the world. Mengni, for the past six years, I really appreciate your companion with me. Every time when I'm facing so many difficulties, you always get my back, encourage me, and solve the problem with me. I will remember all the moments that you try your best to make me laugh and let me feel less stressful. I will also remember all your admonishments and criticisms on me, which makes me become humble, persistent, determined and strong person. It is your selfless support and love that drive me to overcome all the challenges and difficulties, and eventually achieve my goal.

My last acknowledgement, I will give it to my advisor Brandon Krick, he is not only my advisor, but also my friend and my example. He is a great mentor to teach me how to become a successful researcher, how to enjoy the research, and how to become a real man. Thanks to his tireless efforts, we can have this research continued, and eventually results in some exciting publications. Beside research, he also teaches me a lot in my life, my first hiking, my first rafting, my golf, my first road trip in the states, *etc*. All these experiences with him show me, enjoying the life is also very important. It is you who make me become better and better.

Table of Contents

List of Tables

List of Figures

Abstract

The optoelectronic properties of gallium nitride (GaN) has been extensively studied for decades, which has facilitated its application in many different areas, cementing it as one of the most important semiconductor materials in the world. However, in comparison to the study of its optoelectronic properties, there are few studies of its mechanical properties - especially the tribological performance. Knowing the tribological properties of GaN, such as friction and wear, is crucial for understanding its machinability, the implementation of GaN in MEMS, solar cells, and other devices, as well as the wear performance of these GaN-based devices when working under harsh environments. In our study, we reveal that GaN has an ultralow wear nature, and that its wear rate can approach that of diamond. We also discover that the wear rate of GaN is affected by its crystallographic orientation, humidity, and composition.

For the crystallographic orientation dependence, we look into the physics by both experimental and computational methods. We demonstrate that both the friction coefficient and wear rate of GaN exhibits a 60° periodicity. We conclude that these periodic variations of wear rate and friction coefficient are the results of a periodic variation of the energy barrier.

The moisture dependent wear mechanism of GaN has been investigated under dry, low humidity, and high humidity environments. The results show that the wear rate of GaN perfectly follows an increasing of the humidity which spans over two orders of magnitude when the testing environment switches from dry nitrogen to humid lab air. On the contrary, the friction coefficient gave a contrary response, i.e., the lowest friction coefficient was found under low humidity environment, dry nitrogen had the highest friction coefficient,

and the humid environment had its friction in the middle. Various characterization techniques, including SEM/EDS, AFM and TEM were employed to interrogate the worn surfaces under each condition. Based on the results, we hypothesize that the wear under dry nitrogen environment is adhesive in nature whereas grooving abrasive wear dominates the wear behavior of GaN under a humid environment.

The compositional study of GaN wear revealed that by alloying different elements into the GaN system, one can not only tune the bandgap, but also modify the wear rate. This finding can be useful for applications and design that require suitable electronic properties while keep the wear rate within an acceptable range.

Furthermore, during the investigation of the GaN wear mechanism, we discovered that the tribological sliding can also alter the surface band bending of this material. Our results demonstrate that the environment, number of sliding cycles, and normal loads can effectively tune the surface band bending of GaN. This finding shows the capability of mechanical dynamic contact for surface electronic property modification, which can be used in various applications, such as gas sensing, photocatalysis, and photochemistry.

Understanding of the wear mechanism of GaN as well as the shear-induced band bending on GaN can remarkably promote the applications of GaN in various fields other than the optoelectronic area. This also reinforces the important message that tribology is not only a discipline that focuses on investigation of protective coating and lubrication but also can be used in device design and fabrication.

1 Introduction

1.1 Materials Tribology

Friction can be defined as the force resisting the relative motion between two surfaces. These two surfaces can either be solid/liquid, solid/gas or liquid/gas. The frictional force is a non-conservative force. This means it can convert the kinetic energy of two materials which are in relative motion into heat or other forms of energy. When the surfaces of these two materials are in contact, another type of force is engendered, which is called adhesion. Adhesion occurs because of the formation of bonds across the interface. In general, this bonding is very weak, consisting of the van der Waals force, electrostatic force, etc. Once the friction starts, lattices at the contact surface of both materials is displaced, but no material is lost. With proceeding of friction, defects accumulate, bonds are ruptured by shear, and material from the weakened side is either transferred to the mating side or spread away as wear debris. These friction, adhesion, and wear properties are the major aspects that tribology focuses on.

The terminology “tribology” first came up in “The Jost Report” in 1966 by Dr. H. Peter Jost [1]. It is derived from the Greek root “tribo”, which means “rubbing”. Tribology is defined as the study of the interaction between two or more surfaces in relative motion, including the investigations of friction, wear and lubrication. In this renowned report, Dr. Jost suggests that the wastage of resources due to inappropriate frictional designs could be as high as 6% of the GDP. Table 1 shows the potential savings by correct uses of tribological design [2].

Because of this economic demand, increasing attention has been allocated to accelerate the development of tribology. Nowadays, tribology is not only limited to macroscale friction and wear issues, but also extends to a lot of different areas, such as nanotribology (atomic force microscopy, micro/nanoelectromechanical systems, etc.), biotribology (human joint prosthetics, etc.) and green tribology [3]. Thus, tribology is becoming an interdisciplinary area of mechanical engineering, material science, electrical engineering, physics, chemistry, and bioengineering. It spans the studies of physical and chemical properties of materials and it has a wide range of applications in as aerospace, automotive, medical, energy, etc.

Table 1-1 Potential savings by correct uses of tribological design (unit is billion US dollars), World Factbook (2008) [2]

Country or region	Euro	United States	China	Japan	Germany	France	U. K.
Potential saving	303	186	68	63	50	48	36

Materials tribology, as suggested by its name, focuses on the study of the tribological performance of materials, linking the length scales from macroscale to microscale or even nanoscale. Pin-on-disk and flat-on-flat are two common configurations that are widely applied in this field to investigate the tribological behaviors and properties. Wear rate and friction coefficient are not intrinsic material properties but system properties. By employing different countersample to slide against the testing sample, different tribological behaviors will be revealed, due to different tribochemistry occurring between the two surfaces. Materials tribology provides an alternative method to study the surface chemistry dynamically as opposed to traditional static chemistry studies.

The current grand challenges in the materials tribology community are 1) how to link the experiment scales to nano/molecular scale and 2) how to understand molecular origins of friction and wear. To answer these questions, single crystal materials are the best candidates. Their lattice structures have been extensively studied for decades and the perfect periodic lattice structures allow the use of relatively simplistic models. In this study, we investigate the wear mechanism of single crystal gallium nitride (GaN) and attempt to understand how material composition, lattice structure/crystal orientation, and surface chemistry will affect its wear performance as well as how the stress will influence its surface charge properties (*i.e.*, tunable Fermi level and surface band bending).

1.2 Background of III-Nitrides

In 2014, the Nobel Prize in Physics was awarded to Nakamura, Amano, and Akasaki for their remarkable contribution in discovering blue LEDs [4]. As the key material in blue LEDs, GaN and related ternary composites have received more and more focus in the past two decades. The prevalence of GaN in scientific research as well as in industry has expanded rapidly in recent years due to its remarkable optoelectronic properties [5]–[10], *e.g.*, its large band gap, high breakdown voltage, wide transmission bandwidth, high electron mobility, high thermal stability, high chemical stability, and high thermal conductivity. The progress in GaN-based semiconductors devices was driven by the fast development of material epitaxy techniques while device innovations enabled the wide implementation of III-Nitrides in power electronics [5], solid state lighting technologies [6]–[9], *etc*.

1.2.1 Optoelectronic Properties of III-Nitrides

The bandgap of GaN is determined by photoluminescence (PL) measurements of its exciton lines [11]–[13]. More investigations in determining the transition energy of an exciton near T = 0 K have been done since 1990s and the results indicated a temperature dependence of the bandgap of GaN [14], [15]. By employing photoreflectance measurement and theoretical calculation, Shikanai et al. found a strain dependence of exciton resonance energy in GaN [16]. Furthermore, this energy gap property is also highly dependent on the epilayer thickness. By conducting an X-ray reciprocal space mapping (RSM), the author demonstrated that the strain varied significantly with depth while the RBS study revealed that the indium content increased along the growth direction [17]. This epilayer thickness dependency has also been confirmed by [18]. Castaldini et al. reported that the thinner GaN epilayer grown on sapphire had a higher density of recombining defects and a consequent reduction of reverse current density. This epilayer thickness dependence was attributed to strain. Moreover, the strain generated by lattice mismatch between the substrate and the GaN epilayer not only affects the energy gap but also induces a polarization field. This polarization field will influence the potential profile and result in a redshift, which is the so-called quantum-confined Stark effect (QCSE). Thus, the study of strain relaxation is crucial for understanding optical performance of GaN/InGaN-based quantum wells. Bai et al. employed XRD and low-temperature photoluminescence to study the strain relaxation and link it to the number of quantum wells in InGaN/GaN multiple quantum well (MQW) structures. The results showed that the strain in InGaN/GaN MQW structure started to relax with three periods and as the number of quantum well period increases a clear shift was observed [19]. Nonlinear pyroelectric polarization of wurtzite AlGaN/GaN heterostructures and quantum wells has been studied in [20]. The author provided an improved theory to calculate the spontaneous and piezoelectric polarization in nitride alloys. They found that when the polarization nonlinearity was taken into account, the discrepancies between *ab initio* calculation and experiments were reduced. A modified staggered InGaN MQW structure with step-function-like indium content has been proposed. The theoretical analysis and experimental results indicated that the recombination rate and optical gain could be improved dramatically when compared to traditional InGaN MQW [21], [22].

1.2.2 Surface Properties of III-Nitrides

1.2.2.1 Surface Chemistry

Since the atoms at the surface interrupt the periodicity of the lattice, those unfilled dangling bonds make the surface different from the material inside the bulk system. Surface state, lattice reconstruction, physisorption and chemisorption, band bending, etc., are all caused by the missing half of atoms at the surface. All these processes make the material exhibit different chemical properties, which can be beneficial in chemical sensing devices, photocatalysis, photochemistry, solar cell, to name a few [23]–[27]. The surface chemistry of III-Nitride semiconductors is an important aspect that continues to attract more and more attentions. All the designs and optimizations of III-Nitrides-based gas sensors and electronic components (e.g., HEMTs) will benefit from further understanding the surface chemistry.

One of the important aspects of studying surface property is the oxidation of GaN. GaN is a chemically inert material which is difficult to oxidize. Researchers continue to find less than a nanometer native oxide on the surface [28]–[30]. Knowing the susceptibility of GaN to oxidation under various conditions will enable its extension in different areas along with preventing the oxidation effect on device performance [31]–[34]. Yellow luminescence (YL) of GaN is another interesting phenomenon that attracts a lot of attention from researchers. Although it is still under debate what is the main effect giving rise to the YL, i.e., midgap states or surface oxide layer, some groups have already demonstrated the capability of using YL as an indicator to monitor the removal of oxides from GaN films [32]. The surface chemistry and electronic properties influenced by oxide and orientation have been reported along with this YL emission. Results from [35]–[37] indicate that the oxide concentration will vary the Fermi level of GaN and ammonia has been demonstrated to be a good etchant for oxide removal. Chemisorption is another favorite topic of surface researchers in nitrides area. Chemisorptions of various species, like water, oxygen, ammonia, pyrroline, aniline, octanethiol, etc., were studied by surface sensitive characterization techniques, including AES, XPS, ELS, SPV and so on [29], [38]–[46] as well as their interactions at the interface have been analyzed [27].

1.2.2.2 Surface Charge Property

Schottky and Mott first came up with the concept of band bending to explain the rectifying effect of metal-semiconductor contacts [47]–[49]. When two materials (metal and semiconductor) are in contact with each other, the Fermi level of the semiconductor will line up with the metal work function, which results in the generation of an electric field at the interface and bending of the electronic bands. Besides metal-semiconductor contact, several other methods and effects can also induce band bending, including the surface states of semiconductor [50], [51], molecular adsorption [52], doping [23], [53]–[56], and external electric fields [57]–[59]. Being able to tune the band bending at the surface or interface of semiconductor materials allows the generated electric field to assist in the accumulation of electrons (upward band bending) or holes (downward band bending), which can benefit the surface redox reaction in applications such as gas/chemical sensing. Furthermore, with the presence of electric field, the recombination of photoinduced electron-hole pair will be suppressed and more electrons and holes will be available at the surface or interface for further photochemical reaction. In this regard, the capability of effectively tuning the degree of band bending is promising in many applications, such as photocatalysis, photochemistry, sunlight harvesting, metal oxidation/encapsulation, etc. For these reasons more effort has been put into this area to finely control the band bending for specific applications.

Onishi et al. studied electronic states and chemisorption properties of the TiO_2 (441) surface with various adsorbates and compared to the TiO_2 (110) surface[60]. Results showed that small amount of Ti^{3+} species were found at the TiO_2 (441) surface and gave rise to the downward band bending. Different molecules (CH_3OH, HCOOH and SO_2) were introduced to the surface and chemisorption of these molecules was confirmed. This electron acceptor molecule induced downward band bending was confirmed by Zhao through DFT calculation [61]. Chemisorption of electron donor molecules, such as O_2, leading to upward band bending was also observed [62]–[64]. Extensive work has been done to understand how band bending influences molecule adsorption on semiconductor the surface [52], [65]–[68]. Tremendous efforts have also been put towards achieving GaN-based sensors for achieving chemical and biological sensing [69], such as benzene and aromatic compounds [70], [71], ammonia [72]–[74], methane [75], [76], hydrogen and hydrocarbons [77]–[84], oxygen [10], carbonic oxide

[79], [85], botulinum toxin [86], [87]. By changing the dopants and concentrations, surface treatment, and/or decorating the surface with various nanostructures, surface Fermi level tuning can be realized to achieve high H_2/O_2 evolution efficiency in photoelectrochemical (PEC) water splitting. Kibria et al. [23] reported a tunable surface Fermi level of GaN nanowires by controlling the Mg-dopant incorporation (*i.e.*, tuning the Mg effusion cell temperature). On the contrary, AlOtaibi et al. doped Si into GaN nanowires to tune the Fermi level in order to reduce the surface depletion region [56]. Nanostructures formed by Rh/Cr_2O_3 has also been incorporated into GaN surfaces for unpinning the bands at the interface of GaN/cocatalyst. This provides more reaction sites as well as improving efficiency of electron transport and transfer [54], [88]. Caliskan et al. employed XPS to visualize the band bending of GaN with different doping types (unintentionally doped, n-doped, and p-doped) [53]. With different treatments of GaN surface, Lin et al. showed that the obtained nitrogen-related-vacancy defects can alter the Fermi level pinning, which results in different degrees of surface band bending [89]. Kim et al [90] performed UV/O_3 pretreatment on GaN surface before depositing ALD-Al_2O_3 thin films and successfully tuned the band bending at the GaN/ Al_2O_3 interface. Semiconductor nanoparticles have been widely used to induce photochemical process. The properties of nanoparticles also affect the surface band bending in photochemistry and photocatalysis [91], [92]. Zhang et al. studied the effect of particle size on the dynamics of electron-hole pair recombination process [93]. They found that the particle size of nanocrystalline TiO_2 influenced the dopant concentration as well as the optimal doping level, which in turn affected the photonic efficiency. Surface state-induced band bending originates from the termination of the periodic

lattice structure. The dangling bonds at the surface interact with each other to form a narrower energy band. Since the surface states are in general orders of magnitude larger than the defect states/doping levels in the bulk, Fermi level pinning will occur and cause band bending at the surface [47]. Likewise, different orientations will also lead to different interaction manners of those unpaired electrons in the dangling bonds at the surface, which gives rise to different degree of bending of the energy bands. Mishra et al. compared the surface band bending of nonpolar (a-GaN/r-sapphire) and polar (c-GaN/c-sapphire) GaN coatings and found that the core levels as well as valence band spectra were shifted due to this polarization [35]. Kislov et al investigated the orientation dependence of photoactivity of ZnO and reported that oxygen terminated $(000\bar{1})$-ZnO was the only surface that exhibited a strong photoactivity while (0001)-ZnO and $(10\bar{1}0)$-ZnO showed limited dissolution due to the surface defect sites [94]. Nonpolar m-plane GaN has higher reactivity for spontaneous water splitting as well as lower energy barrier for proton diffusion when compared to other crystal planes [23], [55], [95].

Our study reveals that, by applying shear stress, the surface property of GaN can also be altered. This provides us with a new way to achieve surface band bending on semiconductor materials. More details of shear-induced band bending will be discussed in Chapter 7.

1.2.3 Mechanical Properties of III-Nitrides

While the optoelectronic properties of GaN based materials have been widely explored, research into the mechanical properties and performance of GaN has been limited. The elastic constants of GaN have been determined mainly by static displacement methods, X-ray diffraction, resonance ultrasound method, and acoustic wave method [96]–[99], and these parameters have been widely used in lattice mismatch and piezoelectric polarization effect [20], [100], [101]. The Young's modulus (210-330 GPa) and hardness (12-20 GPa) of GaN have been obtained by nanoindentation and bending test on suspended GaN microstructure [102]–[106]. The fracture toughness and yield strength of bulk single crystal GaN were also obtained by indentation and were found to be 0.79 ± 0.1 MPa√m and 15 GPa, respectively [104], [105]. The mechanism of plastic deformation under nanoindentation was also study by Kucheyev, et al. [106]. They found that there was no systematic dependence of mechanical properties of GaN epilayer on both the coating thickness and the doping type and that slip-planes are one of the physical mechanisms responsible for the plastic deformation of GaN. An in-situ micro-compression test has been conducted to extract the deformation parameters of MOVPE grown GaN micro-pillars. Deformation was observed only occurring through 2nd order pyramidal slip on the $\{11\bar{2}2\} < 11\bar{2}3 >$ slip system and measured activation energy for the slip system was determined to be 0.91 ± 0.2eV and the Peierl's stress was 3.76GPa [107]. Study of phase transformation of GaN is another aspect for explaining the change of lattice structure of GaN caused by external mechanical load. High-pressure phase of GaN has been obtained by diamond anvil cell (DAC) within the range of 30-50GPa and this wurtzite to rocksalt phase transition has been determined by Raman spectroscopy, X-ray diffraction and X-ray-absorption spectroscopy [108]–[110]. First principle analysis was also employed to calculate the required pressure for triggering the phase transformation from wurtzite structure to rocksalt structure and the results were constant with the aforementioned experiments

[111], [112]. A Berkovich nanoindentation has been performed on GaN layer and the residual strain field was characterized by Raman mapping [113]. Based on the Raman spectra, no new phase was found after nanoindentation.

Even less is known about the tribological (friction and wear) properties of GaN and GaN based materials (i.e. doped GaN and InGaN). GaN plays a key role in modern semiconductor industry; thus, it is crucial to understand its wear behavior and reliability, especially in MEMS devices, or under some harsh working environments (like space, desert, etc). Moreover, the study of friction and wear of GaN will be very conducive for understanding the machinability of GaN when we refer to the fabrication (ultraprecision machining, wafer grinding, ect.) of GaN-based devices.

Investigations of wear performance and mechanisms of GaN-based materials, is limited to a few studies including nanoscratch [114], chemical mechanical polishing (CMP) of GaN wafers [115]–[125] and our recent papers on the wear of GaN [126]–[130]. Nanoscratch employs single asperity contact to study the scratch hardness, plasticity and fracture of the of GaN, revealing anisotropic scratch hardness [114]. The results indicated that the substrate orientation dominated the extent of ploughing in GaN epilayers and c-axis sapphire-grown GaN epilayer has higher shear resistance than those GaN epilayers grown on a-axis sapphire substrate. However, nanoscratch is generally limited in the context of tribological performance because they are limited to one sliding cycle of a very sharp tip at relatively large contact pressures. CMP focuses on the material removal rate (MRR) with assistance of chemical reaction. The research efforts on CMP of GaN report that, pH [117], concentration [116], size [116], [120] and composition of the abrasive [119], concentration and composition of the catalyst [123], [124], pretreatment [121], [125], process time [115] and surface polarization [117], [118] will influence the MRR, defect density, oxidation, surface roughness, *etc.* of GaN wafer.

In addition to nanoscratch and CMP, our sphere-on-flat tribological studies revealed – for the first time – the ultralow wear performance of GaN semiconductors [126]. In-depth discussion of tribological properties of GaN can be found through Chapter 4 to Chapter 6.

1.3 Motivation

There is a need to understand the surface interactions of such materials, especially their tribological performance and surface chemistry variation under such dynamic contact. One concern in III-Nitride materials is reliable performance when subjected to aging, wear, and erosion in harsh environments, including sand and debris (in desert environments), micrometeroids and vacuum (in the space environment), and water (in humid environments). The immediate impacts of interfacial interactions and tribological performance are rooted in multiple initiatives, including energy, efficiency, sustainability, manufacturing, national defense, nanoscience, electronic and photonic materials, and engineering design. Furthermore, the surface property of GaN, such as early stage of oxide growth, moisture-assisted cracking, etc., can be revealed by means of tribological tests. Understanding of surface chemistry (surface composition, oxidation corrosion, and humidity effect) on GaN will accelerate the optimization of device fabrication process, the understanding of contact formation, the optimization of material growth conditions, etc. However, to our knowledge, there is has been no study of the tribological properties of GaN before this work. Study of these properties will provide us with insight into mechanical and chemical responses of GaN when under external loading or exposed to different environments. Thus, understanding the tribological properties of the GaN will provide a key step towards understanding the mechanical properties of the material for device applications.

1.4 Hypothesis and Research Plan

Our preliminary results reveal that the wear performance of GaN is significantly affected by several factors, including crystallographic direction, environment, composition. Furthermore, the surface charge properties of GaN after tribological sliding is remarkably altered, which indicates a potential way for design and fabrication of III-Nitride-based chemical sensor, photocatalysis device, etc. Understanding the physics and chemistry behind these phenomena will be conducive in the implementation of GaN and other related binary and ternary composites in different areas, as well as assist in the manufacturing and polishing process of III-Nitride-based devices.

Presented are several fundamental questions regarding the aforementioned effects, as well as the corresponding hypothesis and proposed research plan to answer that question. Each question will be addressed independently in its own chapter.

1.4.1 Crystallographic orientation

Question 1:

Does the wear rate of GaN exhibit periodic variation? What causes this directionality?

Hypothesis 1:

MOCVD-grown GaN epilayer has a wurtzite single crystal structure, which makes this material exhibiting anisotropy (60° periodicity) with respect to elasticity, plasticity, hardness and so forth. Since wear rate correlates to hardness to some extent, we can expect directionality to impact the wear rate of GaN. Furthermore, when looking into the lattice structure from the basal plane, the $< 1\bar{2}10 >$ family direction repeats every 60° while the $< 1\bar{1}00 >$ family direction repeats every 120°. This gives rise to another fundamental question: is the periodicity of the wear rate of GaN 60° or 120°?

Proposed Research Plan 1:

Interrogating the crystallographic orientation effect on GaN wear performance will be achieved by both experimental and simulation methods. Linear reciprocating pin-on-disk dry sliding tests will be performed along two different directions to obtain the corresponding wear rates first. Then a rotary pin-on-disk wear test will be conducted to encompass all the directions. Molecular static simulation will be employed to model the free energy variation of the wear debris when moving along different crystal directions. The simulation result will be conducive in understanding the physics behind directionality of GaN wear behavior.

1.4.2 Environmental Dependence

Question 2:

How does moisture interact with GaN surface and how tribochemical reactions change properties of GaN?

Hypothesis 2:

Most of the engineering materials (ceramics, polymers and metals) present environmental dependency of their tribological properties [131]–[152]. Among the numerous possible working environments, moisture is one of the most ubiquitous conditions. Moisture has been reported for decades to have pronounced influence on material wear properties, either in detrimental ways (moisture assisted cracking/water corrosion) or in defensive ways (formation protecting layer). For GaN, we hypothesize that water molecules will split and form hydroxyl groups at the GaN surface. This will lower the surface energy and increase the wear rate of GaN, resulting in a faster rate of material removal.

Proposed Research Plan 2:

In order to reveal the effect of humidity on GaN wear, we will carry out the wear test under different humidity levels. Several advanced characterization techniques, including XPS, AES, FIB, ARM, AFM, and SEM/EDS, will be utilized to examine the worn and unworn surfaces.

1.4.3 Composition

Question 3:

How does different element content affect the wear rate of GaN?

In addition to crystal orientation and environment, composition is another factor that might have markedly influence on GaN wear. In the LED industry alloying indium and aluminum into GaN to form ternary composites is employed to easily tune the bandgap from 0.7 eV (InN) to 6.2 eV (AlN). The hardness will also vary correspondingly, from 3 GPa to 30 GPa [102]–[106], [153]–[155]. Therefore, linking the wear rate and hardness with respect to different In or Al content will provide us with a way to balance the electronic and mechanical properties; in other words, by alloying different elements such as aluminum, boron, or indium with different contents, we can optimize the optoelectronic properties while engineering mechanical properties such as wear rate and hardness into an acceptable range.

Hypothesis 3:

Based on preliminary results, under same testing conditions, the wear rate of GaN is two orders of magnitude higher than InN. We expect that by alloying more In content into GaN film, the wear rate of InGaN will increase correspondingly.

Proposed Research Plan 3:

To achieve this goal, $In_{0.17}Ga_{0.83}N$ will be grown and tested under the same environment and crystal direction. The wear rate of InGaN will be compared with GaN and InN.

1.4.4 Electronic Property Modification by Tribological Sliding

Question 4:

How are the surface charge properties impacted by shear?

Hypothesis 4:

Applied normal load might cause the formation and propagation of defects underneath the worn surface. These newly generated defects can alter the surface charge properties of GaN, *i.e.*, tuning the Fermi level and surface band bending.

Proposed Research Plan 4:

Wear scars will be prepared under different environments, different sliding cycles, and different normal loads. XPS and LVSEM will be employed to visualize the band bending inside the wear scar and compare with the as-grown surface. STEM will also be utilized to image the lattice underneath the surface.

2 Materials: MOCVD-Growth of III-Nitrides

The electronics and optoelectronic properties of III-Nitride materials have been rigorously explored as a function of structure, composition and processing conditions [5]–[9], [21], [22], [156]–[168]. These tremendous advances on the understanding of the optoelectronic properties of III-nitride-based materials are in stark contrast to that of the understanding of mechanical and tribological properties in the III-Nitrides. Our preliminary results reveal that GaN is surprisingly wear resistant, approaching the wear rate of diamond (known for its hardness and wear resistance [169]–[171]) in certain environments. Optimizing the growth of III-Nitrides is one of the pivotal challenges in achieving further understanding of this material system, *e.g.*, lattice structure, polarization, defect type and its formation, *etc.*, thereby assisting the improvement of device performance by optimizing the growth procedure. Metal-organic chemical vapor deposition (MOCVD) is the most common epitaxial method to grow III-Nitrides. Other techniques for III-Nitrides thin film growth includes molecular beam epitaxy (MBE) [172]–[175] and hydride vapor phase epitaxy (HVPE) [176]–[179]. The following sections briefly introduce the MOCVD growth procedures of different materials.

2.1 Binary Composites: GaN, AlN and InN

2.1.1 GaN

Unintentional doped wurtzite GaN epilayers are grown by metal-organic chemical vapor deposition on c-plane single crystal sapphire (α-Al_2O_3). Ammonia and trimethylgallium are used as the precursors to form GaN. The chemical mechanism is shown below.

$$(CH_3)_3Ga\ (g) + NH_3\ (g)\ \rightarrow GaN\ (s) + 3CH_4\ (g)$$

Sapphire is used as the substrate to grow GaN thin film due to their similar lattice structures. The sapphire substrate is baked at 1080 °C to remove all dirt and adsorbents. A 30-50nm thick GaN is then grown on sapphire under a relatively low temperature (LT) of around 530 °C. When the growth of the low temperature GaN is completed, the temperature is ramped up to 1050 °C with an ammonia overpressure inside the chamber to convert the deposited 2-D LT GaN into 3D islands, which is called the back-etch process. A detector is employed to monitor the roughness of the coating. Once the surface roughness approaches its minimum value, the etching process is stopped and the chamber is backfilled with ammonia together with trimethylgallium. Normally the size of the 3D islands at this step varies from 10-50nm [180]. The mixture of ammonia and trimethylgallium react under high pressure and high temperature to break their own old bonds and form new GaN bonds with one other. The lateral growth rate of GaN is higher than the out-of-plane growth rate and these newly formed Ga-N fill in the valleys between islands first, followed by an intra-island coalesced to gradually form a 2D GaN coating. The whole growth process is briefly illustrated in Fig. 2-1a. By carefully adjust the temperature during growth, the waviness and surface roughness can be well tuned.

It is noteworthy that there exists a 30° rotation phenomenon of orientation between GaN epilayer and sapphire substrate. This is illustrated in Fig. 2-1b. When the GaN is grown on top of a sapphire lattice without rotation, the lattice mismatch induced compressive strain on GaN can be as high as 20-30% (a_{GaN}=3.186Å, c_{GaN}=5.185Å, a_{sapphire}=4.758Å, c_{sapphire}=12.991Å). When the GaN lattice rotates 30° to the sapphire lattice, the effective lattice constant now is $\sqrt{3}a_{\mathrm{GaN}}$ and the strain drops down to -16%. In this way the GaN epilayer can be engineered to the greatest extent to minimize its strain.

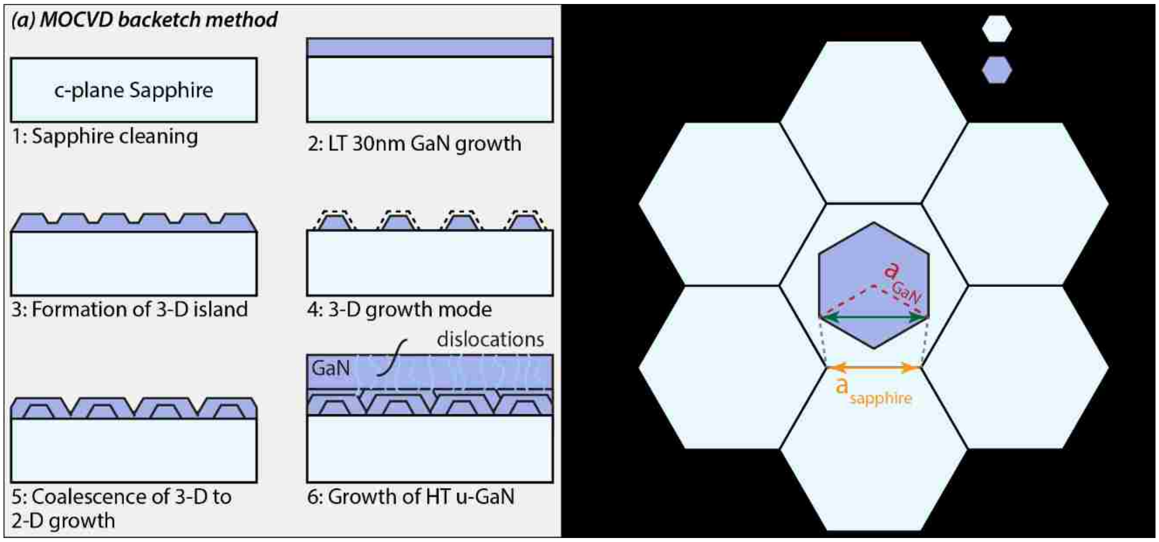

Figure 2-1 Schematic of (a) MOCVD growth of GaN coating; (b) lattice mismatch between GaN and sapphire substrate.

2.1.2 AlN and InN

In general, the MOCVD growth of the wurtzite AlN is similar to that of GaN. A (0001)-GaN template is used for an AlN coating growth. An AlN seed/nucleation layer is grown first under low temperature for a short period, with an Al predeposition using trimethylaluminum before supplying ammonia. Then the temperature is ramped up for 7-10 minutes for an AlN recrystallization. Afterwards, a thicker AlN epilayer is grown on top of this low temperature AlN nucleation layer under low pressure and high temperature (1100 °C – 1600 °C) [181]. There is no back-etch process performed here to form 3-D islands because of the smaller lattice mismatch between AlN and GaN template when compared to GaN/sapphire.

In our research, the AlN coating was provided by Sandia National Laboratory. The coating was grown by a state-of-the-art MOCVD reactor produced by Taiyo Nippon Sanso (SR400HT). In this reactor, the epitaxy of AlN is slightly different from the conventional process. The AlN coating was directly grown on top of (0001)-sapphire substrate. The sapphire substrate was heated up to 920 °C, while the pressure of the growth chamber was raised up to 40 kPa. This was followed by a one standard liter per minute (SLM) flow of ammonia into the chamber for 7 min for the purpose of nitridation. Following the nitridation process, a 100 nm AlN nucleation layer was grown at the same temperature and pressure with 0.3 SLM flow of ammonia. Afterwards, the bulk AlN epitaxy was performed under the higher temperature at 1320 °C while the pressure was lowered down to 13 kPa. At this stage, the flow rate of ammonia was increased back to one SLM.

For InN growth, trimethylindium and ammonia is used as group-III and V precursors, respectively, with nitrogen as the carrier gas and ambient. The optimized growth temperature for the InN is around 540 °C, which is much lower than GaN and AlN. In order to avoid a droplet-free InN coating when supplying continuous trimethylindium and nitrogen precursors into the chamber, a high V/III (nitrogen source/indium source) ratio is required. On the other hand, a pulsed mode epitaxy technique can be implemented to achieve the reproducible high-quality InN coating.

2.2 Ternary Composites: InGaN, AlGaN

The epitaxy of low In-composition (<20%) InGaN materials has been well studied and implemented for solid state lighting application in recent decades. This material is used to form the quantum well active region for blue and visible emitters. Generally, the InGaN coating is grown under low temperatures on top of a GaN epilayer. Trimethylindium (TMIn) and triethylgallium (TEGa) are used as the group-III precursors. As mentioned, because the growth temperature of InN is much lower than that of GaN, the In-composition in the solid-phase InGaN coating will be determined by the growth temperature when the ratio of TMIn over the group-III precursor is sufficiently high. Specifically, higher temperatures will yield lower In-composition, and vice versa. In our study, by adjusting the growth temperature from ~ 700 °C to ~ 780 °C, the In-composition was tuned from 20% to 10%.

Unlike the In-composition of InGaN being dominated by growth temperature, the Al-composition in the solid phase AlGaN coating is generally determined by the gas phase ratio of TMAl over group-III precursors. Such high temperature grown AlGaN has been widely applied in deep ultraviolet (UV) device applications and power electronics. Trimethylaluminum (TMAl) and trimethylgallium (TMGa) are used as the precursors for AlGaN epitaxy under high temperature (~1050 °C). Alternatively, AlGaN can also be grown under ~700 °C using TMAl and TEGa as precursors. AlGaN epitaxy grown under such low temperature conditions has been recently implemented in quantum well active region design for longer wavelength emitters.

3 Methods

3.1 Wear Test

Linear reciprocating dry sliding tests and unidirectional rotary tests were performed by custom-built microtribometer and rotary tribometer, respectively. A microtribometer was mounted in a glovebox (MBraun LABstar workstation) backfilled with either dry nitrogen (NI 4.8, purity 99.998%) or lab air diluted with compressed dry air to realize environment control. Several environments, including dry nitrogen (H2O < 1PPM, O2 < 1PPM) and lab air (relative humidity varies from 5%RH to 75%RH) were selected to investigate the environment dependence of III-Nitride coatings. Single crystal α-alumina (ruby) balls with radius of 0.75mm (Edmund Optics, Grade 25) were used as the countersamples to reciprocate against testing coatings with a constant velocity. Alumina balls were selected here as countersamples because of their chemical inert nature, well-known Mohr's hardness, as well as their high wear resistance.

3.1.1 Linear Reciprocating Microtribometer

Figure 3-1a shows the schematic of the custom type pin-on-disk microtribometer. The linear reciprocating sliding was achieved by a linear motor stage (Aerotech ANT95-L, Fig. 3-1a). This single-axis linear nanopositioning stage moving in x-direction has the travel range of 100mm with the minimum incremental motion of 1nm and the maximum speed of 500mm/s. A piezo stage (PI p-628.1CD) mounted on top of the motor stage moves in y-direction for raster sliding purposes. This piezo stage has the travel range of 800μm with the resolution of 0.1nm. A cantilever is mounted to a second piezo-stage to allow for precise load control. The cantilever is made of Ti-6Al-4V (Ti-

64) and has various designs which cover a broad range of elastic constant (both normal and frictional directions) to meet the specific research requirements. Once the countersample gets in touch with the test piece, the deflection of the cantilever will change the space between the cantilever and capacitance probe (F_n), and the instantaneous normal force can be calculated and recorded. Likewise, as the friction force which originates from the relative motion between the sample and countersample changes, the gap between the cantilever and capacitance probe (F_f) and the frictional force is measured. For the reciprocating sliding test, the friction loop consisting of a forward and a backward stroke is recorded. The friction coefficient ($\mu = \frac{F_f}{F_n}$) can then be calculated by averaging over the middle 20% of forward and backward stroke, as shown in the inset of Figure 3-1. The sampling rate for recording normal and frictional force was set to be 0.01s in this study. The resolution of the capacitance sensors (LION Precision, probe: C5R-2.0, driver: CPL290) has two sensitivity levels, a high sensitivity of 10nm and a low sensitivity of 100nm, to meet specific experiment purpose. The uncertainty of this test comes from the measurements of normal load, frictional load, thermal expansion of the aluminum parts/holders, accuracy and repeatability of the motor stage, as well as the calibration of the cantilever spring constant.

3.1.2 Rotary Tribometer

A motorized rotary stage (PI M-660.55 high speed motorized precision rotation stage) is used to carry out the rotary sliding test. This rotary stage has no limit of rotation range with the maximum speed of 720°/s and minimum incremental motion of 34 μrad. A double leaf spring flexure with normal stiffness of 13,560 mN/mm and lateral stiffness of 15,275 mN/mm is used as a cantilever to apply normal load and measure the frictional load. Two strain gauges are attached to the flexure to measure both normal and frictional forces. The reading from the micrometer to the radius of the wear track is calibrated and correlated by the white light interferometer before the experiment.

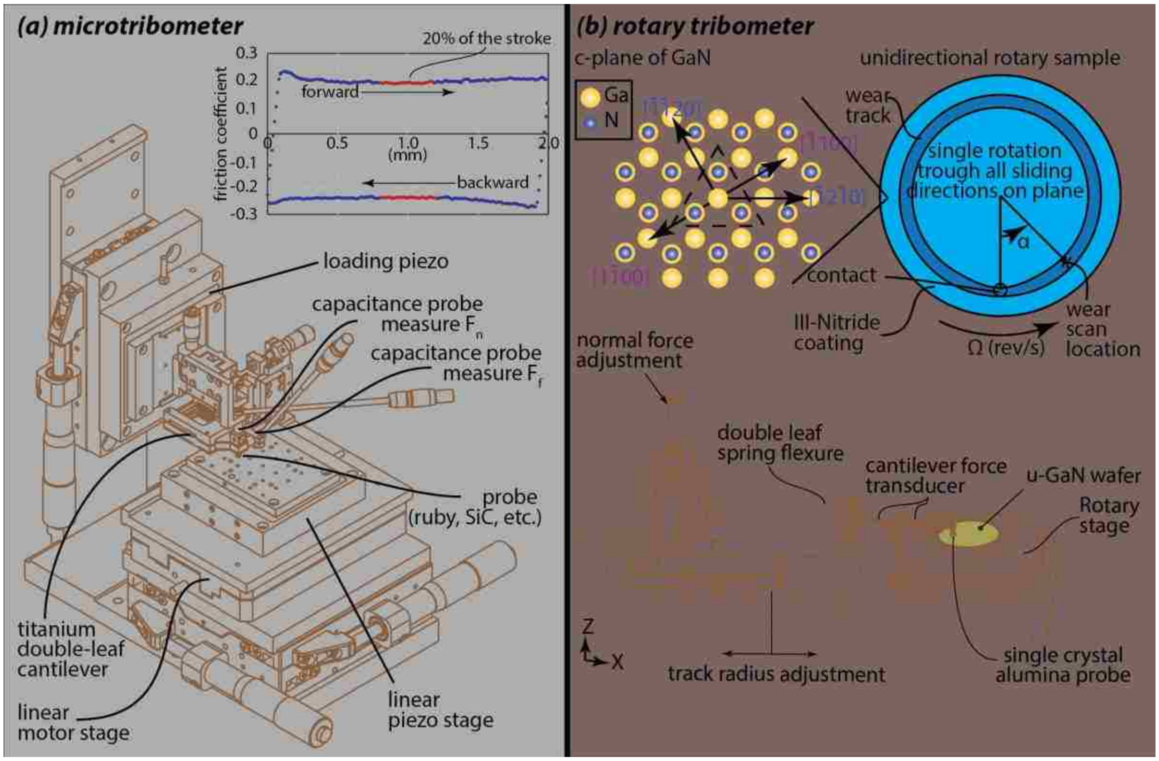

Figure 3-1 Illustrations of (a) linear microtribometer and (b) rotary tribometer.

In addition to simple reciprocating sliding test, a stripe test is also conducted to resolve the cycle number for tribochemistry evolution analysis. By decreasing the stroke length while increasing the cycle number, multiple wear regions with different sliding cycle can be differentiated for further investigation individually.

3.2 Wear Rate Calculation

All the samples were sonicated in acetone first for 5 min and then in IPA for 5 min once the wear test was done to remove the wear debris, and blown dry with ionized dry nitrogen. The 3D profiles of wear scars are obtained by using the scanning white light interferometer (SWLI, Bruker ContourGT-K). For minimizing the variation of wear rate caused by local defect and surface non-uniformity, 20 profilometric scans were made for each wear scar and five 2D height map cross-section were acquired over each individual profilometric scan. Fig. 3-2 shows the procedure of obtaining cross-sectional area of the wear scar for wear rate calculation.

(1) A profilometric scan was first made using SWLI;

(2) 5 line scans were dragged across the wear scar to extract the 2D height profiles at different locations within one profilometric scan;

(3) Each height profile was leveled and the cross-sectional area was obtained (as highlighted in red in Figure 3-2b).

Overall, the average wear rate for each wear scar was calculated from these 100 cross-sections based on the Archard's wear rate, as shown below.

$$K\left[\frac{mm^3}{N\cdot m}\right]=\frac{V[mm^3]}{F_n[N]\cdot d[m]}=\frac{A[mm^2]}{F_n[N]\cdot 2\cdot C}\cdot 10^3\left[\frac{mm}{m}\right]$$

where A is the measured cross-section of wear scar, C is for the number of reciprocating sliding cycles (one cycle includes one forward stroke and one reverse stroke), F_n is the applied normal load. A factor of 1000 [mm/m] here is used for unit consistency.

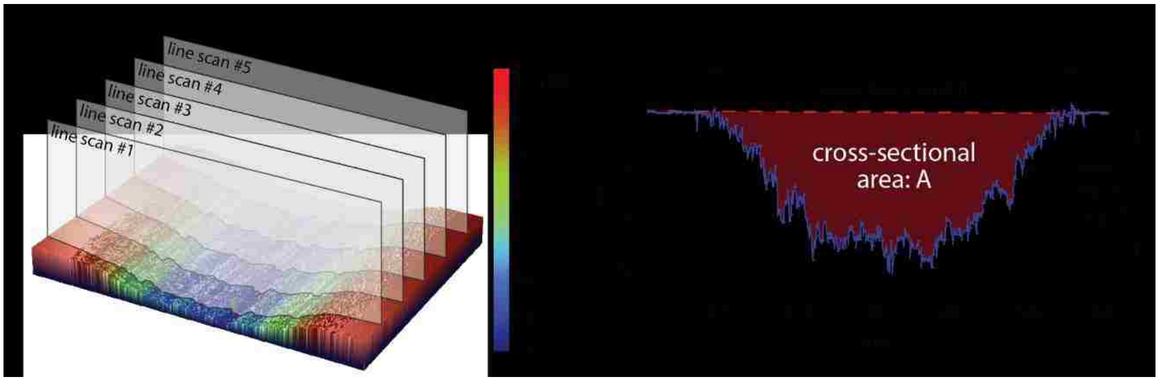

Figure 3-2 (a) Profilometric scan of wear scar; (b) 2-D wear scar profile.

The uncertainty of the wear rate comes from the measured normal load, lost volume and sliding distance, which is calculated as

$$\frac{\delta K}{K} = \sqrt{(\frac{\delta F_n}{F_n})^2 + (\frac{\delta V}{V})^2 + (\frac{\delta d}{d})^2}$$

3.3 Advanced Characterization Techniques

Several advanced characterization techniques are used here to analyze the worn surface and link it to wear mechanisms and tribochemical reactions during the sliding. Detailed descriptions for each characterization are discussed below.

3.3.1 Nanoindentation

The measurements of hardness and Young's moduli of III-Nitride coatings were achieved by nanoindentation (Hysitron TI-950 Triboindenter). A three-sided pyramidal Berkovich diamond tip (Hysitron) with radius of ~50nm was used. All the parameters that were directly measured or derived are indicated in the schematic (Fig. 3-3a). The area function of the tip was calibrated by indenting on a standard fused quartz sample from 0.1mN to 10mN over 100 indents. Area function was fitted with the reduced modulus of fused quartz (69.6GPa). This is shown below:

$$A = C_0 h_c^2 + C_1 h_c + C_2 h_c^{1/2} + C_3 h_c^{1/4} + C_4 h_c^{1/8} + C_5 h_c^{1/16}$$

where A is the calibrated area as a function of contact depth, C_0 is kept at constant value of 24.5 in ideal case and C_1 to C_5 are fitting parameters.

The nanoindentation was conducted with displacement control with the maximum displacement capped at 100nm. As a rule of thumb, the total penetration was kept to less than 10% of the coating to avoid any substrate effect. Loading and unloading rates were set to be 5nm/s (nominal 0.05/s) and the holding time was 5s. At least 20 indentations were made for each coating to obtain average values of hardness and Young's modulus. The grid of indents was set to be 5 × 5 and each indent was 10μm away from others. The calculation of Young's modulus and hardness was done using the Oliver-Pharr method [182], as shown below.

The reduced modulus is evaluated by

$$E_r = \frac{S\sqrt{\pi}}{2\sqrt{A}}$$

with

$$S = \frac{dP}{dh}$$

Data from 5% of the start of unloading curve to 50% of unloading was selected for calculating S, as shown in Fig. 3-3b. With the known Young's modulus and Poisson's ratio of indenter, and the calculated reduced modulus, the Young's modulus of the testing sample can be obtained by

$$\frac{1}{E_r} = \frac{1 - \upsilon_{sample}^2}{E_{sample}} + \frac{1 - \upsilon_{indenter}^2}{E_{indenter}}$$

The hardness of the sample can be evaluated by

$$H = \frac{P_{max}}{A}$$

The schematic of nanoindentation calculation is shown in Fig. 3-3b.

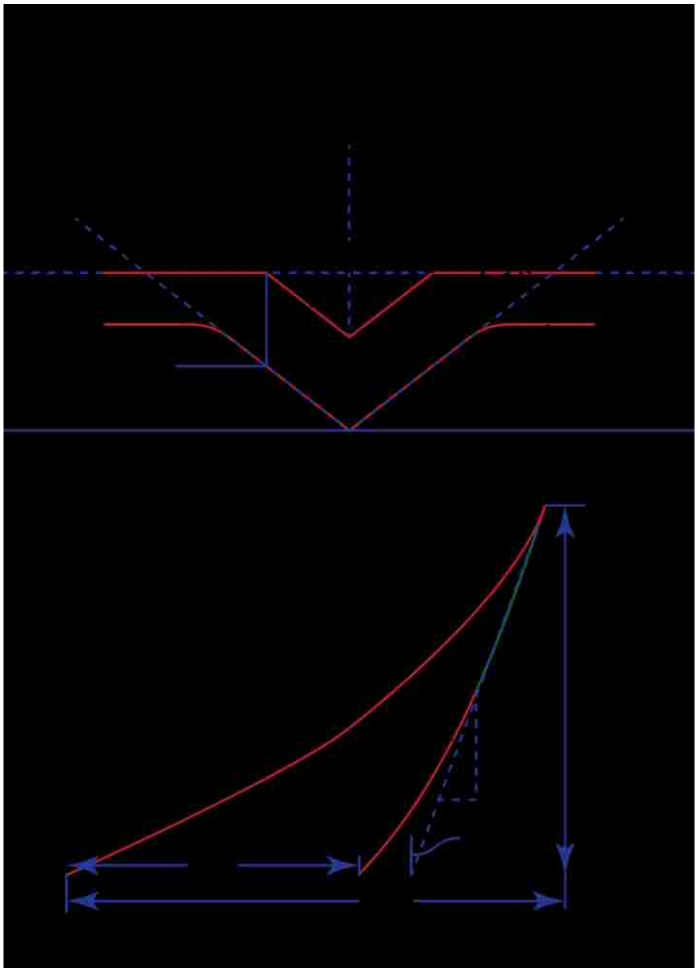

Figure 3-3 (a) schematic of nanoindentation; (b) load-displacement plot of nanoindentation.

Because the hardness measurement of the material highly depends on the material quality, nanoindentation can not only extract the hardness and Young's modulus, but is also capable of scrutinizing the sample quality qualitatively. A 2 × 10 array of indents was made inside wear scars generated under low humidity (~10%RH) and high humidity (~75%RH) lab air environments. The load-displacement plot was used to analyze the dislocation density (“pop-out”) and the obtained hardness was compared with the unworn area.

3.3.2 XPS and Auger Scan

X-ray photoemission spectroscopy (XPS), also known as electron spectroscopy for chemical analysis (ESCA), is a cutting-edge surface sensitive characterization technique for surface composition analysis. The sampling depth of XPS typically ranges from 1-9 nm, depending on the testing material. The working principle of XPS is based upon the photoelectric effect discovered by Einstein in 1905. A core level electron is photoejected by an incident X-ray photon, which reveals the elemental composition as well as some information regarding the “environment” of atoms (*e.g.*, what other species are bonding to this detected atom), as shown in Fig. 3-4. Several mechanisms give rise to XPS peak shifts. Changing of the chemical state leads to variations of the electron configuration of neighboring bonds, resulting in an increase (or decrease) of the local electrostatic potential of the core level. This gives rise to the observed chemical shift (core-level shift) of the XPS peak. Secondly, the XPS peak shift can also arise from surface band bending. When there is no surface band bending, based on the law of conservation of energy, the binding energy will be equal to incident photon energy minus the detected kinetic energy of the escaping photoelectron and the work function of the sample. However, with presence of a net charge in space charge region, the potential energy of all the energy levels at the surface will be changed. This directly leads to different binding energies read from detector, as shown in Fig. 3-5. Thus, XPS is a widely used technique in surface band bending measurements of semiconductors. More details of how to apply XPS in measuring band bending of shear-modified GaN surfaces will be discussed in Chapter 7. Charging and surface dipoles can also cause peak shifts in XPS. This mechanism can be simply understood as an additional electrical field generated at the surface which influences the ejected photoelectron, similar to band bending case.

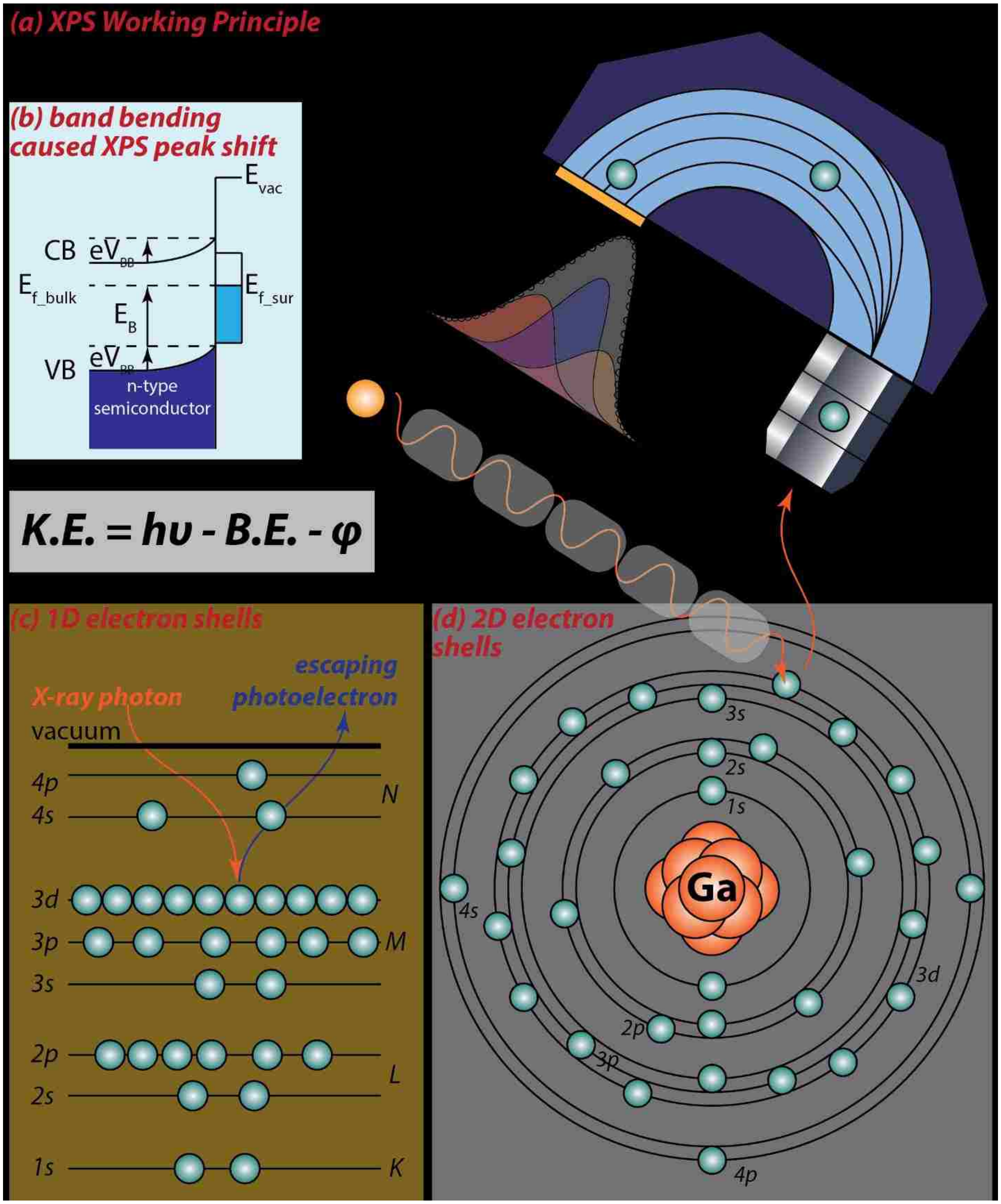

Figure 3-4 Illustration of XPS working principle.

Our XPS analysis of the GaN samples was conducted by an X-ray Photoelectron Spectrometer (XPS) (ThermoFisher K-Alpha$^+$ XPS spectrometer System) at Imaging and Analysis Center (IAC), Princeton Institute for the Science and Technology of Materials (PRISM), Princeton University. This system has been equipped with monochromatic X-ray source and a focused lens which allows selecting an analysis area from 30 µm to 400 µm in 5 µm steps. A flood source with low-energy ions (0.1 eV) was used to provide effective charge compensation. In addition to a flood gun, a 20 nm thick Ir coating was sputtered at the corner of the sample for better conduction of the surface charge. The XPS system has been calibrated by recording a clean Au sample with the Fermi edge binding energy at 0 eV and Au4f binding energy at 84.0 eV.

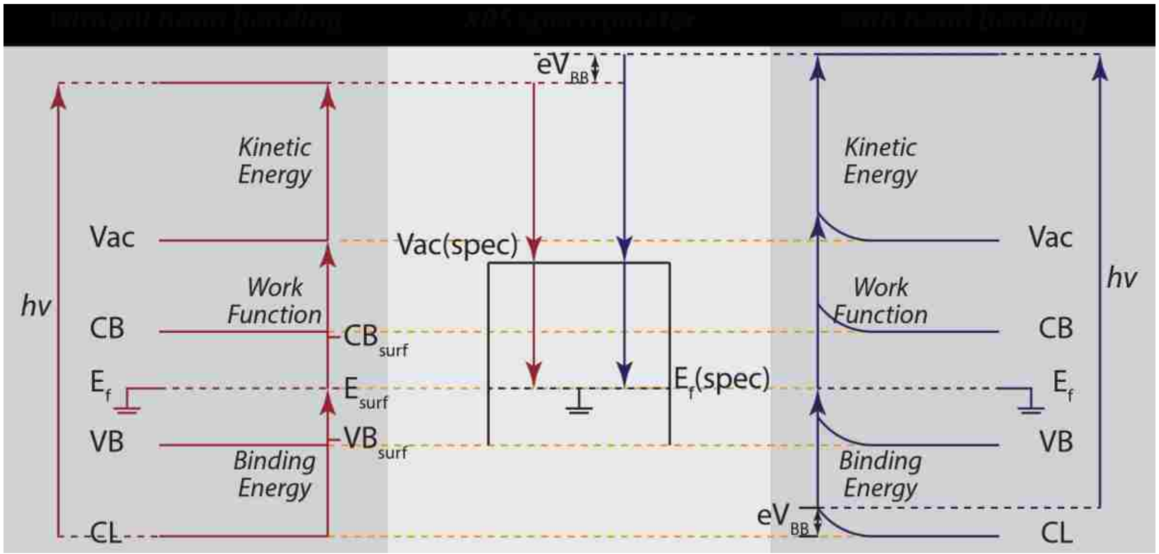

Figure 3-5 Illustration of energy diagram with and without band bending.

Line scans were performed for each wear scar to analyze unworn surface (as received surface), wear debris on both sides of the wear track, and the wear scar. The focused X-ray beam can focus to an elliptical spot with a long axis of 30µm long and a short axis of 10µm long, which can be fitted into the wear scar (varying from 30µm to 70µm from sample to sample). A survey spectrum was conducted first to find out all components existing on the surface, then specific elements were added for further chemical state analysis. During XPS scans, Ga 2p, Ga 3d, N 1s, C1s and O 1s were recorded under 50 eV pass energy and ultrafine scans with high signal to noise ratio for Ga 3d, N 1s and Fermi edges are obtained over 100 scans.

Scanning Auger electron spectroscopy (AES) is a standard characterization technique in surface and interface physics and chemistry with the typical probing depth in the range of 10-50 Å [183]. Similar to XPS, AES is also a core-level spectroscopy. The incident electron beam from an electron gun excites secondary electrons which can be detected and analyzed by an electron detector. The working principle of AES is illustrated in Fig. 3-6. The core-level shell (K or L) is ionized by the primary electron, leaving a vacancy on this shell. This process forces the atom in an perturbed state. An electron from an energetically high-lying shell will fall into the deeper atomic level to fill this vacancy. This deexcitation process is either accompanied by an emission of an X-ray photon or a radiation-less Auger transition. In the latter case, the energy originated from the electron filling process will be gained by another electron at some different (or same) shell. This electron then will be emitted with a well-defined kinetic energy, which directly relates to the core-level energy of atom, and measured by the electron detect. This electron is called Auger electron.

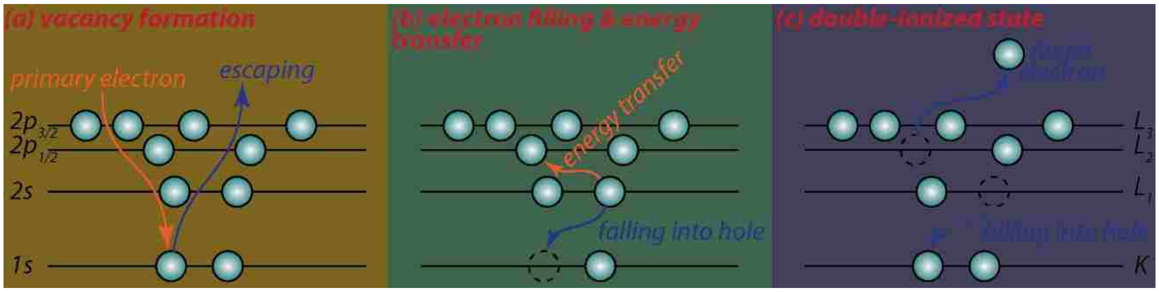

Figure 3-6 Schematic of Auger process: example of KL_1L_2 process.

In contrast to other surface characterization techniques, such as X-ray photoemission spectroscopy (XPS), surface extended X-ray absorption fine structure (SEXAFS), and high resolution electron energy loss spectroscopy (HREELS), AES has better lateral and in-depth resolutions, which can perfectly probe at small geometries, such as valleys and peaks, inside the wear scar. There is also no specific sample preparation requirement when compared to high resolution transmission electron microscopy (HR-TEM). Thus, we utilized AES here to interrogate the elemental composition on the topmost layers of the worn surface obtained under humid environments.

In our study, the surface compositions of GaN were analyzed by Scanning Auger Microscopy (SAM) at Princeton Plasma Physics laboratory (PPPL). The probing depth of SAM is limited by the mean free path of the Auger electrons traveling through the material, which is typically in the order of 0.5 to 5 nm. During the measurement, a 10 keV focused electron beam was scanned across the surface to obtain regular scanning electron microscopy (SEM) images. Using the SEM images as the reference for locating the regions of interest, SAM analysis was conducted to obtain a lateral distribution of Ga, N and O on the surface with the spatial resolution of 100 nm. Fine spectra of Ga LMM, O KLL, C KLL and N KLL were obtained at three different locations: inside and outside of the wear track, along with the region with wear debris engendered during the wear test. 1D line scan and 2D mappings were utilized to obtain the elemental information in these three different regions. Sample current was collected during the 1D line scan with a positive 50 volts sample bias.

3.3.3 FIB Milling and STEM

Focused ion beam (FIB) (FEI Scios DualBeam system) was used to prepare the TEM specimen. Gallium liquid metal was used as the ion source for milling while an electron beam which is 52° with respect to the ion beam was used to monitor the cutting process. The FIB milling began with platinum deposition for surface protection. There are two types of Pt deposition: (1) ion beam assisted Pt deposition which is fast but has certain amount of damage to the surface, and (2) electron-assisted which has much lighter mass which leads to much less damage to the surface, but slower Pt deposition. Thus, the e-beam Pt deposition was first conducted with thickness of 250 nm to protect the surface, then followed by 2 µm thick ion-assisted Pt deposition. The 250 nm e-beam Pt consists of two parts: two valleys were covered with 100 nm e-beam Pt, then a 150 nm thick Pt was deposited to cover both valleys and peaks, as shown in Fig.3-7 (a). This two-step e-beam Pt deposition were used as markers to distinguish the valley and peak inside the wear scar for later TEM analysis. A 50 nA ion beam current with 30 kV acceleration voltage was used to dig trenches on both sides of the specimen. The surfaces of cross-sections were thinned by a smaller beam (0.5 nA, 30 kV) to remove curtain effect before lift-out. After the specimen was attached to the grid, the thinning process was performed primarily with 0.3 nA i-beam current on both sides until the specimen was 5 kV electron transparent. When the sample thinning was done, both sides of the TEM specimen were exposed to the ion beam with 5 kV accelerating voltage and 47 pA beam current for further polishing, as well as removing ion implantation and reducing surface damage during the FIB milling. In addition, specimens were final thinned using a 900 eV Ar ion beam using a Fischione 1040 NanoMill.

The sub-surface atomic structure and composition were analyzed with aberration-corrected STEM using a JEOL JEM-ARM200CF instrument. The STEM is equipped with the latest generation CEOS ASCOR probe corrector that corrects for 3rd and 4th order aberrations, and an INCA high area silicon drift detector (SDD) that enables high X-ray count rates. Data was acquired using a 200 keV probe. Imaging resolution is sub-angstrom and the chemical resolution using Energy Dispersive Microscopy (EDS) is on the atomic scale. High-angle annular dark field (HAADF) images were acquired and EDS maps were collected with background subtracted for the Ga Kα, N Kα, and O Kα elemental peaks.

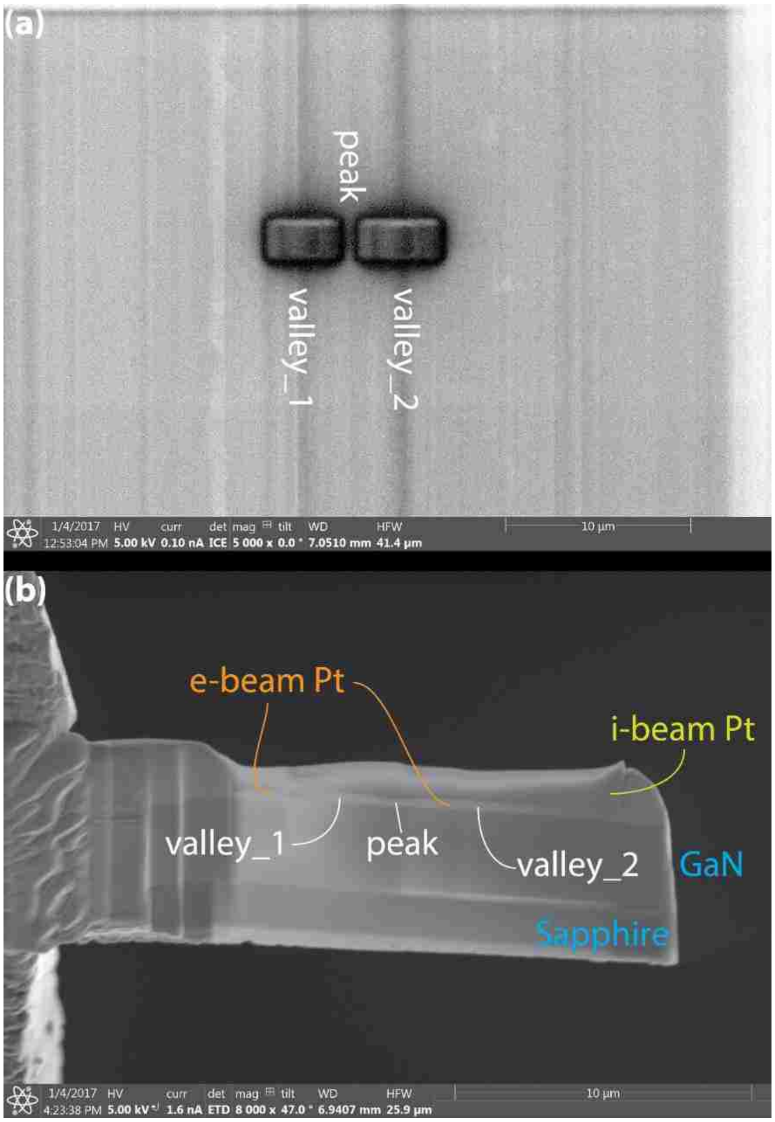

Figure 3-7 SEM image of Pt deposition; (b) 5kV electron transparent TEM specimen, valley and peak regions marked by e-beam Pt

3.3.4 Atomic Force Microscopy

Atomic force microscopy (AFM) (Bruker NanoMan) at Imaging and Analysis Center (IAC), Princeton Institute for the Science and Technology of Materials (PRISM), Princeton University, was employed for revealing the morphology of worn surface in nanoscale. Single crystal silicon tip coated with Pt/Ir and a radius of 6 nm was utilized as the probe (NT-MDT NSG10, Antimony doped, frequency 140-390 kHz). The working principle of AFM is described as follow (Fig. 3-8). A laser diode was first turned on and a highly dense laser beam was located on top of the cantilever spring. The laser beam was reflected to a photodetector used for recording the displacement of the cantilever. Atomic force occurs between the sharp tip and the sample when the cantilever is close enough to the surface. Any variation in height will change the force vector which can be accurately sensed by the tip and revealed in the photodetector. Based on the nature of the tip motion, imaging mode can be classified into three different types, *i.e.*, contact mode, tapping mode (semicontact mode), and noncontact mode [184].

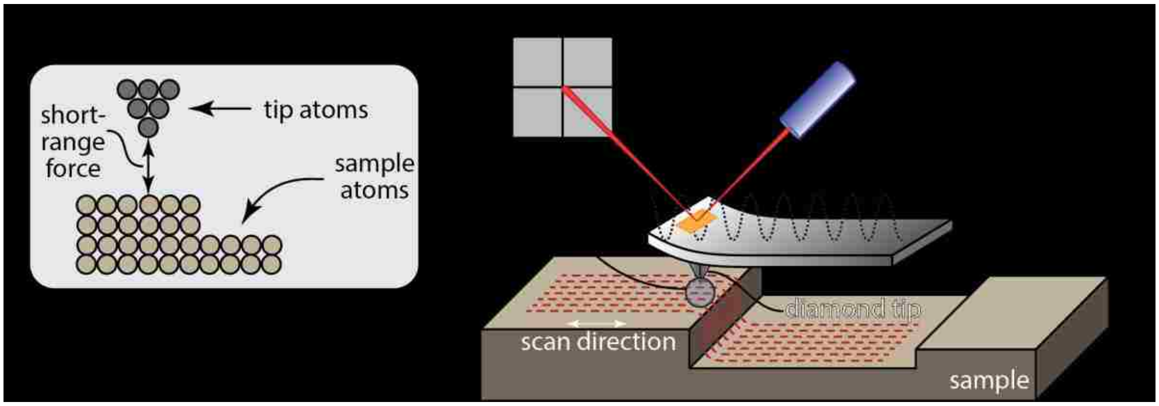

Figure 3-8 AFM working principle

Contact Mode

When the tip is sufficiently close to the surface of the sample, a strong attractive force occurs and the tip will “snap-in” to the surface of the sample. Then the tip will be dragged across the area of interested and the contour of the surface will be recorded. In order to minimize the noise and drift under this contact mode, a flexure cantilever is required (*i.e.*, low stiffness). By attaining large enough deflection of cantilever while keeping the contact force as low as possible, the contrast between measured signal and background noise can be significantly enhanced.

Tapping Mode

Moisture is an inevitable problem for AFM measurements. The water molecules adsorbed on the surface of the sample will form a liquid meniscus layer. When performing AFM scanning under contact mode, the tip will stick to the surface due to the presence of this liquid layer. A tapping mode can be employed to minimize this effect. A small piezo element is used to drive the cantilever oscillating with (or near) its resonance frequency with a specific amplitude. Commonly the amplitude will vary from a few nanometers to hundreds of nanometers. Before approaching the surface, the resonance frequency and amplitude are obtained and kept constant. These two parameters are used to interpret the contour, stiffness, adhesion, *etc.*, of the measured surface. Once the tip is brought close enough to the surface, the short-range forces (Van der Waals force, electrostatic force, *etc*.) will markedly change the amplitude of the cantilever. This feedback of amplitude variation will go directly to the electronic servo and an adjustment of cantilever height will be made to resume the original amplitude. In this way the topography of the sample can be recorded. By using tapping mode, one can not only prevent the adhesion caused by liquid layer on surface, but also minimize the direct mechanical contact between tip and sample, which in turn minimizes the wear of the sharp tip. Therefore, tapping mode is the most popular mode in AFM measurement. In addition to monitoring amplitude variation, frequency variation is also recorded. Similarily to how that amplitude can be interpreted into height profile by calculating the energy dissipation of cantilever through each oscillation cycle, frequency variation can locally reflect the stiffness and/or adhesion properties of sample. It’s noteworthy that this technique can only qualitatively reveal the material properties rather than quantitatively analyze the sample.

Noncontact Mode

By utilizing the short-range force, the contour can be obtained even without contact. In this non-contact mode, the cantilever oscillates at its resonant frequency with much less amplitude, typically ranging from few picometers to few nanometers. This small vibration makes the cantilever sensitive enough to any short-range forces that extend out to a few nanometers above the defined surface. The variation of the amplitude due to the atomic force is monitored and the servo system will adjust the height of cantilever in order to maintain the oscillation with constant amplitude and frequency similar to the tapping mode. In this way the topological profile of the surface can be obtained with the biggest advantage of any degradation effects minimized to the greatest extent. This is critical to soft samples, such as tissues and cells, hydrogels, *etc*. However, there are also some disadvantages of using this mode. As aforementioned, the water molecules adsorbed on the surface will give rise to a thin liquid layer. Both contact mode and tapping mode will penetrate through the layer and measure the real surface, while the non-contact mode will go across the surface of the liquid meniscus layer, results in measuring both the actual surface and the liquid meniscus.

3.3.5 Scanning Electron Microscopy and Energy Dispersive X-ray Spectroscopy

Scanning electron microscopy (SEM) was used here to image the morphology of the worn surface. As suggested by its name, SEM uses an electron beam as opposed to light to scan over the sample for surface imaging. The electron beam can be highly focused by electrostatic lenses, which results in spatial resolution up to a few nanometers. A high vacuum environment (usually lower than 10^{-4} mbar) is required since any particle inside the chamber can deflect the electron coming out from the sample and affect the results. However, with the progress of SEM techniques, environmental SEM (ESEM) emerges to allow the measurement of insulated materials without conductive coating. This ESEM measurement is usually performed under low vacuum mode (typically less than 1 kPa). The term "low vacuum" implies a charge stabilization while the term "environmental" is used specifically when the gas plays a thermodynamic role to either initiate a chemical reaction or prevent liquid evaporation from the sample surface. In reality, these two concepts are not mutually exclusive and can be considered the same in many engineering studies. When gas molecules are introduced into a vacuum chamber, the incident electron beam will ionize the gas molecules via collision. In the cases of positive ionized molecules and electrons interacting with the sample, the surface charging will be neutralized by positive ions, while the electrons still work in conventional way, *i.e.*, engendering secondary electrons (SEs) and backscattered electrons (BSEs), Auger electrons and X-ray. Comparison of these three kinds of electrons and X-ray is illustrated in Fig. 3-9. Secondary electrons come from materials in top 5-50 Å while the back-scattered electrons are excited from into the bulk region. Therefore, the secondary electrons reveal the surface topography and the back-scattered electrons contain more atomic number information. We selected secondary electron detector here to analyze the worn surface for defect and wear mechanism analysis. Energy-dispersive X-ray spectroscopy

(EDS) was also applied here for surface composition analysis. Similar to AES and XPS, EDS is often utilized to obtain localized chemical characterization or elemental analysis of a given specimen. The emission of characteristic X-rays can be stimulated by charged particles with high energy, such as electrons, X-rays or protons. The electrons in inner shells will be excited by the incident electron beam (primary electron) and ejected from the electron shell. The electron from outer electron shell with higher energy will fill in the hole left by the ejected electron, while emitting a specific amount of energy in the form of X-ray. In our study, the acceleration voltage was set to be 10 kV to include the Kα line of Ga. High current with aperture size of 60 μm were used to obtain higher counts of the signals. Different areas on humid and dry wear scars were mapped to compare the tribochemistry under different testing environments.

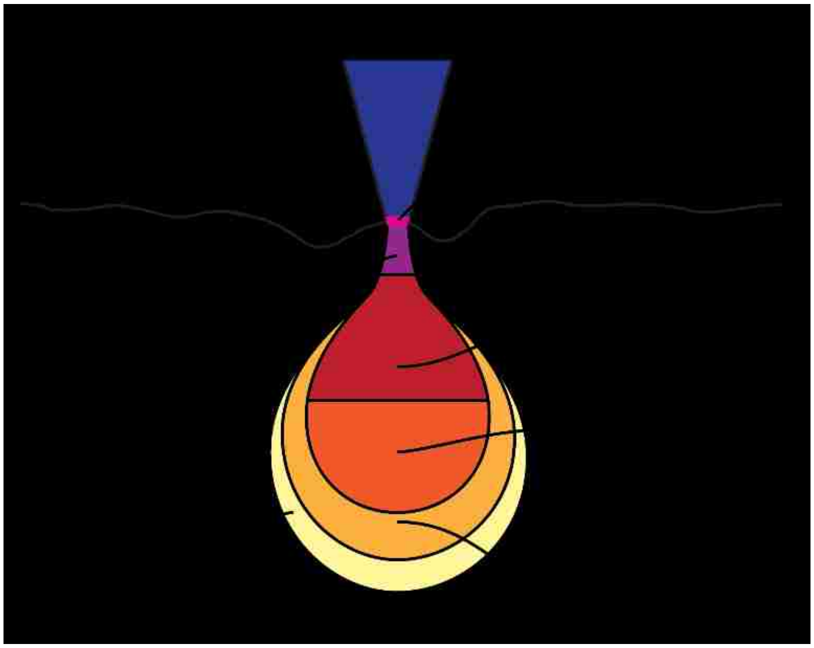

Figure 3-9 Illustration of signals coming from different area of the tested specimen.

There is one additional feature that makes SEM very useful in studying the electronic property of GaN, which is called low voltage SEM (LVSEM). The SE detector usually collects all the secondary electron signals, including SE1, SE2, SE3 and SE4. On the contrary, in-lens detector mainly capture the SE1 signal, which originates directly from the outmost surface. A primary electron beam with low accelerating voltage (typically less than 2 kV) can only penetrate top few monolayers at the surface. Thus, this low voltage technique is very suitable for band bending visualization. Surfaces with different band bending can have the secondary electron emission to differing extents, depending on the direction of the electrical field and the dimension of the space charge region. This results in a secondary electron contrast, as depicted in Fig. 3-10. With larger space charge region (depletion region/accumulation region), the built-in electrical field will be higher, which in turn further suppresses/enhances the emission of secondary electrons and higher SE contrast.

In our experiment, we started the accelerating voltage at 0.5 kV and gradually increased the accelerating voltage up to 5 kV to visualize the band bending as well as the variation of the SE contrast corresponding to the applied accelerating voltage of the primary electron beam.

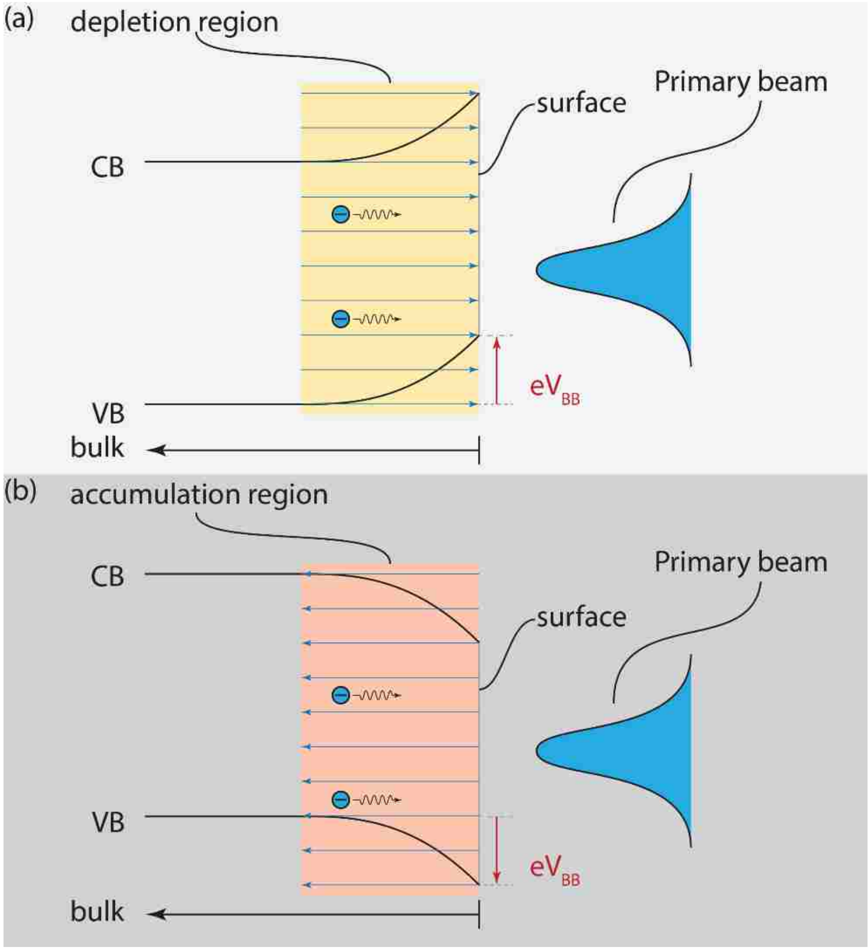

Figure 3-10 Electrical field generated inside space charge layer: (a) upward band bending; (b) downward band bending.

3.4 MS Simulation

In order to understand the directionality of wear rate of GaN, an analytical model was built to simulate the wear debris behavior that has been pulled out from the GaN coating. Two-body potential [185] between Ga and N was selected here to calculate the free energy of the system, as shown in Eqn. 3-1.

$$u_{ij} = \frac{Z_i Z_j e^2}{4\pi\varepsilon_0 r_{ij}} + f_0(b_i + b_j)\exp\left(\frac{a_i + a_j - r_{ij}}{b_i + b_j}\right) + D_{1ij}\exp(-\beta_{1ij} r_{ij}) + D_{2ij}\exp(-\beta_{2ij} r_{ij}) - \frac{c_i c_j}{r_{ij}^6}$$

Equation (3-1)

The first term represents the coulomb interaction, the second term stands for the Gilbert-type short-range repulsion, the third term contains both covalent bonding and covalent repulsion of modified Morse type and the last term shows the van der Waals potential. Z_i is the effective charge for each atom, e is the unit electric charge (1.6×10^{-19} C), ε_0 is the dielectric constant of the vacuum, the variable r_{ij} is the interatomic distance between the ith and jth atoms, f_0 is the constant for unit consistency, b_i is the softness parameter, a_i is the repulsion radius, D_1 , D_2 , β_1 and β_2 are covalent coefficients, and c_i is the van der Waals coefficient. All the parameters used in this two-body potential are listed in Table. 3-1.

Simulations start with a base of GaN consisting of 54,000 Ga and 54,000 N atoms. A small cluster of 6 Ga atoms and 6 N atoms was extracted from the center of the top surface of the base and moved up 5.166 Å (Fig. 3-11 and Fig. 3-12), at a location in registry with the GaN crystal. The reference total energy of the system was first determined when the wear cluster was placed right above the hole it left behind at a distance in registry with the base. This total energy was obtained by summing all energy potentials between each cluster atom and every atom in the base (sum of 1,295,856 potentials for each iteration). The twelve-atom “wear” cluster was then “slid” radially from the center in 0.0795 Å incremental steps out to 31.8 Å (400 steps for 10 lattice spacings from the origin). The radial sweeps started at $[\bar{1}2\bar{1}0]$ and were done at all angles along the surface, in 1 degree increments. The total energy for each location is calculated. A two-body potential was used to obtain the interaction between Ga-Ga, Ga-N and N-N [185]. The variation of total energy associating with cluster in different places along different crystal direction then was revealed.

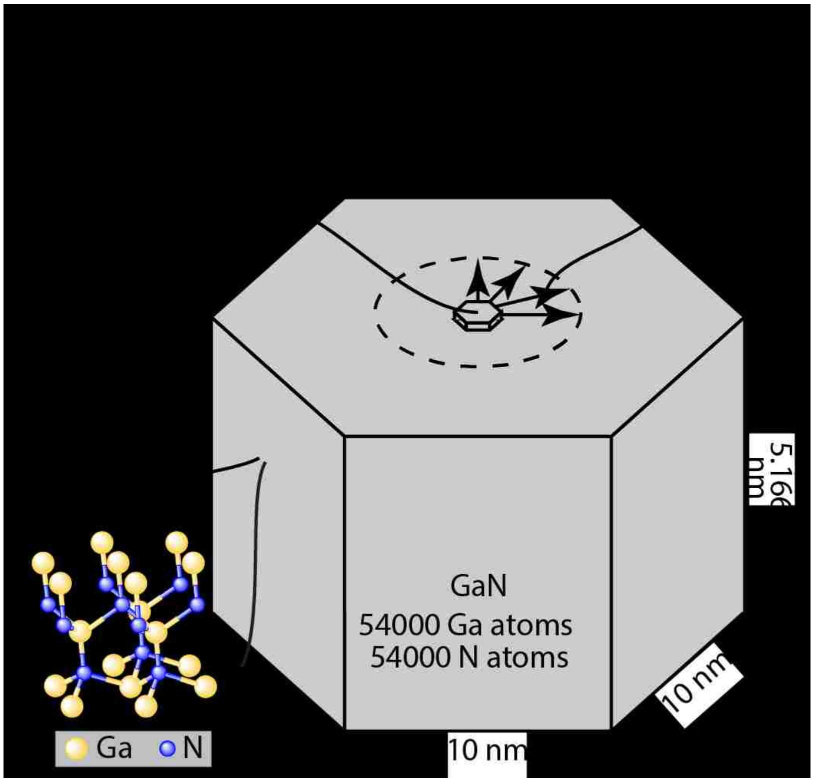

Figure 3-11 Schematic of molecular static model.

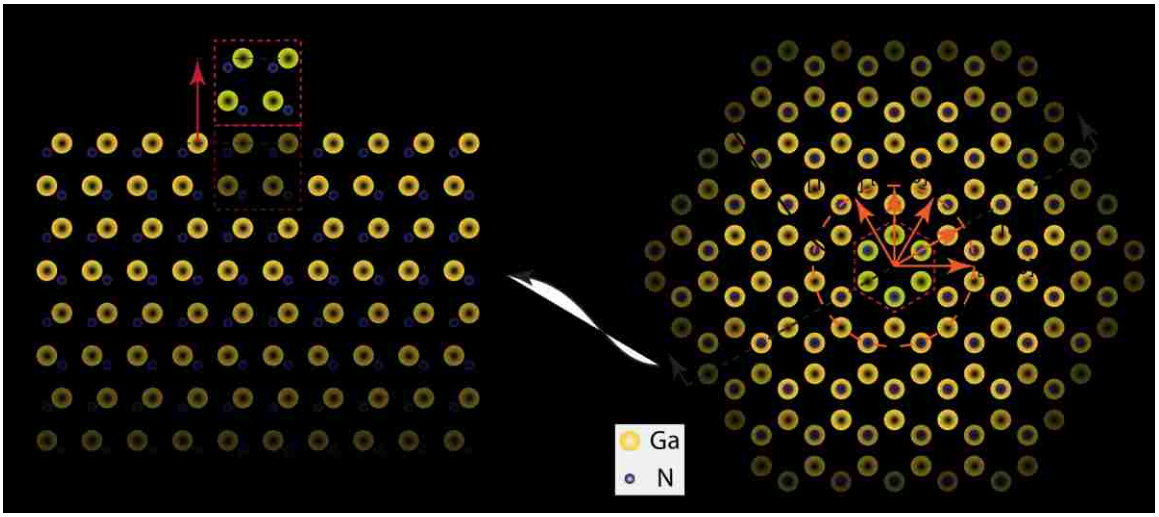

Figure 3-12 Molecular static simulation model. (a) side view (a-plane) of GaN wear cluster and base (Ga-terminated), cluster lifted out of the base by 5.166 Å; (b) top view (c-plane), wear cluster sweeps radially at all angles along the surface with 1° increments.

Table 3-1 Potential parameters of GaN for Coulomb interation, Gilbert-type repulsion, modified Morse type covalent bonding and repulsion, and van der Waals

Atom	N	Ga
Z_i (e)	-1.15	1.15
a_i (nm)	0.1970	0.0834
b_i (nm)	0.0123	0.00911
c_i (kJ/mol)$^{1/2}$(nm)^3	0.0364	0.0
atom-atom	**Ga-N**	
D_1 (kJ/mol)	-5250.5	
D_2 (kJ/mol)	6581.7	
β_1 (nm)$^{-1}$	20.0	
β_2 (nm)$^{-1}$	40.0	
Constant		
$f_0 = 41.86\ \mathrm{kJ/nm \cdot mol}$		

3.5 DFT Simulation

Density Functional Theory (DFT) is a theorem that describes correlated many-body systems [186]. The basic idea was introduced by Thomas and Fermi [187], [188] in 1927, where they defined the kinetic energy as an explicit functional of the electron density. This opened a substantial simplification, since one equation can describe what the full Schrodinger equation with 3N degrees of freedom, N being the number of electrons, can describe. Later in 1964, DFT gained important insights, when Walter Kohn and Pierre Hohenberg showed that all properties of a system can be considered as unique functionals of the ground state density [189]. Thus, the theorem was improved by Kohn and Sham in 1965, who developed the *ansatz* for the ground state density that is widely applied in various calculations nowadays [190].

In our study, relative surface energy calculations for investigating the effect of water on the surface of GaN are performed using the slab approach, similar to other approaches [191], [192]. The DFT calculations performed in this work are based on the MedeA Vienna Ab Initio Simulation Package (VASP), a commercially available software widely used for various types of DFT calculations [193]. In the calculations, the Perdew-Burke-Ernzerhof (PBE) version of the Generalized Gradient Approximation (GGA) has been utilized. Structures were initially optimized using the structure optimization tool, where the atoms were allowed to relax with the Hellman-Feynman force set to 0.02 eV/Å. The energy iteration convergence was set to $1\text{x}10^{-5}$ eV using the Normal (blocked Davidson) algorithm and reciprocal space projection operators. The slabs were constructed with ~10 Å separation to minimize interaction with neighboring layers. Plane wave cut off energy was set to 400 eV along with ‘normal’ precision, whereas the k-spacing was set to 0.5 1/Å, leading to a 3 × 3 × 1 gamma-centered k-mesh. In addition, the external stress to the system was set to 0 GPa and a Methfessel-Paxton integration scheme was used with a smearing width of 0.02 eV.

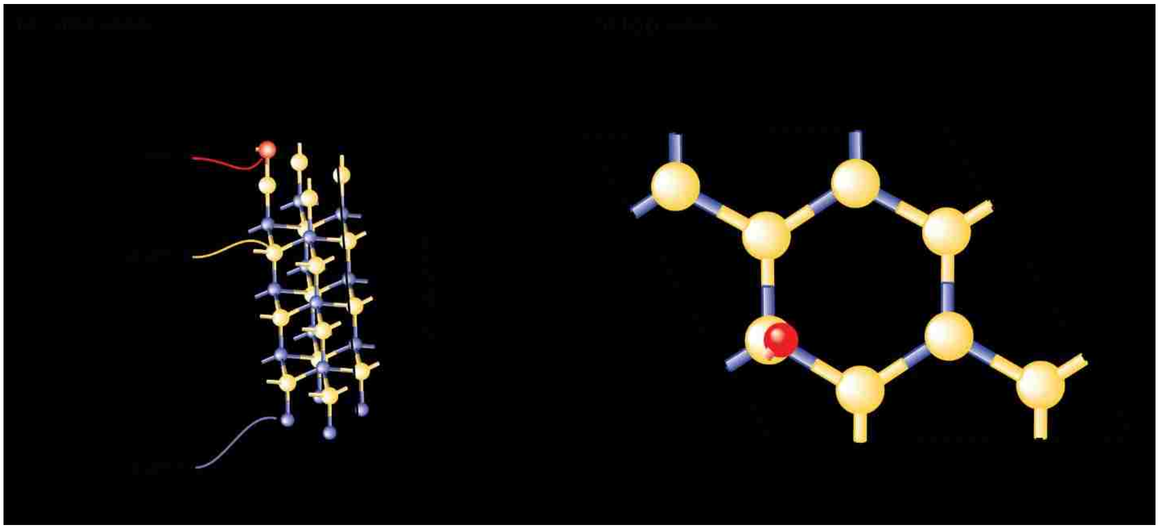

Figure 3-13 (a) Side view of a GaN slab contain a total of 40 atoms (16 Ga, 16N, 4O and 4H atoms) along the (001)-direction, and (b) Top view of the slab.

Fig. 3-13 a and b show the surface slab used for calculating the relative surface energies of the GaN system with oxygen atoms at the interface. The surface is constructed perpendicular to the c-plane (or (001)-direction) and it consists of a total of 40 atoms – 16 gallium, 16 nitrogen, 1 oxygen atom. Then the oxygen atom coverage will be increased to 50% (2 oxygen atoms) to examine the oxidation susceptibility with increasing of oxygen content. Afterwards, the lattice will be rotated to m-plane and then a-plane to repeat the same procedure. The surface energy will be compared for each of these planes.

4 Discovery of Ultralow Wear of Gallium Nitride

The prevalence of gallium nitride (GaN) in technological applications has rapidly expanded in recent years because of its remarkable optoelectronic properties [5]–[9]. Historically, innovations in material epitaxy and electronic devices have allowed GaN-based semiconductors to be implemented in power electronics [5] and solid state lighting (SSL) technologies [6]–[9]. Specifically, the improvements of the dislocation density in GaN [156]–[161] and p-type doping activation [162]–[164] were the primary driver of the III-Nitride SSL technologies. Recently, high efficiency III-Nitride-based SSL technologies [21], [22], [165]–[168] have been realized through understanding the connectivity of nanostructure, properties, and performance at both the basic physics and device scales, leading to recognition by the 2014 Nobel Prize in Physics [4].

Tremendous advances on the understanding of the optoelectronic properties of GaN-based materials, devices, and nanostructures are however in stark contrast to that of the understanding of mechanical properties in the GaN. The lack of the understanding of the mechanical characteristics of GaN results in relatively few innovations taking advantage of these properties for device applications; therefore, the understanding of the mechanical properties of GaN-based semiconductors is essential for opening up new applications. Specifically, the elastic constants of GaN have been investigated [96]–[99], resulting in wide utilizations for research concerning the lattice mismatch and piezoelectric polarization effect [20], [100], [101]. In addition, the mechanical properties such as the Young's modulus, hardness, and fracture toughness of GaN material have been extensively studied [102]–[107], providing essential information for various scientific applications requiring those experimentally obtained parameters. In comparison, the tribological properties of GaN and other III-Nitride materials are still lacking: there are no investigations of wear performance and mechanisms of GaN-based materials to our knowledge. The closest studies have been chemical mechanical polishing [122] and nanoscratch experiments [114], but these are still very different from sliding wear. GaN plays a key role in modern semiconductor industry; thus, it is crucial to understand its wear behavior and reliability.

We measured wear rates and friction coefficients of GaN using a microtribometer (Fig. 4-1a) to perform reciprocating, sphere-on-flat, dry sliding wear experiments. To our surprise, GaN has remarkable tribological properties, with wear rates from 10^{-9} to 10^{-7}mm^3/(Nm) (depending on a number of factors including environment, crystallographic direction; discussed below); this is approaching wear rates reported for diamond (K ~ 10^{-9} to 10^{-10}mm^3/(Nm)), which has been reported as the hardest and most wear resistant material [169], [171]. In fact, when performing wear measurements of unknown materials, we typically slide for 1,000 cycles, then measure the wear scars; experiments had to be increased to 30,000 reciprocating cycles to be measurable with our optical profilometer. Furthermore, the large range in wear rates (~2 orders of magnitude) depending on sliding conditions and orientations are surprising and can provide insight into the wear mechanisms of GaN. It is also important to note that GaN is the only visible light emitting semiconductor that possesses low wear rate up to our knowledge, further implying the strong potential of implementing GaN in prospective applications.

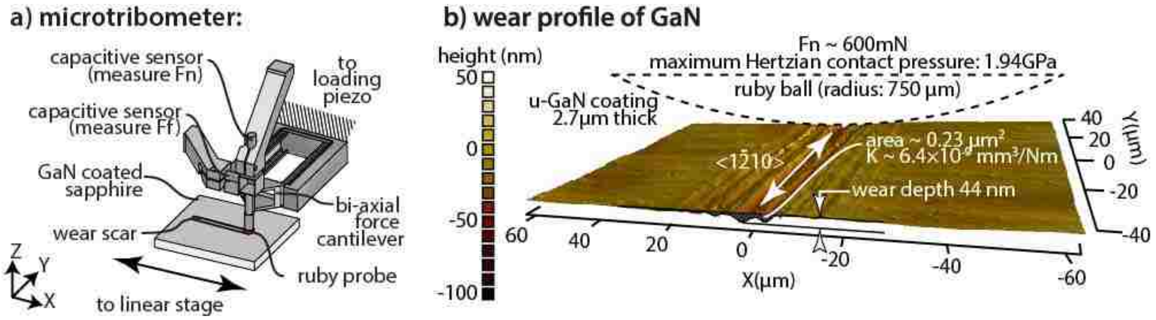

Figure 4-1 a) Micriotribometer; b) Profilometric scan on u-GaN wear scar.

Besides GaN, other allied III-Nitrides are also of interests. Band gap of III-Nitride family spans several electron volts. By alloying different element with different content into the base material to form ternary composite, people can easily fit the band gap between the binary composite. Furthermore, due to the less lattice mismatch between ternary composite and its corresponding binary composite (*e.g.*, GaN and InGaN), alloying of elements from same group has also been widely used in strain engineering area to minimize the strain and dislocation density. For the mechanical perspective, although indium and gallium are both group 13 metals, the hardness of indium nitride is much lower than gallium nitride [194]–[196]. Because of this, one would expect the wear performance to be worse for InN than GaN. We conducted reciprocating wear experiments on an InN thin coating (thickness is around 240 nm) along $< 1\bar{2}10 >$ to measure the wear rate of this relatively softer material. The applied normal load was reduced to 300mN (estimated Hertzian contact pressure ~ 1GPa) to insure the contact pressure is below the hardness of InN (H ~ 3-11GPa [194]–[196]). The wear experiments were conducted inside a glovebox with relative humidity of 20% RH. We found a wear scar with depth of ~ 90nm after 500 reciprocating sliding cycles (corresponding wear rate of K = 2600×10^{-9}mm^3/(Nm) which is almost two orders of magnitude higher than u-GaN. The coating was completely worn through after 1,000 sliding cycles (as opposed to 30,000 cycles to produce measurable wear on the GaN). However, there is still an opportunity to balance optoelectronic properties with wear properties using InGaN coatings. By replacing 17% of gallium atoms with indium atoms to form the $In_{0.17}Ga_{0.83}N$ alloy, the wear rate of this alloyed thin coating (~200nm thick epilayer), was $K_{<1\bar{2}10>}$ ~ 92 × $10^{-9}mm^3$/(Nm) (20% RH air, using 0.75mm radius ruby probe with 600mN applied normal load). This is approximately double the wear rate of GaN at 20% in the $< 1\bar{2}10 >$ direction, (K ~ 49 ×$10^{-8}mm^3$/(Nm) (Fig. 4-2). While the substitution of 17% Ga with In appears to be a large increase in wear rate, it is still fifty times lower than the wear rate of pure InN; this points to the opportunity to optimize coatings by balancing optoelectronic properties with wear properties using InGaN alloys. Furthermore, if the correlation between hardness and wear rate with changing group 13 cation persists, there is a clear benefit to pursue studies in wear of AlN or even attempts to stabilize wurtzite BN alloy coatings.

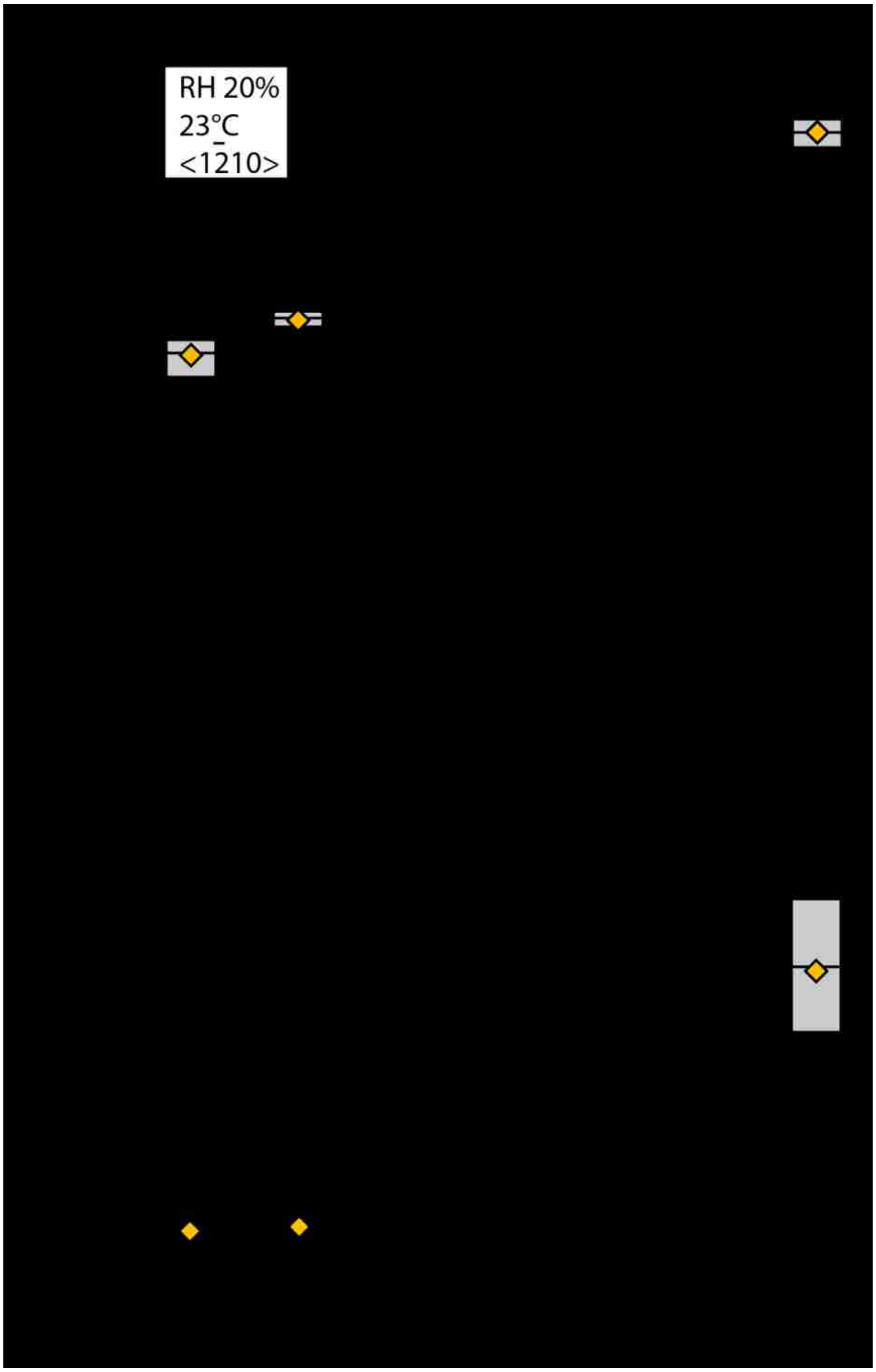

Figure 4-2 Wear rates of u-GaN, $In_{0.17}Ga_{0.83}N$and InN along $< 1\bar{2}10 >$ direction as a function of In content (x) for $In_xGa_{1-x}N$ coatings; plotted in log-linear (a) and linear-linear (b) for visualization.

4.1 Motivation: Newly Discovered Tribological Phenomena

The initial study on tribological properties of GaN resulted in more questions than answers. The following phenomena were discovered and motivate the rest of this dissertation.

4.1.1 Crystallographic Orientation Dependency

The pioneering work on anisotropic tribological properties of crystalline materials has been done in 1960's [197]–[200]. In this study, we test the wurtzite GaN coating in two different crystal directions, $< 1\bar{1}00 >$ and $< 1\bar{2}10 >$, to examine the anisotropy of friction and wear of this material. Wear experiments were performed on the (0001)-plane of GaN coatings grown epitaxially with metalorganic chemical vapor deposition (MOCVD) on single crystalline sapphire wafers. The average wear rates of GaN along $< 1\bar{1}00 >$ and $< 1\bar{2}10 >$ sliding directions were K ~ 9.3 $\times 10^{-9}$mm^3/(Nm) (N≥ 3) and K~ 31$\times 10^{-9}$mm^3/(Nm) (N≥ 3), respectively [Note: Each reported average wear rate comes from mean of all experiments for a given condition, each individual experiment (N=1, single wear scar) has n = 54 individual wear scans along the wear scar]; a difference of approximately three fold was observed, as shown in Fig. 4-3. These were obtained by linear reciprocating sliding test in nitrogen environment on 2.7µm thick unintentionally doped GaN (u-GaN) coating with a 1.5mm diameter alumina (ruby) probe. It should be noted that the wear scar was unresolvable (K<10^{-9} mm^3/(Nm)) in the dry nitrogen environment for 3 $< 1\bar{1}00 >$ and 2 $< 1\bar{2}10 >$ experiments, further highlighting GaN's potential as an ultralow wear material. As a comparison, sapphire has a hardness averaging ~ 25 GPa [201]; in the nitrogen environment, GaN is more wear-resistant than sapphire in these two crystal directions - $K_{sapphire,<1\bar{2}10>}$~ 2.6×10-

^{8}mm^{3}/(Nm) and $K_{sapphire,<1\bar{1}00>}$ ~ 3.6×10^{-8}mm^{3}/(Nm) (N = 2 for each). Of note, the orientation dependence of sapphire is not distinguishable from the current experiments, although there is possibly a subtle orientation dependence (previously reported by Steijn [199]) that is similar to the GaN trend.

The profilometric scans of example wear tracks for u-GaN (Fig. 4-3a and b) and sapphire (Fig. 4-3c and d) in both for $< 1\bar{1}00 >$ and $< 1\bar{2}10 >$ directions exposes differences in the wear rates of the different directions and materials. The wear track for one experiment on GaN in the $< 1\bar{1}00 >$ direction (single experiment wear rate of 6.4×10^{-9}mm^{3}/(Nm)) is 44nm after 30,000 reciprocating cycles (60,000 sliding passes), which indicates an average of 0.007Å has been removed per sliding (Fig. 4-1b). That is statistically one atomic layer removed every 700 reciprocating cycles.

Wear of the ruby balls were also examined after the wear tests. The results indicated that the wear of the ruby probes slid against GaN averaged around 9×10^{-9}mm^{3}/Nm with a standard deviation of ~ 6 × 10^{-9}mm^{3}/Nm. The wear rate of the ruby probe sliding against ~ 4×10^{-9}mm^{3}/Nm, within the standard deviation of the wear of the probe for GaN. The average combined uncertainty of the measurement is ~ 3 × 10^{-9}mm^{3}/Nm. The wear of the ball may vary due to the randomness of their orientation relative to the system.

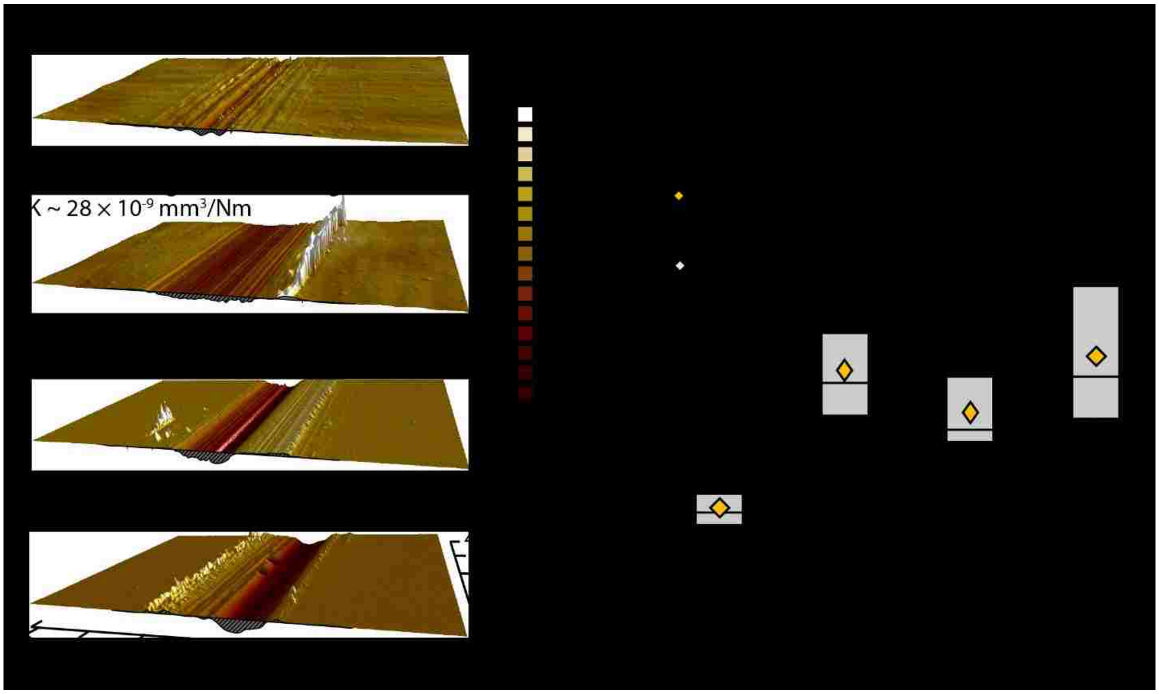

Figure 4-3 Profilometric scans of wear scars on (a) u-GaN along $< 1\bar{1}00 >$; (b) u-GaN along $< 1\bar{2}10 >$; (c) sapphire along $< 1\bar{2}10 >$ and (d) sapphire along $< 1\bar{1}00 >$; wear rate for individual example scan provided with wear track profile. (e) Wear rates for each testing condition (N= 2 to 3, not including wear scars that were too small to measure). Wear rate statistics in *e* represent datasets of n = 54 wear measurements along each wear experiment for a total of N*n datum per dataset for a given parameter set.

<u>Questions:</u>

From the preliminary results (Fig. 4-3), we can see that the wear rate of GaN depends on the sliding direction. However, what causes this directionality of wear rate of GaN? Why the $< 1\bar{1}00 >$ has the lowest wear rate? Will the wear rate of GaN vary periodically due to its single crystal wurtzite structure? Chapter 5 will explore these questions and explain the physics behind the directionality.

4.1.2 *Environment Effect*

Dry nitrogen is not the only environment of interest for the wear behavior of GaN; humid air is a prevalent environment, as such it is also of interest. Our custom microtribometer is housed in a glovebox that can be backfilled with either nitrogen or humid air to examine if the sliding environment will affect the wear behavior of GaN. The oxygen was <0.1 PPM and the H_2O was <1 PPM for the nitrogen environment while the water was varied between ~5,600 PPM (RH 20%) to 14,100 PPM (50% RH) for the humid air environment. However, in all cases, including dry nitrogen, the system was not heated to remove adsorbed water. Fig. 4-4 shows the wear rates of u-GaN in both dry nitrogen environment and humid air. There is a strong dependence of wear on relative humidity, with average wear rates (N>3) increasing approximately two orders of magnitude in the $< 1\bar{1}00 >$ direction from $K_{<1\bar{1}00>}$ ~ $9.3 \times 10^{-9} mm^3/(Nm)$ (dry nitrogen, N = 3 measurable [Note: An additional 3 experiments (N=3) were performed with unmeasurable wear scars]) to $K_{<1\bar{1}00>}$~ $770 \times 10^{-9} mm^3/(Nm)$ (50% RH, N = 6). The trends of wear being a function of crystallographic directionality is preserved in humid environment with mean wear rate increasing from $K_{<1\bar{1}00>}$ ~ $21 \times 10^{-9} mm^3/(Nm)$ to $K_{<1\bar{2}10>}$ ~ $49 \times 10^{-9} mm^3/(Nm)$ for 20% RH, from $K_{<1\bar{1}00>}$ ~ $240 \times 10^{-9} mm^3/(Nm)$ to $K_{<1\bar{2}10>}$ ~ $450 \times 10^{-9} mm^3/(Nm)$ for 35% RH, and from $K_{<1\bar{1}00>}$ ~ $770 \times 10^{-9} mm^3/(Nm)$ to $K_{<1\bar{2}10>}$ ~ $950 \times 10^{-9} mm^3/(Nm)$ for 50% RH.

Coefficient of friction, μ, of GaN was recorded in different humid environments. For the "run-in" period (initial sliding period with transient tribological properties) in the dry nitrogen environment, the friction coefficient generally went up from ~ 0.25 to ~0.4 first. Then, friction dropped down to ~0.35, where it remained for the duration of sliding, as shown in Fig. 4-5. The authors speculate that this relatively high friction coefficient may due to the existing oxide layer on the surface. With continuing of the test, the GaN was gradually exposed and interacted with the countersample. As such, we can see the friction coefficient centering around ~0.35. On the contrary, the friction started low at μ ~0.15 and then went up to μ ~ 0.2-0.28 for all the tests in lab air. We speculate that the relatively low friction during the first few cycles attribute to the adsorbents (*i.e.* water, adventitious carbon, oxygen) and reacted species on the GaN surface (possibly hydroxyl groups and oxides). The increasing of the friction during the "run-in" period might be due to the removal of these surface contaminations and oxide layers, exposing GaN. After the "run-in" period, the wear test fell into a relatively stable stage where the ruby probe slid against the mixture of newly formed gallium oxide/hydroxide and GaN. The results also showed that the friction coefficient will not change much when sliding along different crystal direction in the humid air environments, but there is noted friction anisotropy for the dry nitrogen environment (Table 4-1).

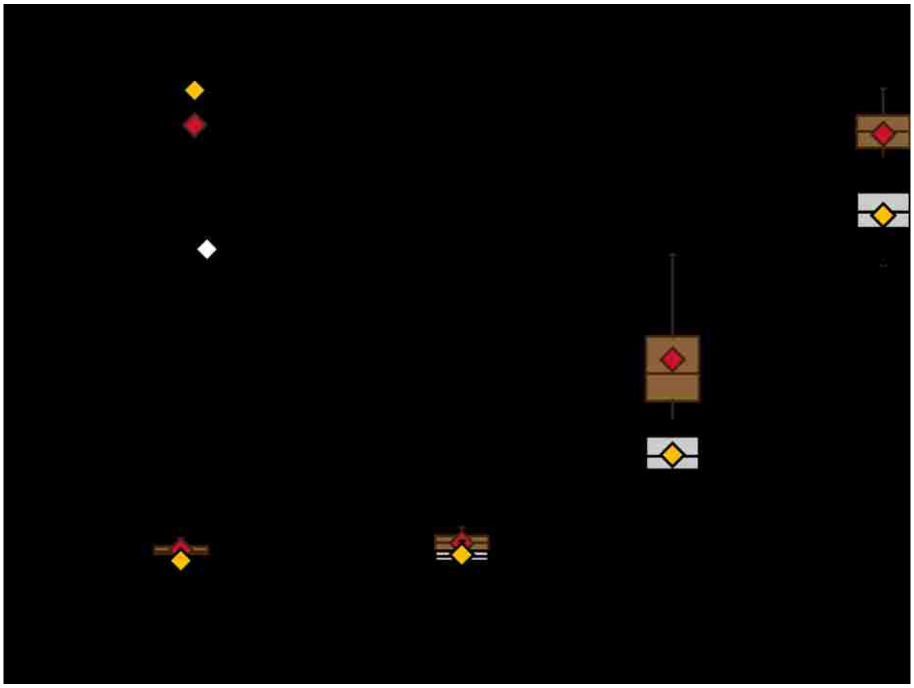

Figure 4-4 Wear rates of u-GaN in different environments (dry N_2, 20%RH, 35%RH and 50%RH).

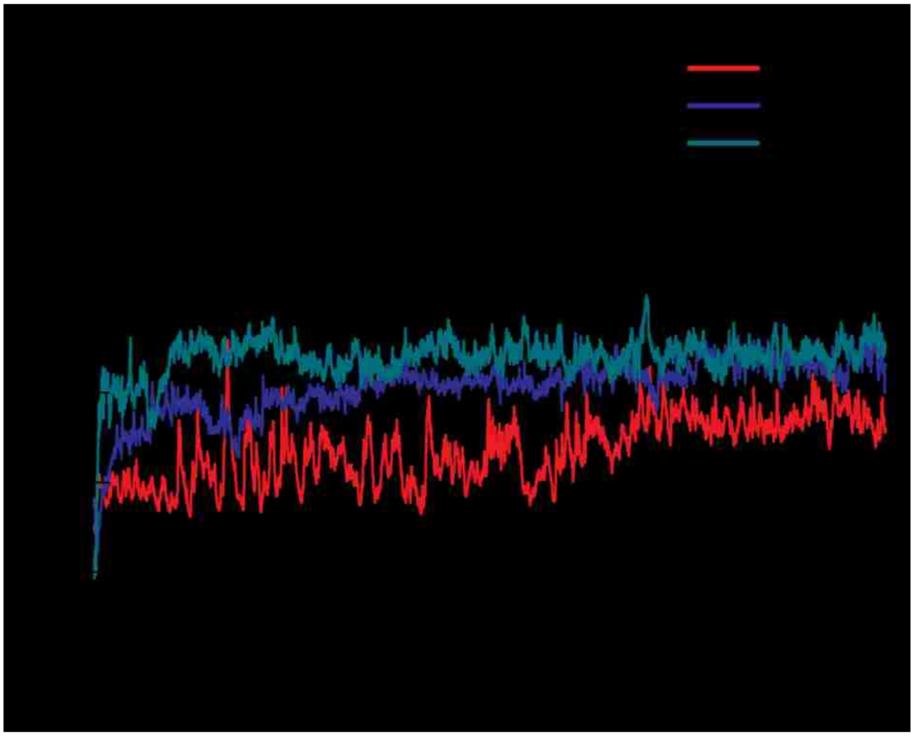

Figure 4-5 Coefficient of friction under different environments.

Table 4-1 Coefficient of friction along different sliding directions and environments

environment		$\mu_{<1\bar{2}10>}$	$\mu_{<1\bar{1}00>}$
nitrogen	**< .5 % RH**	0.35	0.31
air	**20 % RH**	0.21	0.23
	35 % RH	0.26	0.25
	50 % RH	0.28	0.27

Questions:

Moisture effect on wear performance of engineering materials has been studied for decades. In our case, the wear rate of GaN is significantly influenced by humidity, spanning more than an order of magnitude from dry nitrogen environment to humid environment (50 %RH lab air). We hypothesize that the tribochemical reaction between water molecule and GaN surface causes this humongous variation in GaN wear rate. Thus, how water molecules interact with GaN surface is the main question we need to answer.

4.1.3 Shear-induced Band Bending

XPS is a powerful tool to analyze the chemical state of a given surface, with the capability of probing the top 6-8 nm surface layer. We employed the XPS to interrogate the surface composition after testing under different environments. To our surprise, the preliminary results showed a lower binding energy shift, which means reduction of GaN towards metallic gallium. More discussions about this finding can be found in Chapter 7.

Questions:

Based on the design and working principle of XPS, this technique is used for determining the chemical state of the material. Thus, higher binding energy shift means the chemical state that newly formed is more stable (*e.g.*, oxidation), vice versa, lower binding energy shift means the chemical state is less stable (*e.g.*, reduction). How come under humid environment with large stress presented, GaN can be reduced instead of oxidized is the main question we have in this study.

5 Crystallographic Orientation Effect on GaN Wear

Investigations of anisotropic tribological properties of crystal materials starting from 1960s and various crystal materials have been studied since then [151], [197]–[200], [202], [203]. Bowden et al observed that friction coefficient of MgO_2 and diamond exhibited a 90° symmetry while with larger cone angles the friction coefficient decreased but the directionality was still preserved [197], [203]. Similarly, Steijn concluded that friction and wear properties of single crystals with FCC and BCC structures, like copper, iron, NaCl, LiF, etc., depended on crystal orientation [198]. And for HCP crystal like sapphire, wear rate on basal plane along $[11\bar{2}0]$ was lower than $[10\bar{1}0]$ [199]. After these pioneering works on anisotropic friction and wear properties, more efforts have been made in exploring directionality of tribological properties for various kind of materials [204]–[213]. As aforementioned, wear rate of GaN exhibits a strong directionality. In order to map the full orientation dependence of GaN wear performance, we employ a custom-type pin-on-disk rotary tribometer to conduct unidirectional rotary test to include all the crystal directions. It has been shown in Fig. 3-12 that, $<1\bar{2}10>$ family direction is symmetric while the $<1\bar{1}00>$ family direction is asymmetric. Thus, unidirectional rotary sliding tests (including clockwise and counter-clockwise directions) were performed on (0001)-GaN coating to distinguish the asymmetric in $<1\bar{1}00>$ family direction. In addition, a molecular static model was built to simulate the free energy variation when dragging wear cluster around the surface (in Chapter 3-3). The simulation results provided us with insightful information to look into the physics behind the wear process.

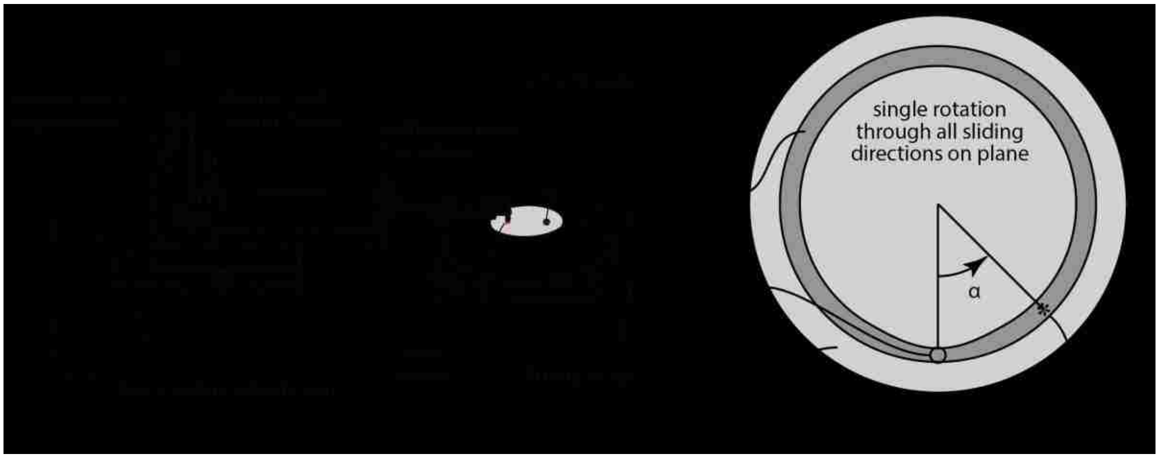

Figure 5-1 (a) schematic of rotary tribometer, (b) schematic of unidirectional sliding test.

5.1 *Experimental and Simulation Methods*

Unintentionally doped single crystal (0001)-plane GaN coating (3 µm thick, grown by metal organic chemical vapor deposition on c-plane single crystalline sapphire) was used in these experiments. The as-grown u-GaN sample has background doping (n-type) of $n \sim 5 \times 10^{16}$ cm^{-3}. The rotary wear tests were performed by our custom rotary tribometer (Fig. 5-1a) mounted inside a glovebox to achieve the environment control (25% - 30% RH lab air). Two force transducers attached to the flexure were used to measure the normal and frictional forces. The linear sliding speed was set to be 20 mm/s and the sliding cycles was 30,000. A single crystal ruby ball (α-alumina) with radius of 1.5 mm (Swiss Jewel Company, Grade 25) was used as the countersample due to its hardness and wear resistance. The applied normal load was set to be 600mN (~1.2 GPa maximum Hertzian contact pressure, approximately 1/10 of the hardness of GaN [102]–[106]). The rotary wear test was first performed in a unidirectional (clockwise) manner for obtaining the wear rate corresponding to each crystal direction, then a second unidirectional rotary test was performed 1mm away from the first test with a reversed direction to distinguish the symmetry of wear behavior of wurtzite GaN. The tribometer was mounted inside a glovebox to guarantee the testing environment being strictly maintained around 30% RH. Optical profilometer (Bruker ContourGT-K) was used here to measure the cross-sectional area of the wear scar. The rotary stage carrying the sample was placed underneath the profilometer for wear scar profile measurement. Stage rotated every 3° for profilometer to make a profilometric scan. Then Archard wear rate was used for deriving the wear rate, as described in Chapter 3. Five line scans within each single profilometric scan were made to get data that is statistically representative of the local material wear properties [214].

In addition to rotary test, a molecular static simulation was also carried out to understand the physics of crystal orientation dependence (Chapter 3-3).

5.2 Rotary wear test

Unlike the linear reciprocating sliding test performed in Chapter 4, the unidirectional rotary sliding test not only includes all the crystallographic directions, but can also distinguish the possible asymmetry within each family directions. From Fig. 5-2, we can see that, the wear rate of GaN exhibited a strong orientation dependence, with periodicity of 60°. The lowest wear rate was at $<1\bar{1}00>$ family direction ($K_{<1\bar{1}00>}$ = 6.7×10^{-8} mm^3/Nm ± 0.92×10^{-8} mm^3/Nm) and the highest wear rate can be found at $<1\bar{2}10>$ family direction ($K_{<1\bar{2}10>}$ = 14×10^{-8} mm^3/Nm ± 2.7×10^{-8} mm^3/Nm). Profilometric scans along this circular wear scar revealed a continuous variation of wear rate with orientation. This periodic crystallographic dependent wear behavior matches with what we reported previously that <1$\bar{1}$00> direction was more wear resistant than <1$\bar{2}$10> direction [126]. The inconsistency of the wear rate within same family direction is either attributed to the local quality of the GaN sample or a possible asymmetric within the same family direction. In order to answer this question, another unidirectional wear test with reverse sliding direction (counter-clockwise) was made on the same coating 0.5 mm away from the first unidirectional test. This is to guarantee a comparable local sample quality and allow us to differentiate the possible asymmetric wear behavior within same family direction. As plotted in Fig. 5-2b, we can see that the wear rate was very close to the first test with only limited increase of wear rate for all directions.

In addition to wear rate, friction coefficient also exhibits an obvious crystallographic orientation dependence with same 60° periodicity, having its lowest value along <1$\bar{2}$10> and highest along <1$\bar{1}$00> (Fig. 5-3), except for the region around starting point of the test, which was attributed to the discontinuity of the stage near this point (acceleration and deceleration of each cycle). This periodicity does not come from variation in the normal load, which, for this experiment, typically has a ±7 mN (less than 2%) variation with periodicity of 360º, caused by slight misalignments; the friction coefficient is normalized as the instantaneous friction force divided by the instantaneous normal force. We hypothesize that a possible anisotropic energy barrier distribution is presented on the surface, which is caused by the intrinsic lattice structure of GaN.

To verify this hypothesis, we performed a molecular static simulation to look into the surface energy and energy barrier distribution on Ga-terminated surface.

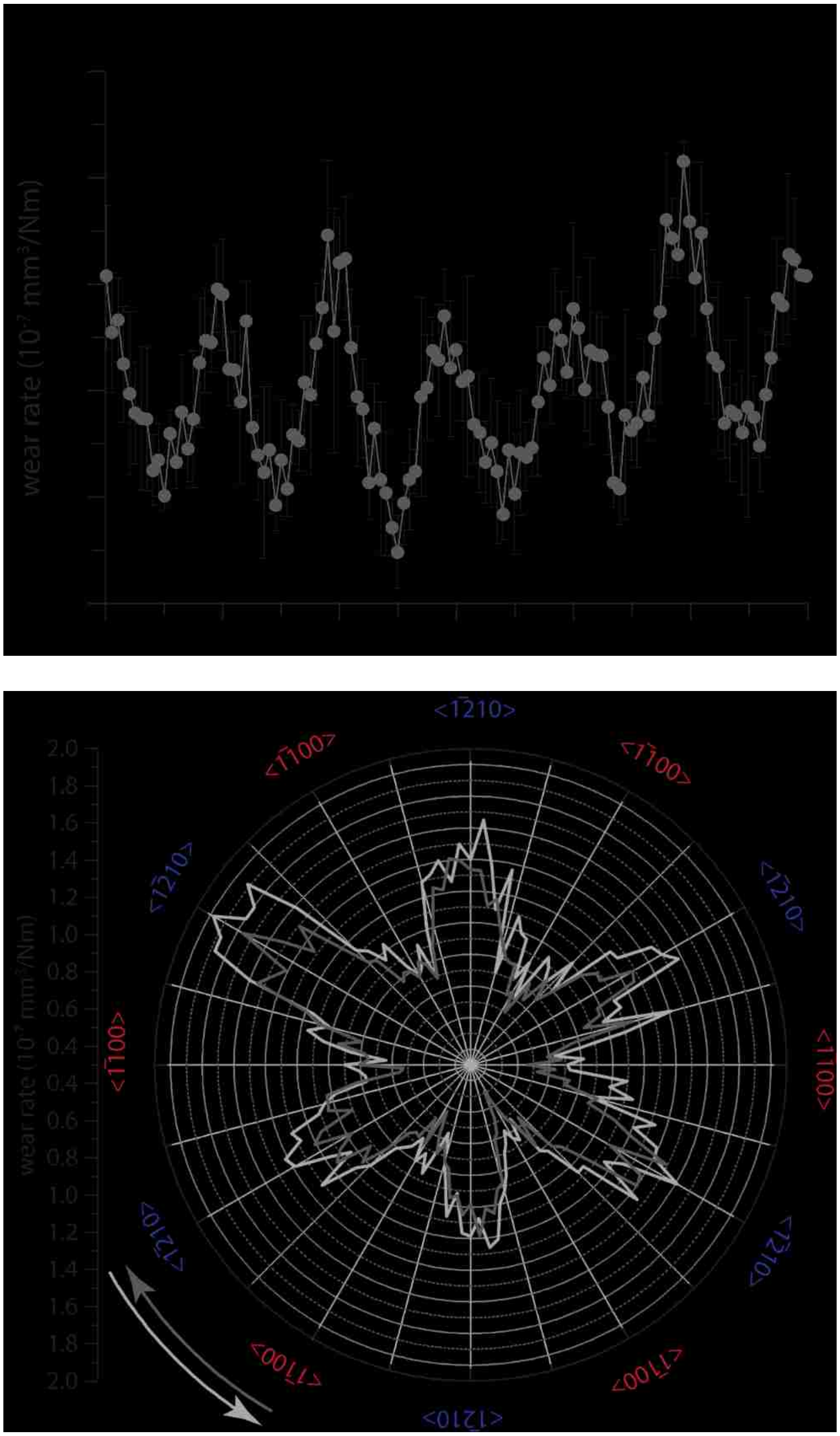

Figure 5-2 (a) Wear rate for clockwise unidirectional sliding test in Cartesian coordinates; (b) clockwise and counter-clockwise unidirectional sliding tests in polar coordinates.

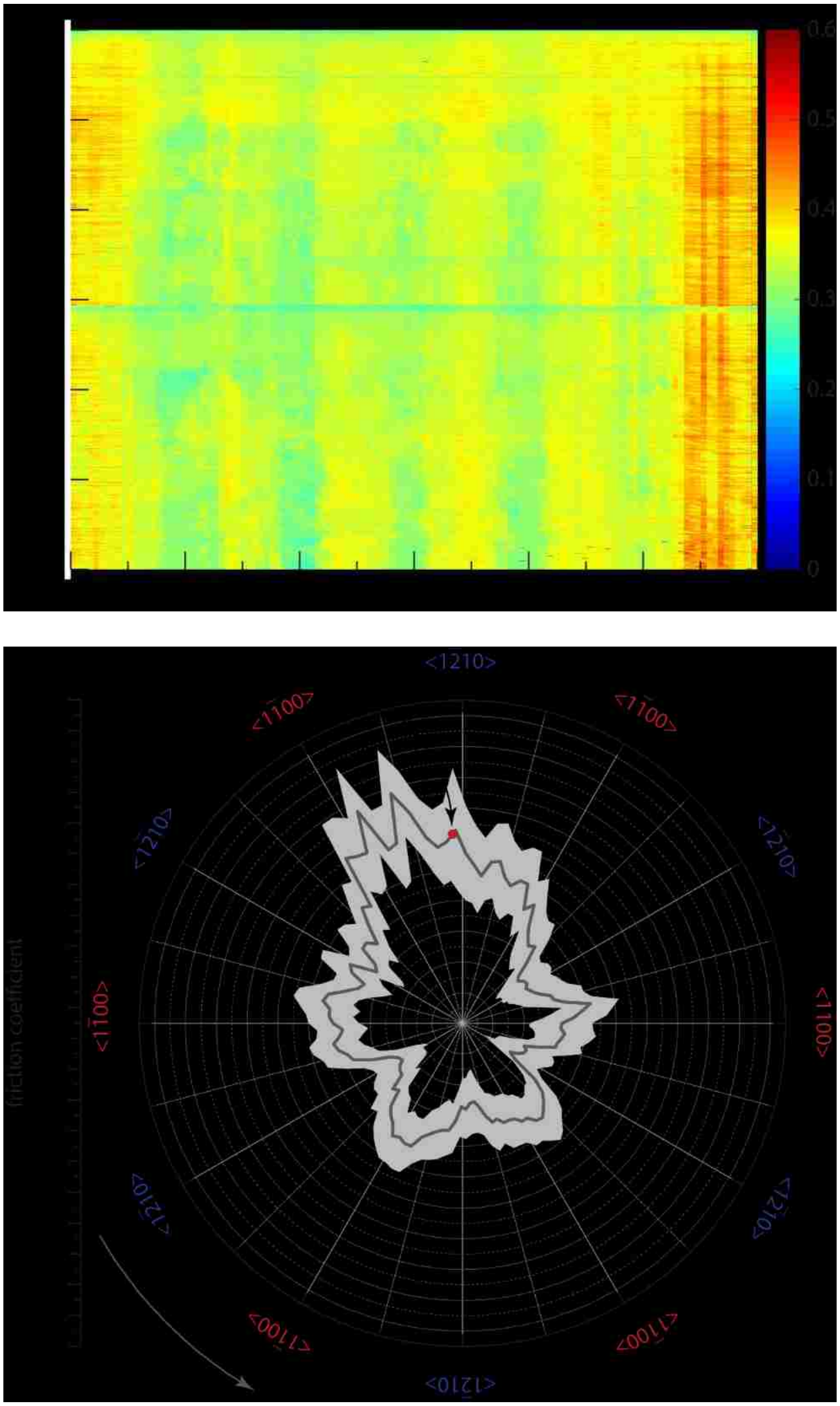

Figure 5-3 (a) friction coefficient map of counter-clockwise unidirectional sliding test; (b) average friction coefficient of 30,000 cycles with standard deviation highlighted as light gray.

5.3 Molecular Static Simulation

Unlike prior results for frictional and wear anisotropy [197], [199], [203], GaN is under a very mild wear regime and plasticity is not expected to contribute. As previously reported, height removal rate for GaN is as low as ~ 0.0007 nm per sliding cycle [126]. To explain this, we propose a mental framework that considers the removal/sliding of a small, charge balanced GaN cluster. We hypothesize that higher energy barrier along <1$\bar{1}$00> direction results in more difficult removal process of the material, which in turn results in lower wear rate. The anisotropy of friction coefficient is much more subtle than the anisotropy of wear. The anisotropy in friction likely comes from the same or similar energetic barriers derived from crystalline structure that governs wear.

To test this hypothesis, we employed molecular static calculation to understand the physics of crystal orientation dependence of wear. For simplicity, we only considered wear as the internal bond breaking within the GaN surface. Thus, only GaN-GaN interface will be simulated. Although, this model is simplified and does not strictly correspond to the complexity of the experiment, the energy barrier distribution can be used to correlate with the anisotropy of GaN's wear performance. Details of this MS simulation can be found in Chapter 3-5.

The molecular static simulation results revealed 60° periodicity on c-plane surface, with energetic barriers to sliding strongly linked to the sliding direction. This supports our hypothesis that the crystallographic orientation dependences of wear rate is attributed to the anisotropic energy barrier distribution on the c-plane surface of GaN. From Fig. 5-4, we can see that there are less energy barriers along <1$\bar{2}$10> family direction while more energy barriers along <1$\bar{1}$00> family direction. This indicates that more work is required to overcome the energy barriers along the <1$\bar{1}$00> direction, resulting in lower wear rate. On the contrary, less energy barriers make the wear cluster more free to pass along the <1$\bar{2}$10> direction, leading to increased wear rate in this direction (Fig. 5-4a). We also plot the energy variations along specific crystallographic directions (Fig. 5-4b). Higher energy barrier height in <1$\bar{1}$00> than in <1$\bar{2}$10> means it is more difficult to drag a wear cluster along <1$\bar{1}$00> family direction, again demonstrating that <1$\bar{1}$00> family direction has a lower wear rate than <1$\bar{2}$10>. It is also noteworthy that the crystal structure along <1$\bar{2}$10> family direction strictly repeats every 60° while the crystal structure in <1$\bar{1}$00> is exact the same every 120°, but varies a little every 60° (Fig. 5-4b). To specify this point, we looked into the crystal structure of GaN (Fig. 3-12) and saw that when moving along [1$\bar{1}$00] direction, the wear cluster will approach one Ga atom first and split two other N atoms afterwards. On the contrary, when moving along [$\bar{1}$100] (the opposite direction) the wear cluster will split two N atoms first then approach the next Ga atom. This slight difference is due to wurtzite layers cycling among two equivalent shifted layers; we suspect that there is no anisotropy in wear between these two directions, as this effect is averaged out as the material is worn through multiple layers. Theoretically speaking, this anisotropy in <1$\bar{1}$00> family direction could exist instantaneously and in atomic-scale wear events and experiments. However, it is important to note that the wear behavior of GaN is influenced not only by crystal orientation, but also highly depends on the humidity, as well as the local sample quality, which makes it extremely difficult to demonstrate this theoretical calculation with macroscale wear test.

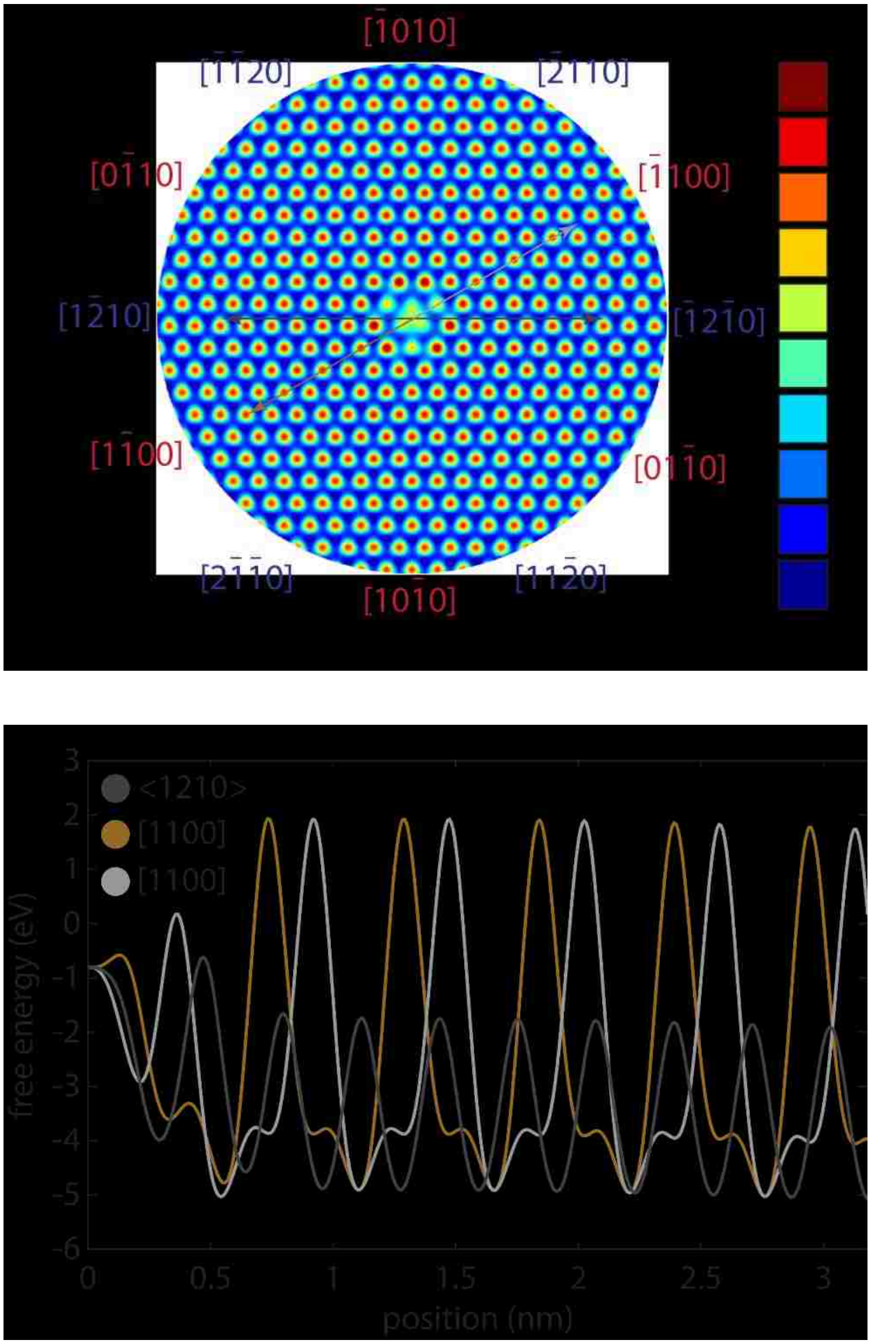

Figure 5-4 (a) Free energy variation of GaN wear cluster moving along the GaN surface; (b) line scans of the energy barriers along [$\bar{1}010$], [$\bar{1}100$]; [$\bar{2}110$] and [$\bar{1}2\bar{1}0$] overlapped and plotted as family direction <1$\bar{2}$10>.

6 Moisture Induced Wear Mechanism Transition of GaN

In addition to crystallographic orientation, moisture is also a pivotal factor that will markedly influence the wear performance of GaN, as mentioned in Chapter 4. Moisture effect on various materials has been studied for decades, including wear of glass [131], and mechanisms of moisture effect on fracture and wear performance of several ceramics, like Si, SiC, Si_3N_4, SiO_2, ZrO, Al_2O_3, GaAs, etc. [132]–[148] and ceramic filled polymers [149]–[152]. Wiederhorn published a seminal work on how moisture assisting crack growth on glass and sapphire [131]. He discovered that the measured crack propagation velocity was a function of stress and water vapor concentration. Gee looked into the tribochemical reaction during wear of α-alumina and pointed out that the wear rate of alumina decreased with the increasing of humidity, yet very little effect was found of humidity on its friction coefficient. They hypothesized that it was due to the formation of thin protective/tribochemical films of aluminum hydroxide at the interface [146], [148]. Ishigaki et al. performed a pin-on-disk sliding test under various environments, including dry nitrogen, 50% RH and 90% RH, to study the humidity effect on tribological performance (friction and wear) of hot pressed silicon nitride [133]. Their results indicated that the adsorbed water molecules enhanced the plastic flow of silicon nitride and reduced both friction and wear. Fischer and Mullins [140] applied Lewis acid theory to explain the tribochemical reaction occurring during the sliding contact with water vapor presence. They systematically analyzed the tribochemistry of several representative ceramics, *i.e.*, alumina, silicon nitride, silicon carbide and zirconia, and claimed that the interaction between two ceramics was dominated by charge transfer with ambient environment through acid-base reaction.

Erdemir et al. also employed Lewis acid and base and hard and soft acids and bases (HSAB) concepts to help understanding the role of water molecules during tribochemistry on certain solid oxides [141]. Murthy et al. investigated the influence of humidity on friction and wear of silicon carbide [142]. They found that the friction, wear rate and debris size and morphology changed depending on the humidity. Kim's group performed molecular dynamic (MD) simulation to look into the atomistic mechanism of humidity effect on tribochemical wear of silicon oxide [144]. Their results show that the tribochemical reaction occurs at the interface and oxidizes the silicon as a function of adsorbed water molecule amount. It is noteworthy that stress acts as a key role in assisting the chemical reaction [215] and cracking of ceramics under humid environment [216], [217]. However, the mechanism of stress corrosion cracking for most of the ceramics still remains unclear [218].

GaN and other III-Nitrides have gained interest as electromechanical materials for numerous device applications [219], [220]. These GaN-based devices, including RF-MEMS switches are used under various environments, including desert and space. It is necessary to understand its surface chemical property and wear behavior when interacting with water molecules, especially under contact condition where stress will be applied. Recently, the ultralow wear nature of GaN has been reported [126], and its wear performance was greatly influenced by humidity. However, the mechanism of humidity effect on GaN wear performance is not fully understood yet. Furthermore, understanding the mechanisms of material removal (*e.g.* wear, machining and polishing) of GaN surfaces will be relevant for device fabrication and polishing processes [122],

[221], [222], especially if subtle environmental factors (*i.e.* humidity) can control material removal rates as well as surface finish and chemistry.

In this chapter, we will look into the surface chemistry of GaN when tested under different environment, and a wear mechanism of GaN will be proposed.

6.1 Materials and Methods

6.1.1 Materials

Single crystal unintentionally doped GaN (u-GaN, 3μm thick) films were grown on c-plane sapphire by metal-organic chemical vapor deposition (MOCVD). The as-grown u-GaN coating has background doping (n-type) of $n \sim 5\times10^{16}$ cm^{-3}. [21], [22]. One MOCVD GaN grown wafer was cut into 4 samples. One sample was used for each environment, and three wear experiments were performed on each sample/environment for repeatability. All the samples are sonicated in acetone and then IPA both for 5 min, and blow the surface dry with ionized dry nitrogen to clean the surface and remove the particles due to sample cutting. Single crystal α-alumina ball (ruby, Swiss Jewel, Grade 25, 1.5mm diameter) was used as the countersample to reciprocate against GaN coating along $<1\bar{2}10>$ crystallographic direction as alumina is hard, chemically stable and commonly used as an abrasive material.

6.1.2 Sliding Test

All wear tests were carried out on custom ball-on-flat, reciprocating tribometer mounted inside a glovebox with controlled environment (as described in Chapter 3-1). Testing environments included dry nitrogen (<5 ppm H_2O and <1 ppm O_2), 10% RH

(± 5% RH) air, and 75% RH (± 5% RH) air. A cantilever with ruby probe (1.5mm diameter) attached was used to apply normal load onto the GaN coating. Strain-gauge based biaxial force transducer was used to measure the normal and frictional loads. The applied normal load was kept at 600mN ± 5mN (corresponding to ~2GPa maximum Hertzian contact pressure) in all sliding tests. 2 GPa was chosen to be low enough below hardness to not be doing a scratch test and perform a wear test. Onset of plastic deformation of GaN is ~10-11 GPa, so 2 GPa is adequately and arbitrarily low enough [223]. Material properties and working conditions are summarized in Table 6-1.

Table 6-1 Material properties and working conditions [103], [104]

Material Property			**Test Condition**	
	GaN	α-alumina	Sliding speed	5 mm/s
Young's Modulus	290±5 GPa	350±50 GPa	Relative humidity	Dry nitrogen, 10%, 75%
Poisson's ratio	0.25	0.25-0.3	Normal load	600 mN
Hardness	16±2 GPa	22±3 GPa	Sliding direction	<$1\bar{2}10$>

6.1.3 Wear Measurement

Topography of each wear scar was measured by scanning white light interferometry (Bruker ContourGT) to obtain the 3D height profile of the wear scar. The cross-section of the wear scar was extracted from profilometric scan to obtain the cross-sectional area of the lost volume; these were used to measure the Archard wear rate. Details of wear measurement can be found in Chapter 3-2.

6.1.4 Surface Analysis

Worn surface morphology was analyzed by scanning electron microscopy (SEM, ZEISS 1550) to compare the wear modes for different environments. Energy dispersive X-ray spectroscopy (EDS, Oxford Instruments) was applied to scrutinize the surface composition after the wear test. In addition, atomic force microscopy (AFM) was also employed to measure the microscale surface topography of worn surfaces obtained under all environments.

A TEM specimen was prepared by Ga-source focused ion beam milling (FIB, FEI Scios DualBeam). A 100nm electron beam assisted platinum followed by 2μm ion beam assisted platinum were deposited on the worn surface (75% RH testing environment) for surface protection. In order to remove the Ga ion implantation during the milling process, a two-step post-surface-cleaning process was conducted. The specimen was first exposed to the low current Ga ion beam (5KV, 47pA), then Ar ion cleaning (Fischione 1040 Nanomill) was performed to further remove the residual Ga ion implantation. Transmission electron microscopy (TEM, JOEL 2000) was utilized to image the defects formed underneath the worn surface for understanding the moisture effect on wear mechanism of GaN.

6.2 Wear Rate and Friction

Fig. 6-1 shows the wear rates of GaN under different testing environments and sliding cycles. We can clearly see that, from dry nitrogen to 10% RH low humidity lab air, there was only about a one-fold increase of the wear rate of GaN, from $K_{nitrogen}$ ~2.3×10^{-8} mm^3/Nm to $K_{10\%RH}$ ~4.2×10^{-8} mm^3/Nm. In the stark contrast, the wear rate of

GaN was averagely increased over 20 times when tested under 75% RH high humidity lab air environment, *i.e.*, $K_{75\%RH}$ ~54 × 10^{-8} mm^3/Nm. This is consistent to our previous report [126]. The wear rate for different testing environments clearly evidenced a humidity dependence of GaN wear performance. With testing environment changed from dry nitrogen (O_2 < 1 PPM, H_2O < 1 PPM) to low humidity lab air (78% nitrogen, 21% oxygen, 10%RH corresponding to ~2800 PPM), the wear rate only increased about two times. In the stark contrast, when humidity was the only factor that had been changed from 10% RH to 75% RH (corresponding to ~21,300 PPM), the wear rate of GaN had significantly increased over ten times. This indicates that moisture contributes to the wearing of GaN with the presence of mechanical contact. Density functional theory (DFT) and molecular dynamics simulations have been intensively applied to investigate the interactions at GaN-water molecule interface [40], [42], [224], [225]. It has been shown that the water molecules will dissociate into hydroxyl and hydrogen and bond to Ga and N, respectively. On the other hand, the increasing of the water coverage can also facilitate the crack propagation by lowering the surface energy of GaN [192]. As another aspect that tribology focuses on, friction coefficient, μ, provides additional insight into tribochemistry of this system. Fig. 6-2 shows the averaged friction coefficients for three testing environments. We can observe that in humid lab air environment (75% RH), the friction coefficients started at ~0.15 and gradually went up to ~0.3, where it stabilized at this value for the duration of the test. Low humidity environment is slightly different. For the "run-in" period, the friction coefficient also began with a low value of ~0.15, but went up directly to its highest 0.28, and then dropped back to a lower value of 0.2. Although, there are some increases of friction coefficient occurred during ~7,000 cycles and ~14,000 cycle, the friction coefficient kept at ~0.2 in the rest of sliding. For dry nitrogen environment, the friction coefficient started at ~0.2 and went up to ~0.8-0.9 in the “run-in” period. Then the friction coefficient remained between 0.8-0.9 in the following sliding cycles. The results were consistent with [126], which suggests the water molecules and hydroxyl groups acted as lubricants at GaN/alumina interface. Much higher frictional force (friction coefficient) in dry nitrogen also indicates a much larger shear stress applied onto the GaN coating, and this will correlate to the surface damage and wear mode that will be discussed below. It’s noteworthy that, besides the friction coefficient, the “noise” (variation of friction coefficient) of low humidity testing environment during the stable stage is much smaller when compared to dry nitrogen and high humidity environment. This indicates that something other than water molecules or hydroxyl groups formed during sliding for low humidity test, and further decreased and stabilized the friction.

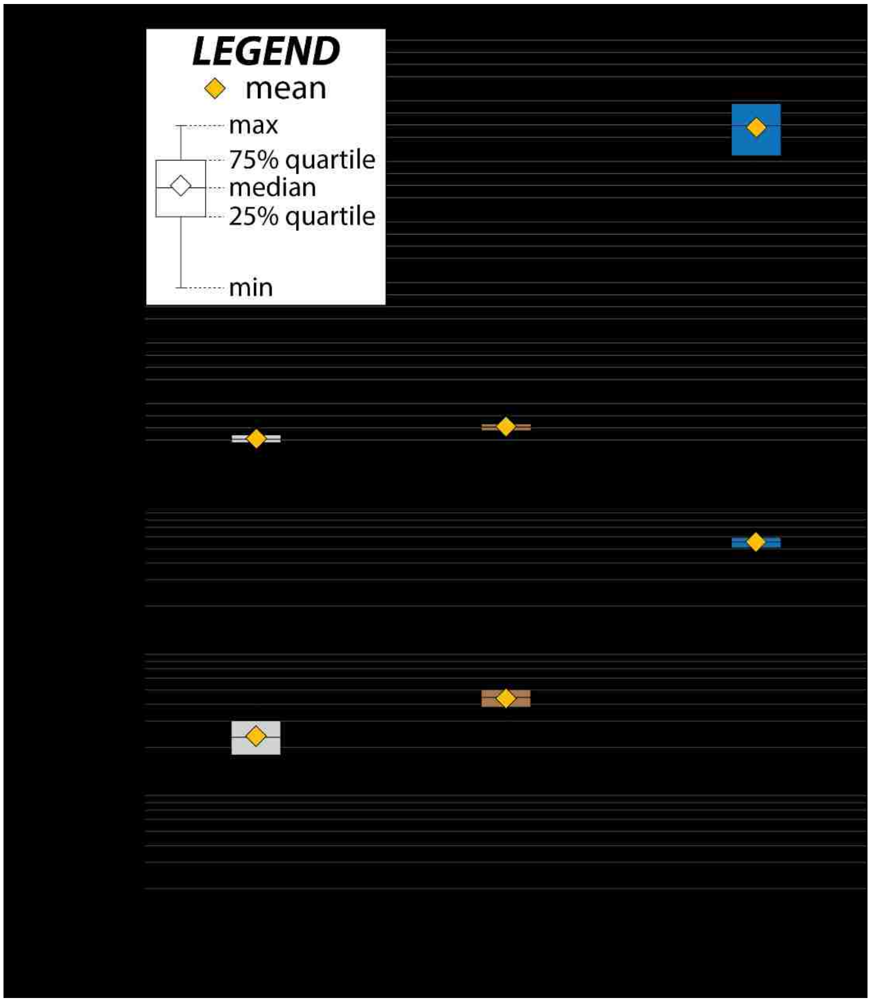

Figure 6-1 Wear rate of GaN under different environments (in linear scale and log scale).

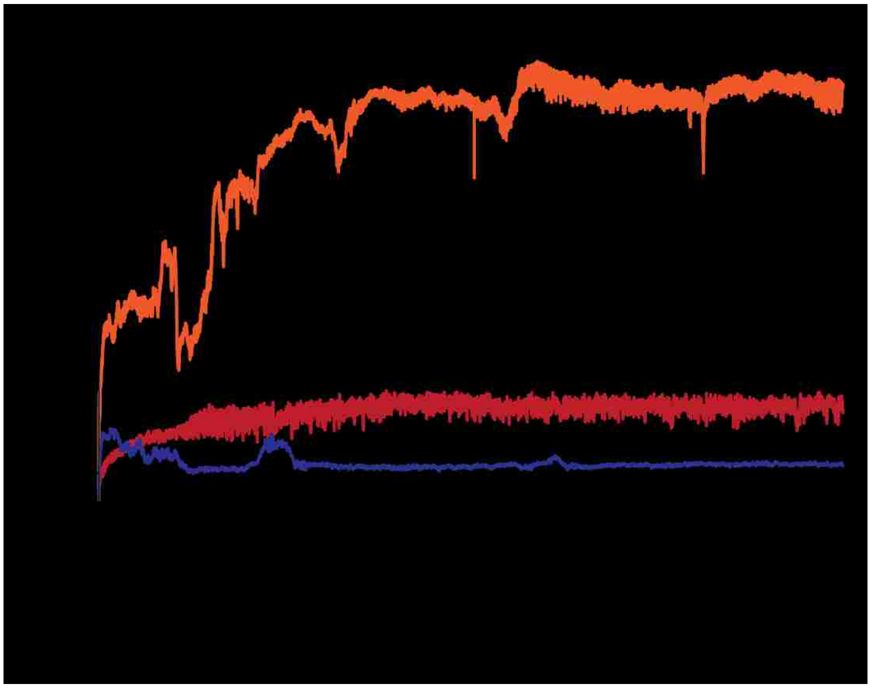

Figure 6-2 Friction coefficient of GaN tested under different environments.

6.3 Tribochemistry of GaN Under Different Environments

The SEM measurement (secondary electron mode) was utilized to image the microscopic morphology of these worn surfaces for wear mechanism comparison. As shown in Fig. 6-3 a, the worn surface from 75% RH testing environment exhibited a relatively smooth (in the direction of sliding) wear grooves in the surface after 30,000 reciprocating cycles. Both 10% RH (Fig. 6-3 b) and dry nitrogen (Fig. 6-3 c and d) environments had significantly smaller wear scars with less uniform damage features. For 10% RH lab air, small, periodic dark patches were found on the surface (Fig 6-3 b). Ridges (Fig 6-3 c) and ridges with potholes (Fig. 6-3 d) were found for wear scars from the dry nitrogen testing environment.

The ridges found in the worn surface obtained under dry nitrogen environment after 30,000 reciprocal sliding cycles indicates that the major mechanism of material removal is adhesive wear, i.e., bonding was formed between sample and countersample, and then ruptured by shear stress, which resulted in material transfer from one surface to the other, as well as material fatigue. Furthermore, when the sliding cycles increased to 50,000 cycles, dark potholes were engendered on the surface, as shown in Fig. 6-3 d. This finding suggests a possible wear debris formation mechanism in dry nitrogen environment, *i.e.*, strong adhesion leads to much higher friction and material fatigue, which eventually causes the material to be knocked out by the ruby probe. Instead, the difference in morphology and defect type from the other two worn surfaces (10% RH and 75% RH) suggested different contact modes in each case. This can arise either from the variation of the shapes of both sample and countersample or the newly formed tribofilms during the wear test.

At 5 kV electron accelerating voltage, the electron penetration is ~200 nm in GaN, making EDS surprisingly surface sensitive [223]. Thus, EDS was performed on worn surfaces as well as countersamples to obtain further insight into the tribochemistry for this water-GaN-Alumina tribosystem.

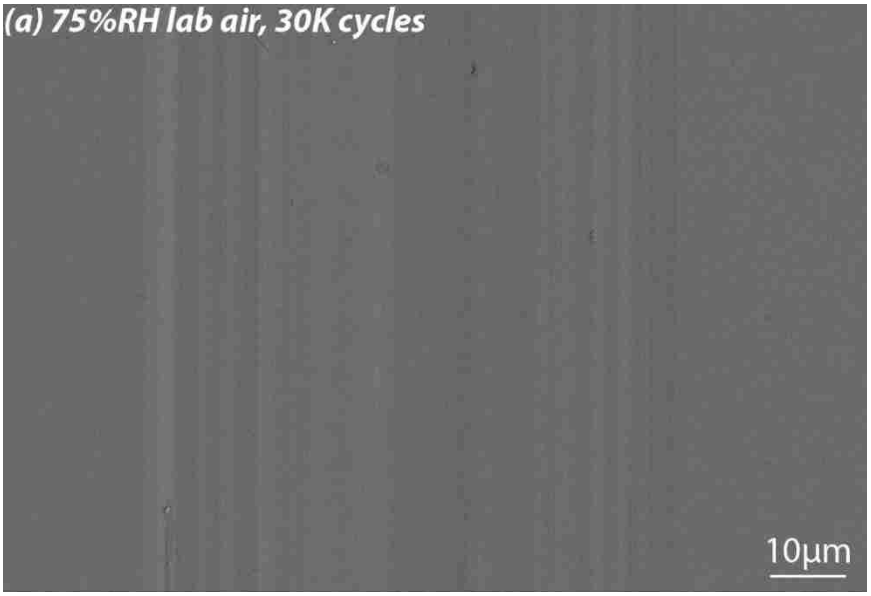
(a) 75%RH lab air, 30K cycles
10μm

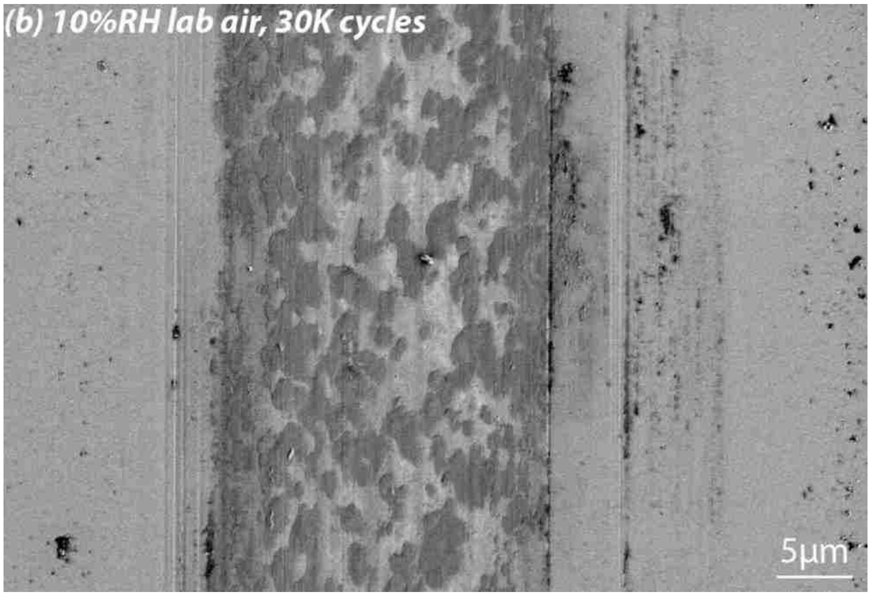
(b) 10%RH lab air, 30K cycles
5μm

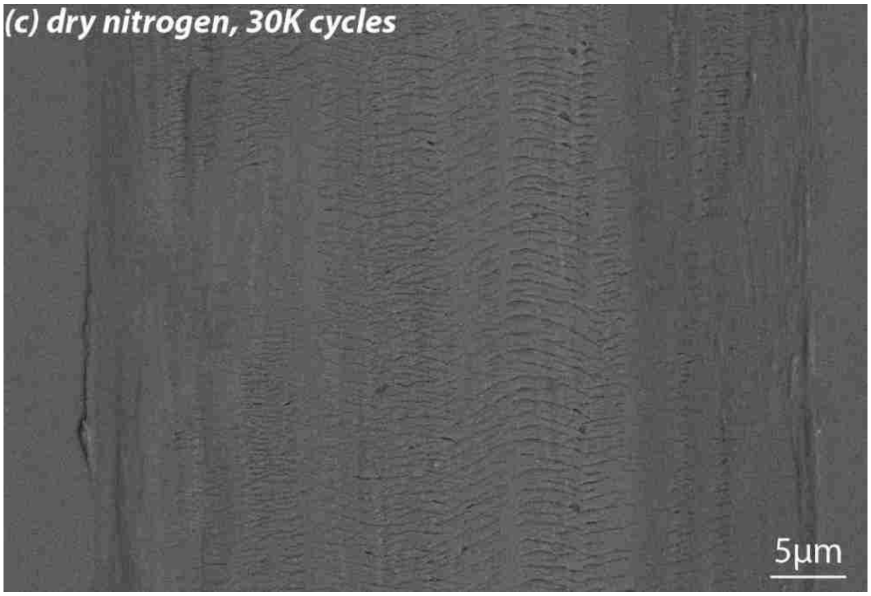

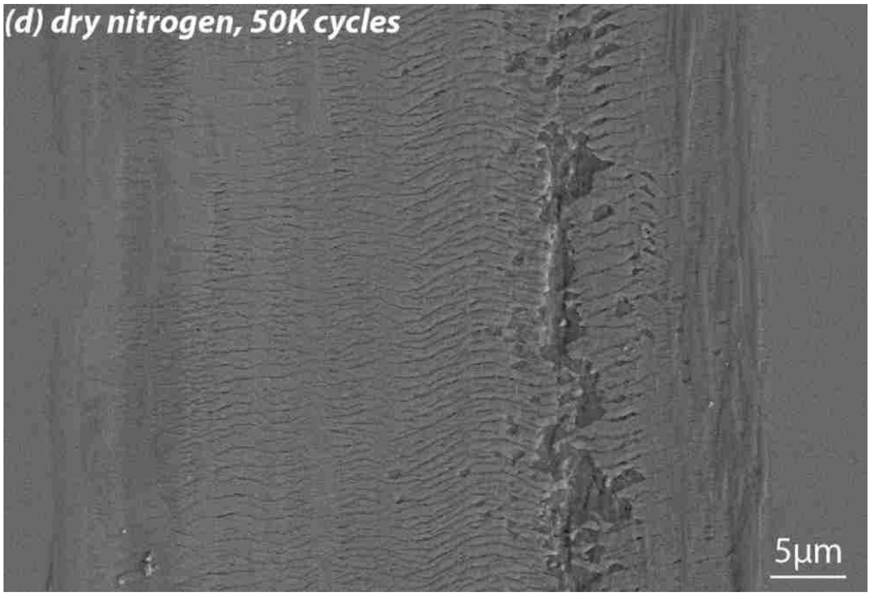

Figure 6-3 SEM images of wear scars tested under (a) 75% RH lab air; (b) 10% RH lab air; (c) dry N_2 after 30,000 cycles and (d) dry N_2 after 50,000 cycles.

From Fig. 6-4, it can be seen that the surface chemical composition revealed by EDS presented different chemical features for each worn surface. Abundant signals of oxygen centered at the ridges and potholes on the worn surfaces were found for dry nitrogen environments while deficient signals of gallium and nitrogen were found at the same area [Fig. 6-4(a-d)]. The relative intensity ratio of Ga/O for spot#1 and spot#2 are 5.28 and 59.32, respectively. Similarly, the ridge patterns on worn surface under dry nitrogen environment obtained after 30,000 cycles also exhibited discernible oxygen signals centering at the ridges [Fig. 6-4(e-h)]. As reported by Chin *et al.*, a-plane GaN is more susceptible to oxidation than c-plane [226]. Thus, we speculate that the newly formed ridges engendered new planes on the side, *e.g.*, a-plane and m-plane, which are more chemical active than c-plane and easier to be oxidized during the sample transfer from dry nitrogen environment to SEM chamber, as revealed by EDS.

Counterintuitively, the wear scar obtained from high humidity environment showed undiscernible oxide on the surface based on EDS measurement [Fig. 6-5(a-d)]. The smoother surface from humid environment (75% RH) consisted of gallium and nitrogen, and a very limited amount of oxygen [Fig. 6-5(a-d)]. There is likely an oxide layer, however it is too thin for EDS to measure [127]. Thus, we employed scanning Auger microscopy (SAM) to analyze the worn surface. Fig. 6-6a shows the SEM image of the interested region inside wear scar. Both mapping (Fig. 6-6b) and line scan (Fig. 6-6c) were performed to reveal the surface composition inside and outside the wear scar. First of all, the results confirmed that wear debris consisted of gallium oxide. The gallium signal is slightly less inside the wear scar than the unworn surface. The intensity of nitrogen inside the wear scar is also deficient as compared to the unworn surface. The increased oxygen signal with minimal decrease in Ga signal suggests there is a thin oxide layer on the surface. Furthermore, the lowest intensities for both Ga and N and highest intensity for O inside the wear scar appear in the center of the wear scar. This matches with the location of the maximum normal and shear stress. Considering the difference of probing depth between AES and EDS, it can be understood why oxygen can be barely seen in this case.

For low humidity environment (10% RH), rich signals of oxygen coming from dark patches at the surface, where less nitrogen signal can be seen. This might be the reason for the low and stable friction we have seen in low humidity environment (Fig. 6-2). It is noteworthy that by forming these oxide patches, the wear rate of GaN only increased a little but the friction coefficient (~0.2) was much lower than the unlubricated dry nitrogen environment (~0.8 - 0.9). This might be useful for designs and applications which require both low friction coefficient and ultralow wear rate. However, the formation mechanism of these dark patches is still unclearly and more details of these oxide patches need for further analysis.

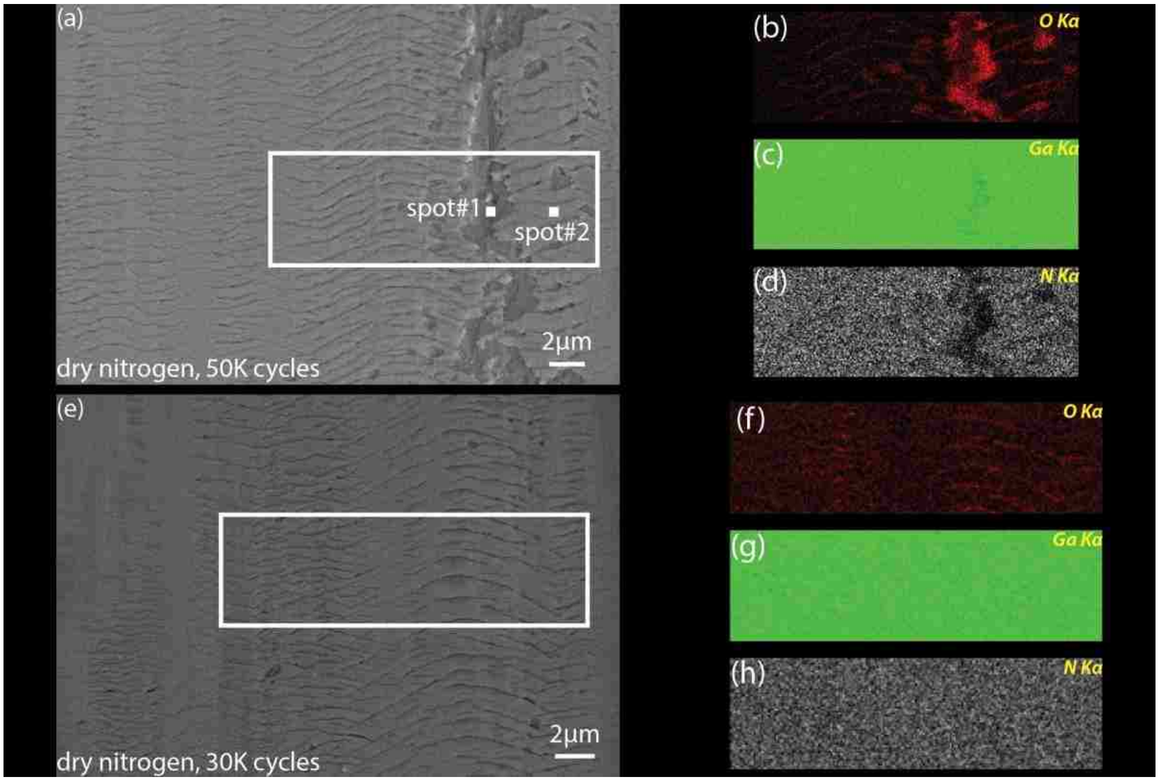

Figure 6-4 EDS mapping on worn surfaces: (a-d) dry nitrogen environment after 50,000 cycles: a) SEM, b) O EDS, c) Ga EDS, and d) N EDS., and (e-h) dry nitrogen environment after 30,000 cycles: SEM and EDS mapping on worn surfaces. (a-d) 75% RH lab air environment after 30,000 cycles: (e-h) 10% RH lab air environment after 30,000 cycles: e) SEM, f) O EDS, g) Ga EDS, and h) N EDS.

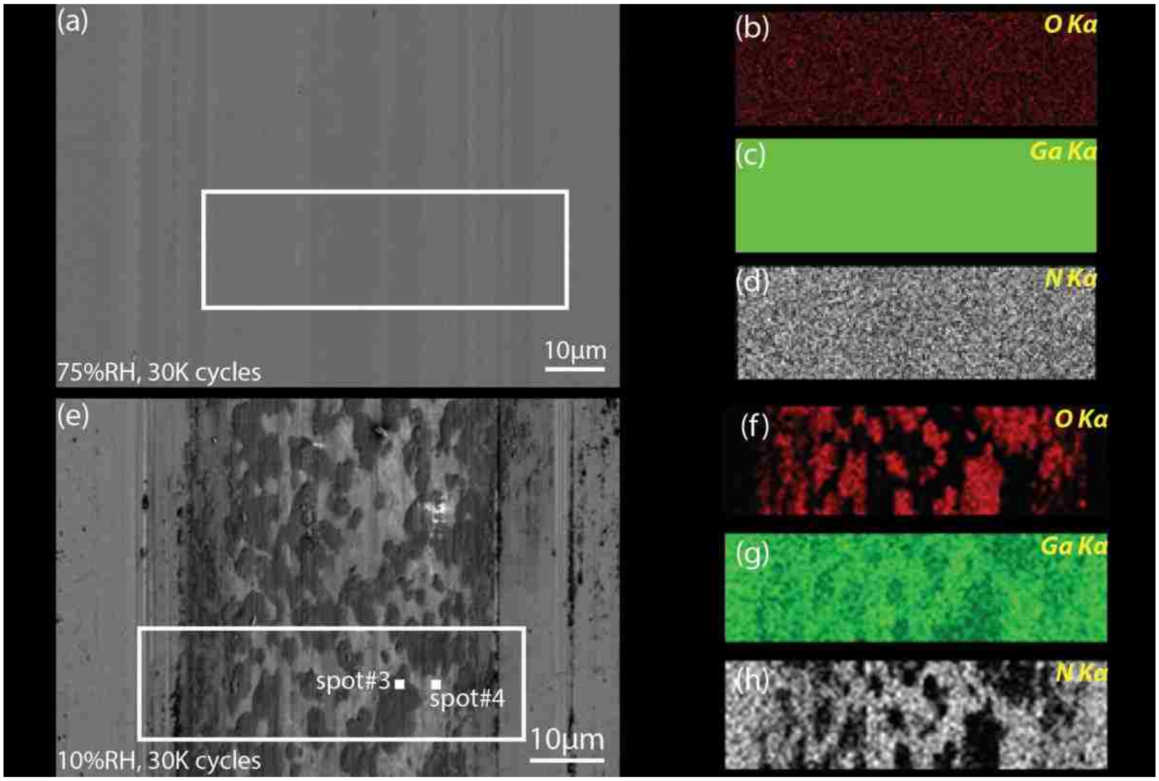

Figure 6-5 SEM and EDS mapping on worn surfaces. (a-d) 75% RH lab air environment after 30,000 cycles: a) SEM, b) O EDS, c) Ga EDS, and d) N EDS. (e-h) 10% RH lab air environment after 30,000 cycles: e) SEM, f) O EDS, g) Ga EDS, and h) N EDS. Note: the EDS measurement is more sensitive to Ga, resulting in Ga detection at every pixel in 5c.

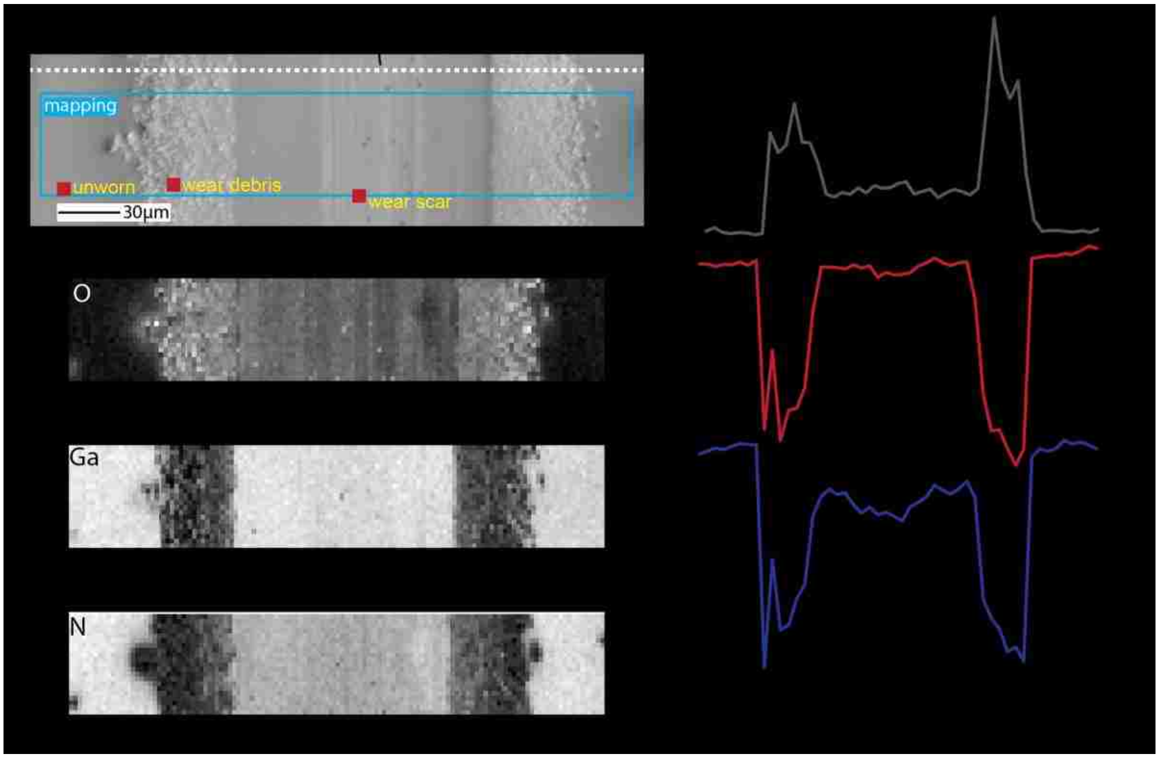

Figure 6-6 Auger electron spectroscopy, (a) SEM image of interested region, (b) Auger mapping and (c) line scan across the wear scar.

The ruby probes associated with each wear scar were also examined by SEM and EDS (Fig. 6-7). It was found that, the ruby probe associated with humid testing environment had a comparable worn surface (~ 60 - 70 µm in diameter) with large amount of wear debris (mainly consisted of gallium-oxygen and gallium-nitrogen) surrounding it. This result suggests a two-body grooving abrasive wear mechanism in humid tribosystem for GaN, which will be discussed later. In contrast, less wear debris of GaN can be seen but more gallium and nitrogen signals were probed at the worn surface of the ruby probes for both dry nitrogen and low humidity testing environments. Although, the surface damage and tribochemistry for both cases were different, material transfer from GaN to ruby probe was clearly evidenced in these two cases. Furthermore, more gallium oxide was found inside the worn area of the ruby probe for low humidity case, and we suspect that this is coming from the oxide patches on the worn surface.

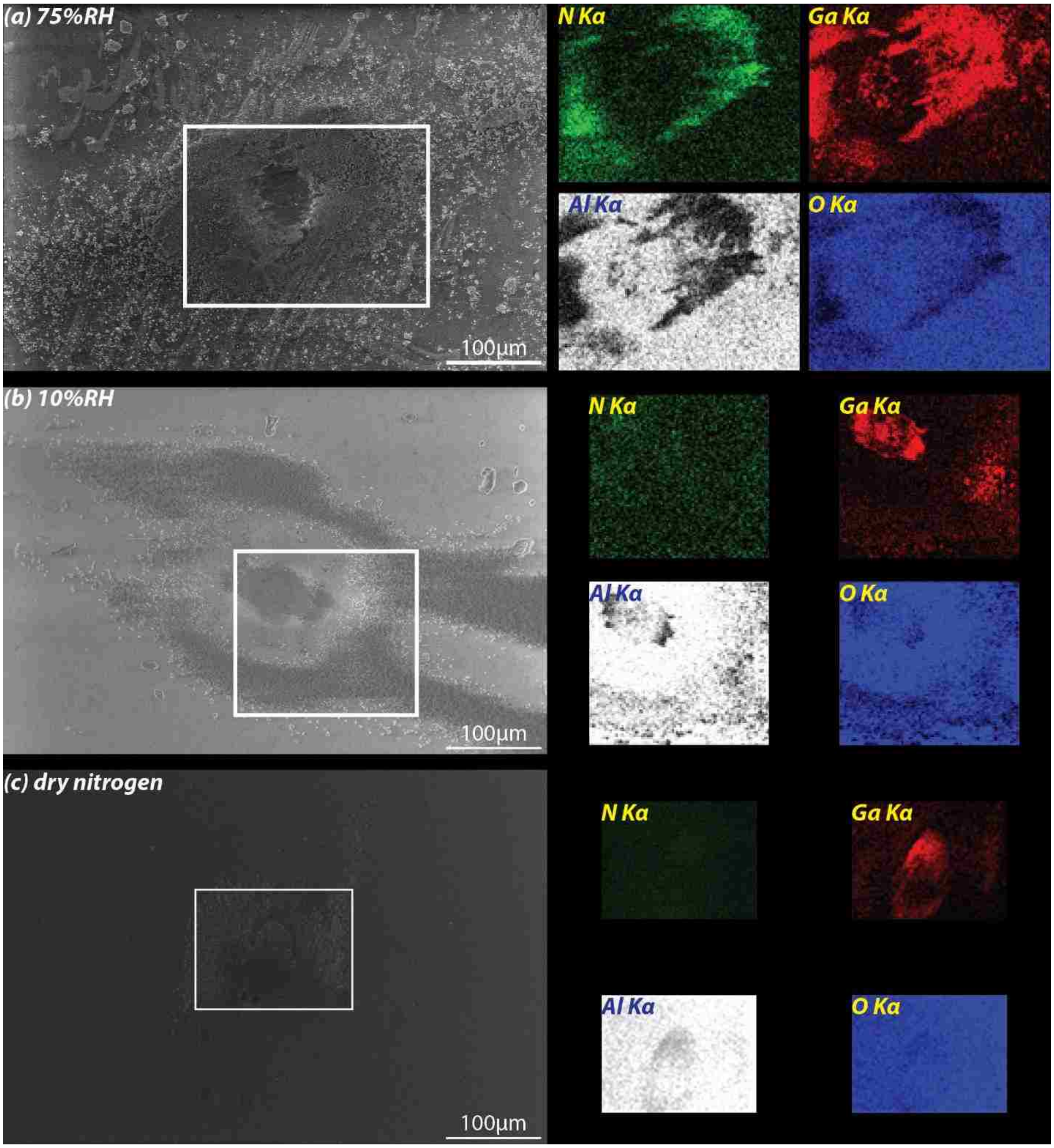

Figure 6-7 EDS on countersamples: (a) 75%RH lab air, (b) 10%RH lab air, and (c) dry N_2.

6.4 DFT Simulation on GaN

In order to verify the hypothesis for explaining the oxidation observed on dry nitrogen environment wear scar, we performed DFT calculation to examine the surface oxidation susceptibility for c-, a- and m-plane of GaN.

Fig. 6-8 shows the DFT-calculated surface energies for GaN with one and two oxygen atoms, respectively. Here, the surface energy is calculated in the following way:

$$\mathrm{E}_{\mathrm{surface}} = \frac{\mathrm{E}_{s} - \mathrm{n} \cdot \mathrm{E}_{b}}{2\mathrm{A}}$$

Where, E_s is the total energy of the entire surface slab, E_b is the bulk energy for each of the atoms represented in the system, n is the number of each of the represented atoms and A is the surface energy of the considered surface slab.

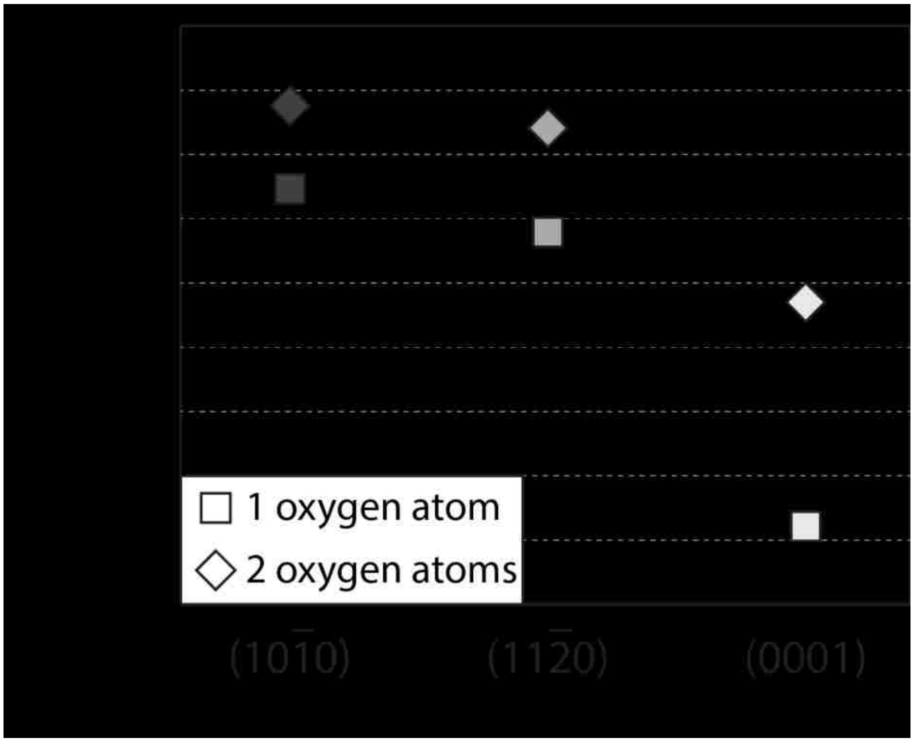

Figure 6-8 DFT simulation: surface energy of m-plane, a-plane and c-plane with one and two oxygen atom coverage.

Fig. 6-8 shows that the c-plane is lowest in energy for 1-oxygen case, as well as the 2-oxygen case, indicating that the c-plane has the most stable energy configuration out of all the planes considered and is less susceptible to oxygen-induced effects compared to the other planes. On the other hand, a-plane is slightly lower in energy compared to the m-plane by about 0.007 J/m^2 for the 1 oxygen case and about 0.004 J/m^2 for the 2-oxygen case. In addition, the trend of the increasing surface energy with the increase of oxygen atoms is anticipated, since larger systems lead to larger total energies, and in turn – surface energies.

This can explain that why the newly formed m-plane and a-plane were heavily oxidized during the sample transfer.

6.5 Discussion of Wear Mechanism

Due to the insufficient height contrast of SEM for humid environment wear scar and the purpose of imaging microscale defects, an AFM scan was performed inside the worn surface to complementally interrogate the topography of the wear scars. As can be seen in Fig. 6-9a, a groove-like profile was presented. Fig. 6-9b shows the profile of a line scan made inside Fig. 6-9a, from which we can see that the peak and valley have the lateral size varying from 2-7 μm and 10-50 nm in depth. Such high aspect ratio matches with what we found in Fig. 6-6a, *i.e.*, the dimension of wear debris accumulated on the ruby probe.

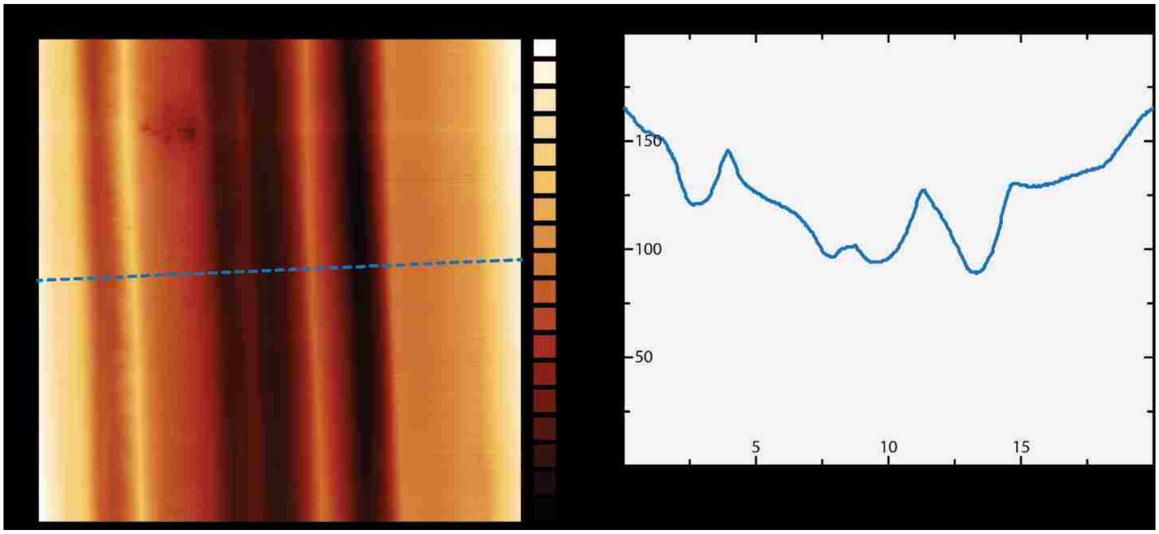

Figure 6-9 AFM of GaN wear scare created with 30,000 sliding cycles in 75 %RH air. (a) height map. (b) height trace.

Combining with the wear debris observed from Fig. 6-7a, we hypothesize that the engendered wear debris, together with the ruby probe, contribute to the wear of GaN coating. Density functional theory (DFT) and molecular dynamics (MD) simulations have been intensively applied to investigate the interactions at GaN-water molecule interface [40], [42], [224], [225]. It has been shown that the water molecules will dissociate into hydroxyl and hydrogen and bond to Ga and N, respectively, reducing the surface energy. With presence of water molecules, more hydroxyl groups will bond to Ga atoms and the surface energy of GaN will be decreased [192], this can facilitate crack propagation and creation of new surfaces. Furthermore, the ubiquity of midgap states in GaN also plays a pivotal role when interacting with water molecules, as shown in Fig. 6-10. The thickness of adsorbed water film will increase with the increasing of relative humidity [227]. This humid atmosphere provides a source of oxygen redox couple (acceptors/donors) and thus enhances the charge transfer with midgap stages of

GaN. This will electrochemically pin the Fermi level of GaN and thus assist the oxidation. As a result, generating defects and removing materials from GaN coating (as shown in Fig. 6-3d) are much faster. It is noteworthy that there is no Al signal in the EDS, thus EDS maps of Al are not included in Fig. 6-4 and 6-5. Furthermore, it was previously observed by scanning Auger microscopy (SAM) that there is no Al in the wear scar [127].

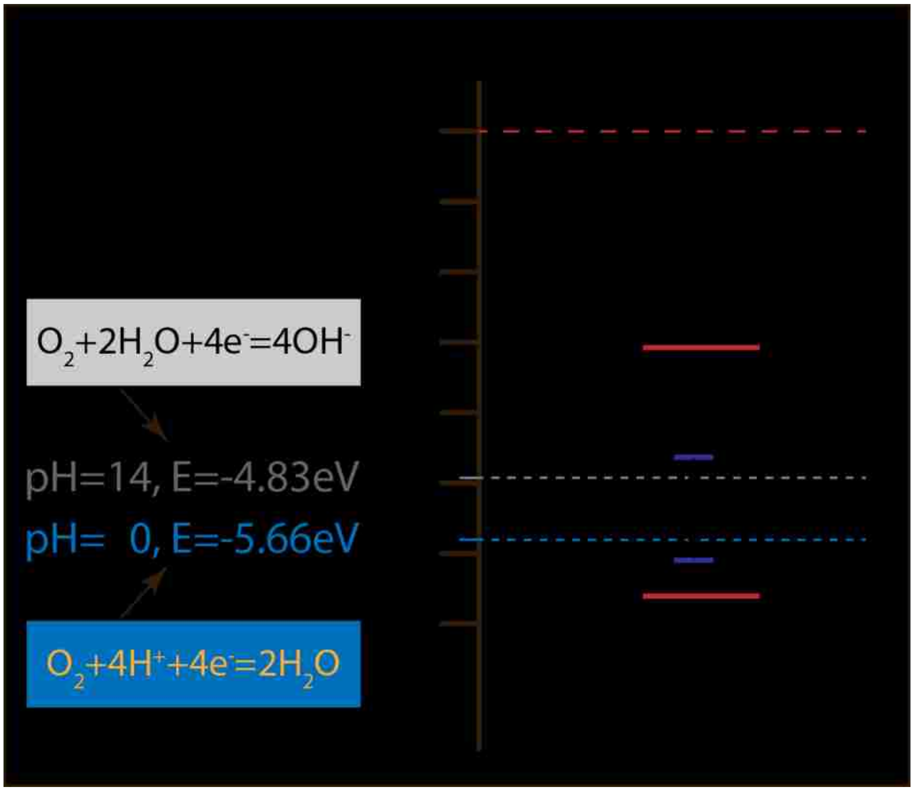

Figure 6-10 Mid-gap states of GaN and energy level of oxygen redox couples [227].

In order to image the defects caused by the sliding contact, a cross-section of the wear scar was prepared by FIB and examined by TEM. Fig. 6-11 presents the dislocations formed underneath the wear scar which was obtained from humid environment. In addition, threading dislocation arising from the lattice mismatch during the epitaxy was also observed [228]. The inset of Fig. 6-11 shows a zoom-in of a dislocation underneath the wear scar. The size (~400 nm) of the GaN within this dislocation was comparable to the size of the wear debris, which indicates a possible evolution of a wear debris formation during the wear test. Induced by the shear stress, the dislocations and cracks will generate and propagate, and both of them directly contribute to the formation of wear debris.

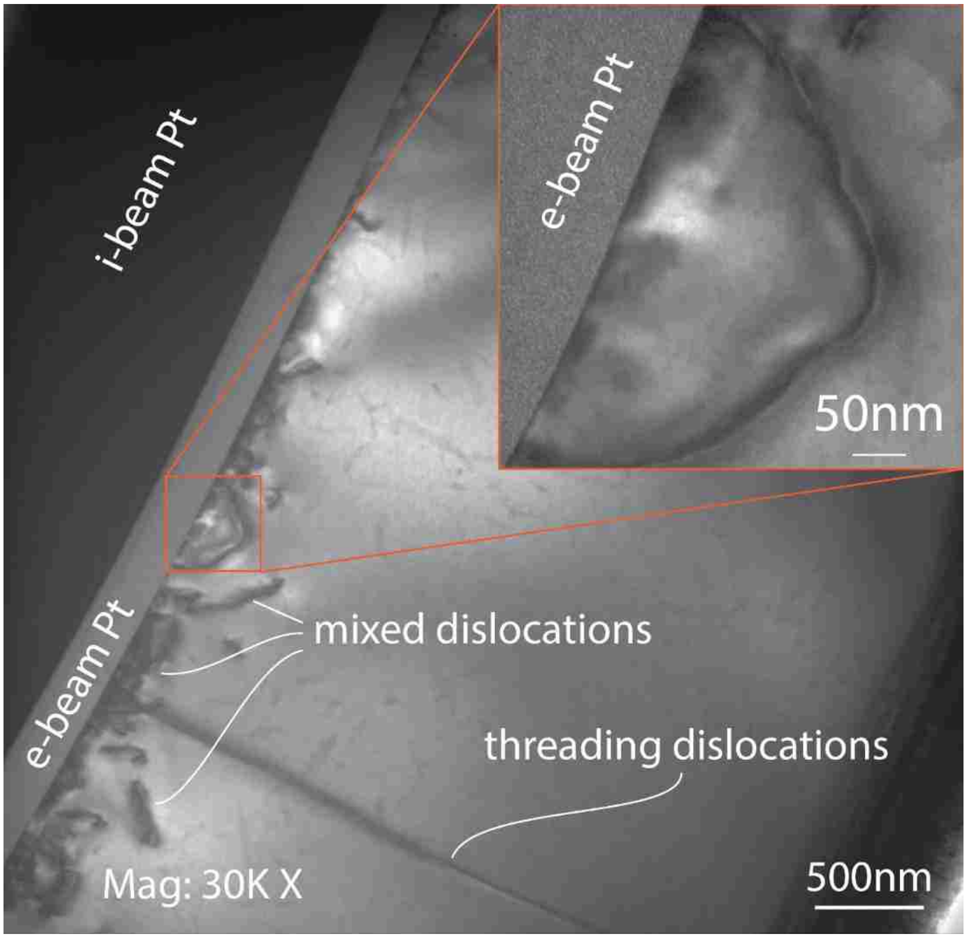

Figure 6-11 TEM image of the cross-section of wear scar (75% RH humid environment).

With presence of a water layer adsorbed onto polar GaN surface, water molecules can split and form Ga-OH bonds at the surface [27], [42]. We hypothesize that applied shear stress at the interface between water and GaN will induce the formation of oxide and hydroxide, which have higher wear rate and can be removed easily as the wear debris (Fig. 6-12). When comparing the high humidity (75% RH) to low humidity (10% RH), we hypothesize there is a competition between tribochemical oxidation (forming a lubricous, but high wear material) and material removal; when oxidation is faster, there is a thicker average oxide layer and material can be removed quicker. If oxidation is slow (as in the 10% RH), the oxide/hydroxide layer remains thin, lubricating the interface and slowing the removal process. Once the wear debris was created, some debris will spread along the sides of and within the wear scar while some will accumulate on the surface of ruby probe and be involved in the following wear process. The multitude of nanometer size wear debris can act as high contact pressure abrasive particles, which in turn facilitate the material removal of the continuously oxidizing sliding surface. In the dry nitrogen environment. tribochemistry with the environment is less likely to occur without the chemisorption of water molecules; the wear process between GaN and ruby countersample in dry nitrogen environment is hypothesized to be dominated by adhesive-type wear. Ridges perpendicular to the wear scar and high friction coefficient support an adhesive wear component. We cannot rule out fatigue-related mechanisms for ejection of larger debris particles from the pot-hole like worn regions.

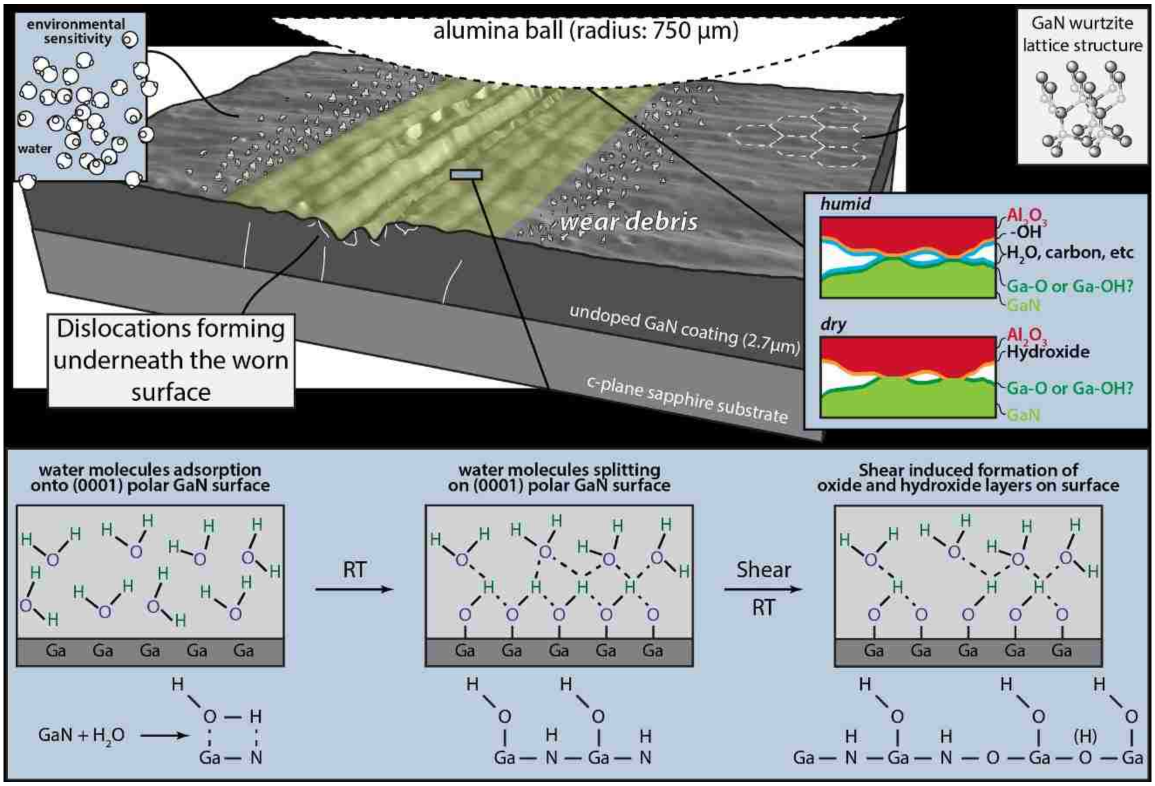

Figure 6-12 Proposed wear mechanism of GaN tested under humid environment.

7 Shear-induced Band Bending in GaN

The prevalence of gallium nitride (GaN) in both scientific research and industrial applications, such as solid state lighting and power electronics, has rapidly expanded in the past few decades due to its remarkable optoelectronic and electronic properties [5]–[8], [159]. As one of the most important semiconductor materials in the optoelectronic area, GaN-based semiconductors have promising potential in photovoltaics, photocatalysis, and photochemistry applications, such as solar cells and photochemical water splitting, due to its profound surface charge properties, i.e., surface band bending and Fermi level tuning [23]–[27]. However, the link between dynamic mechanical contact and band bending has yet to be investigated. To link sliding-induced contact stress to band bending, we used a ruby (α-alumina) probe to perform reciprocating sliding experiments on GaN with different conditions to modify the GaN surface. XPS was employed to measure the band bending and analyze the surface chemistry [27]–[29], [31], [32], [37], [38], [42]–[46], [53], [89], [225], [229]–[232] and STEM with EDS was used to visualize the shear-modified surface and subsurface. The results revealed that, by adjusting the humidity and sliding cycles, the band bending of GaN can be controlled. We term this shear-induced modification to the band states as “tribodoping”.

7.1 Methods and Materials

The unintentional doped (undoped) wurtzite single crystal (0001) 3-μm thick GaN coatings were grown by metal-organic chemical vapor deposition (MOCVD) were tested. Linear reciprocal pin-on-disk sliding tests were performed by custom-built microtribometer mounted inside a glovebox to achieve the humidity control. Three humidity levels were attained in this study, *i.e.*, 5% RH, 30% RH and 60% RH. All the sliding cycle dependence and shear stress dependence studies were conducted under 60% RH environment. All sliding tests were along <1$\bar{2}$10> crystallographic direction. Single crystal α-alumina (ruby) balls with radius of 0.75mm (Swiss Jewel Company, Grade 25) were selected as the countersamples to reciprocate against GaN coating. The sliding speed was kept as 5mm/s for all the tests. The applied normal load was kept at 600mN constantly, corresponds to a maximum Hertzian contact pressure of ~2 GPa, for all the environment dependence and sliding cycle dependence studies. The normal load then was switched to 100mN (~1 GPa maximum Hertzian contact pressure) for shear stress dependence investigation.

X-ray photoemission spectroscopy (XPS), scanning Auger microscopy (SAM), high resolution transmission electron microscopy (HR-TEM) as well as energy dispersive X-ray spectroscopy (EDS) were employed to analyze the surface before and after shear modification. Low voltage SEM (LVSEM, ZEISS 1550) was employed to visualize the inhomogeneous band bending from the shear modified surface (60% RH lab air, 30,000 sliding cycles). In-lens detector was used to capture "true" secondary electron (SE1) signals only and the working distance was set to be 5mm. Low accelerating voltage (0.5 kV) was used first to obtain a clear secondary electron (SE) contrast. Then the accelerating voltage was then increased gradually to 5 kV to obtain a stable contrast reversal.

7.2 *Surface Characterization by XPS*

7.2.1 Environment Dependence

As shown in Fig. 7-1a and 7-1b, sliding on the unintentionally-doped (background doping n-type of 5 × 10^{16} cm^{-3}) GaN surface produced a significant shift to lower binding energy (BE) of the Ga 3d XPS peak. This was initially interpreted as a chemical shift, which would mean reduction of Ga in GaN towards metallic gallium [28], [233]. However, careful calculation of the Auger parameter (see Auger Parameter Calculation; Table 7-1) and analysis of spectra obtained after deposition of Au (Fig. 7-6) indicates that this BE shift is not chemical. Instead, we hypothesize that this BE shift is the result of physical changes to the GaN semiconductor surface, which results in modifying the degree of band bending. The as-grown GaN surface has a narrow peak centered at 20.2 eV, which is used as a reference peak, while a broader Ga 3d peak from the shear-modified surface (*i.e.* the region where the ruby sphere was slid against the surface) occurs at a lower BE; this is evidence that the band structure of the film has been modified. The width of this peak suggests that the band states of the shear-modified region of GaN are inhomogeneous in space. Furthermore, the Ga 2p, and N1s followed similar shifts in binding energy. However, the N1s is less reliable as there a Ga Auger line close to the GaN N1s binding energy [234].

The degree of band structure modification (as measured by XPS) is strongly correlated to the relative humidity of the sliding environment (Fig. 7-1a). The band structure is most modified when sliding in a 60% RH environment, followed very closely by a 30% RH environment. Contrary to that for GaN films modified in high humidity, sliding in a 5% RH environment caused surface oxidation, as shown in Fig. 7-1a and 7-1c.

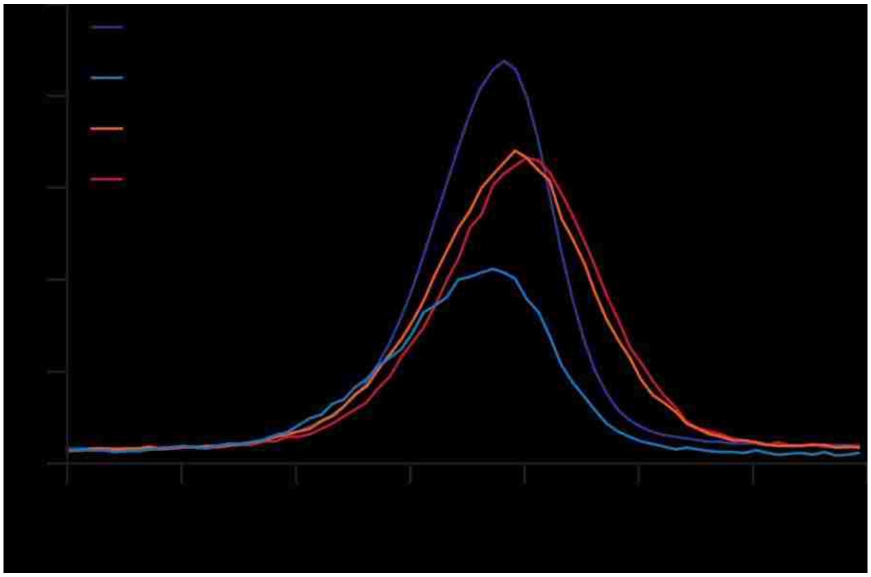

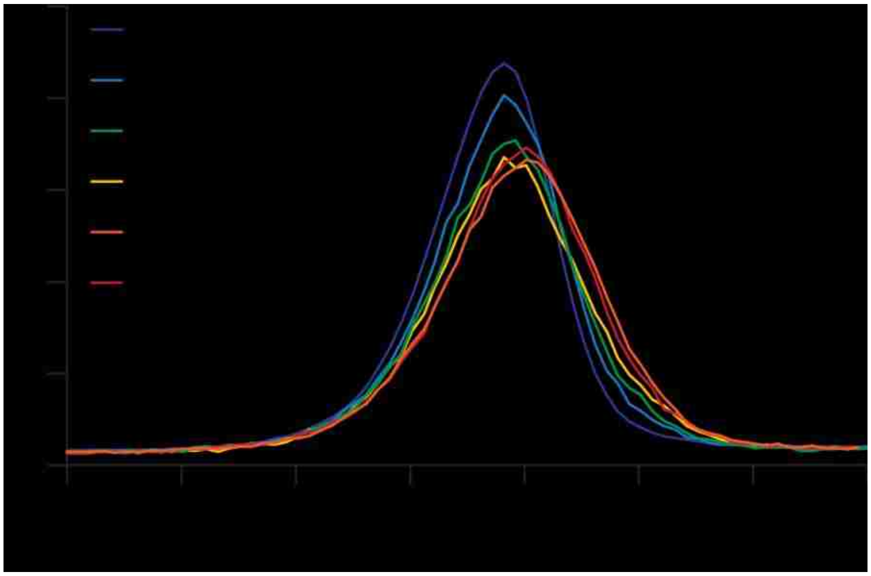

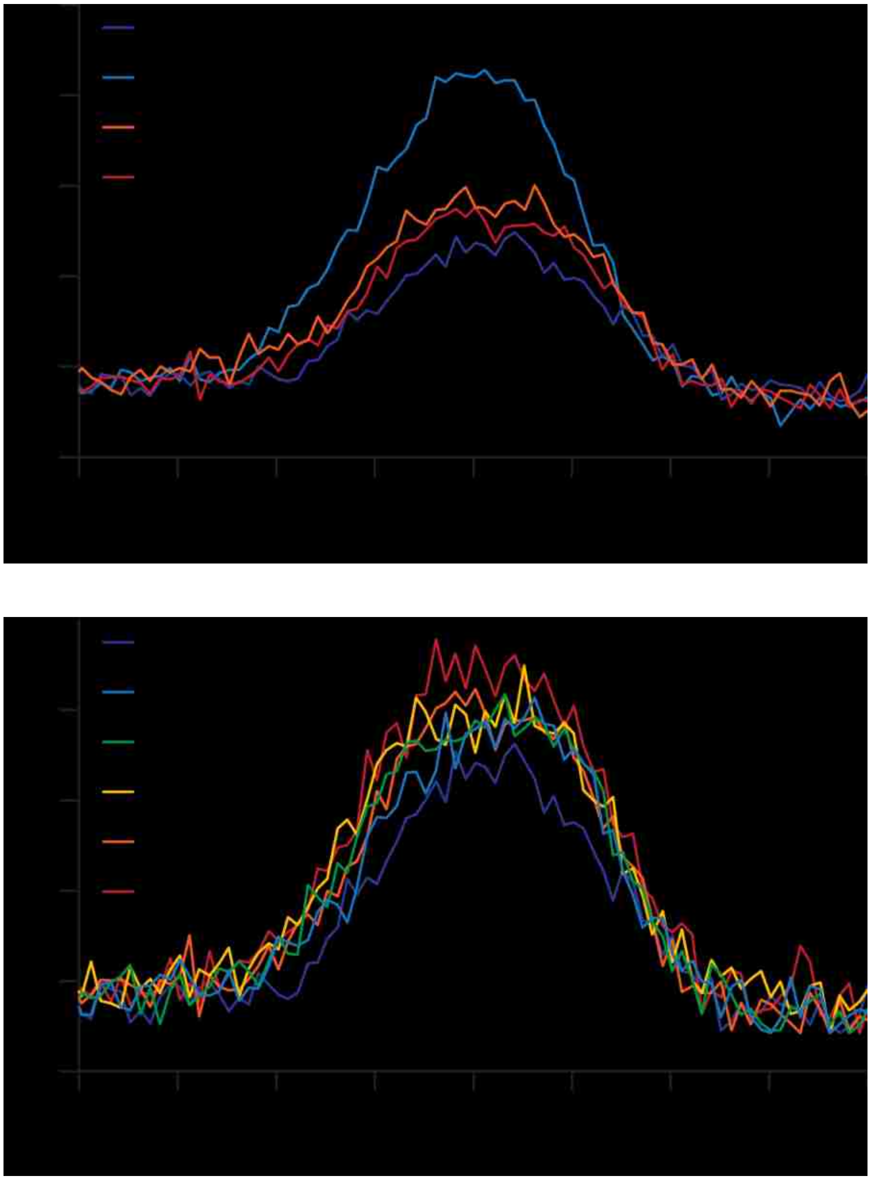

Figure 7-1 XPS of Shear-Modified GaN surfaces. (a) XPS Ga 3d spectra from different testing environments; (b) XPS Ga 3d spectra from different sliding; (c) XPS O 1s spectra from different testing environments; (b) XPS O 1s spectra from different sliding.

7.2.1.1 Clarification of Band Bending

The core level binding energy (BE) shift in XPS can be influenced by several factors, including chemical shift associated with bonding state, band bending, and charging effect. To eliminate the surface charging created by photoemission, low energy electrons (0.1 eV) generated by the floodgun with Ar clusters were exposed to the surface for surface neutralization.

Auger parameter is a useful tool to analyze the chemical state without being influenced by surface charging. Calculation of Auger parameter is shown as followed [235]:

$$\alpha = E_K(A) - E_K(PE)$$

where $E_K(A)$ represents the kinetic energy of Auger electron while the $E_K(PE)$ is the kinetic energy of photoelectron from core level. Table 1 compares the Ga 3d Auger parameters of shear modified surface (60% RH, 30,000 sliding cycles) and as-grown surface, as taken from the Auger line, measured by XPS (Fig. 7-2). It clearly shows that the Auger parameters for these two surfaces are identical, which indicates that other than the change of chemical state, band bending is believed to be responsible for all these peak shifts.

Table 7-1 Auger parameters for shear-modified (60 %RH, 30,000 sliding cycles) and as-grown surfaces

	Kinetic energy (Ga 3d) $E_{K.E.}$ (eV)	Auger energy(LMM) E_{Auger} (eV)	Auger parameter E_{Auger} - $E_{K.E.}$ (eV)
Shear modified surface	1466.7	1064.07	-402.63
As-dep surface	1466.45	1063.8	-402.65

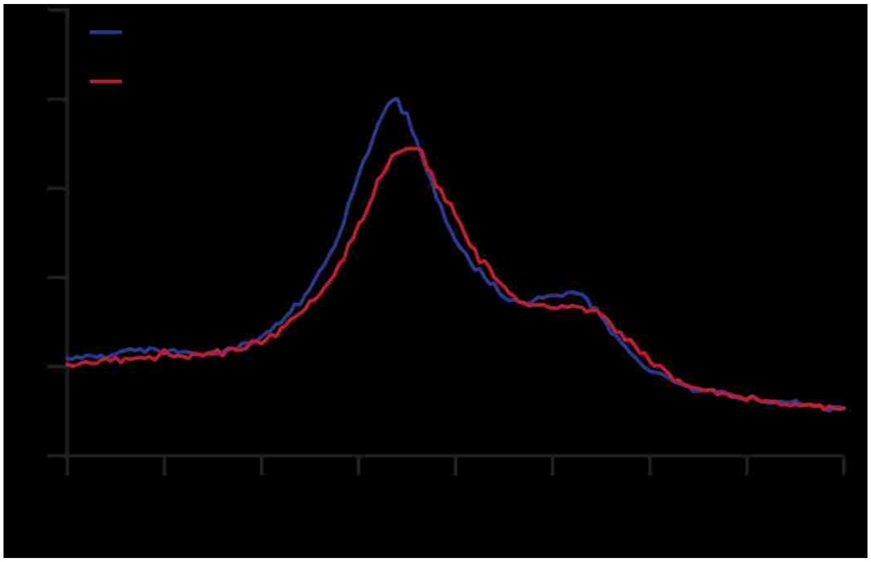

Figure 7-2 Ga LMM Auger lines for as-grown and shear-modified (60% RH, 30,000 sliding cycles) surfaces.

7.2.2 Sliding Cycle Dependence

In addition to humidity, the Ga 3d peak position also exhibited a strong dependence on the number of sliding cycles (Fig. 7-1b). With increasing sliding cycles, the Ga 3d peak shifted further down to lower BE for up to ~30,000 sliding cycles where the maximum peak shift occurred. It is noteworthy that, under same testing environment (60 %RH lab air), shear-modified surfaces with different sliding cycles exhibited comparable oxidation at the surface with only 50,000 cycle shear-modified surface having slightly higher O 1s signal (Fig. 7-1d). This slightly heavier oxidation after 50,000 sliding cycles leads to a “backward” shift of the Ga 3d peak to higher BE, as shown in Fig. 7-1b.

Several factors are proposed for explaining the peak shifts and broadening in the XPS spectra. First, sliding with a spherical probe on a flat surface results in spatially variant contact stresses observed by the film. Furthermore, wear is somewhat stochastic in nature and the surface that is modified by sliding will be inhomogeneous. This results in spatial variance of the band bending, which indicates that the width of the broad shifted peak is the sum of many smaller sub-peaks with slightly different binding energies, as shown in Fig. 7-1a and 7-1b. Secondly, the probe depth (surface sensitivity) of XPS is less than 8 nm, which is much smaller than the depth of the space charge layer, resulting in different BEs measured for Ga photoelectrons originating at different depths. Finally, the formation of a thin oxide at the surface can modify band bending [236]. This can also modify the chemical shift in XPS and even result in surface dipoles.

7.2.3 Normal Load Dependence

Two different normal loads (100mN and 600mN) were selected to examine the load dependence on surface band bending. Fig. 7-3a presents Ga 3d XPS spectra that probe surface band bending that results from different normal loads and different sliding cycles. Band bending still follows the sliding cycle dependence for both cases, *i.e.*, with longer sliding, the Ga 3d peak shifts further to lower BE. However, the surfaces from the 100 mN normal load have significantly fewer alterations to the surface states, as evidenced by smaller intensity at lower BEs, while the surfaces from the 600 mN load with corresponding sliding cycles exhibited much larger peak shifts. This result is consistent with the aforementioned hypothesis that the vacancies introduced by the shear stress give rise to band bending. Fig. 7-3b shows another interesting finding about surface oxidation. Counterintuitively, surfaces subjected to the higher load (600 mN) had less oxidation on the surface than those for the lower load (100 mN). We hypothesize that the frictional interaction will oxidize GaN in the presence of oxygen, however the competition between oxide forming and oxide wearing rates results in thicker oxides for the lower applied normal loads. This can be extended to the counterintuitive observation that lower humidity environments produced more oxide, because, the wear rate of GaN is significantly lower with decreasing relative humidity, resulting in less wear of the oxide.

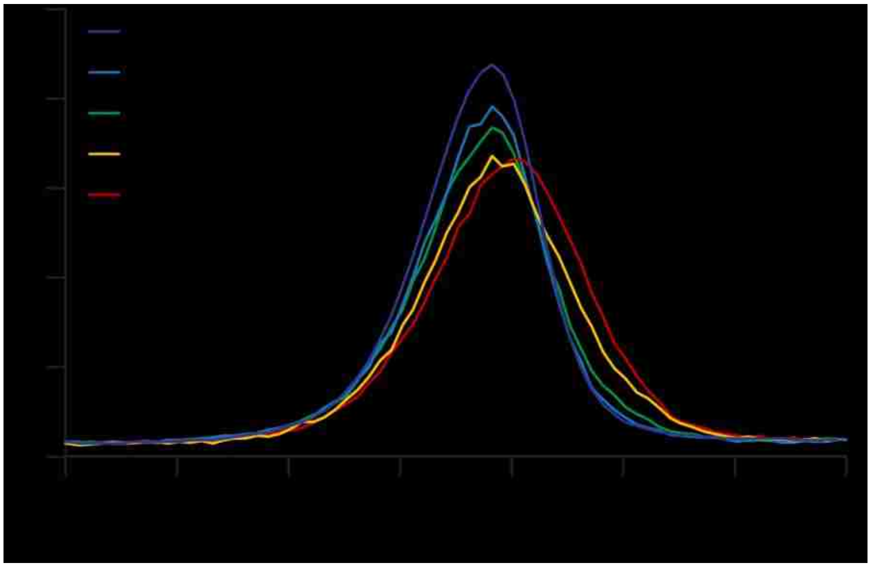

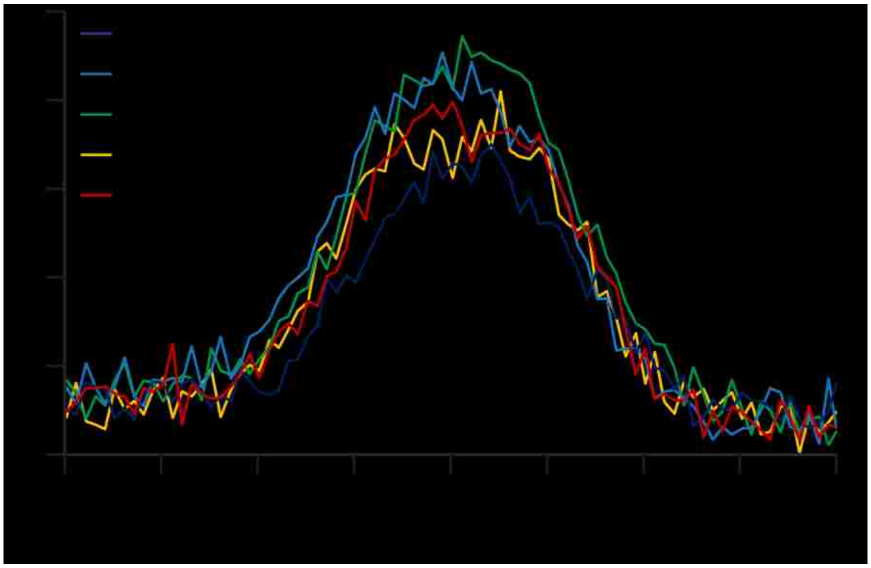

Figure 7-3 XPS Revealing Normal Load and Sliding Cycle Dependence on Band Bending (a) XPS spectra of Ga 3d with 100mN and 600mN normal loads; (b) XPS spectra of O 1s with 100mN and 600mN normal loads.

7.3 Visualization of Lattice Structure and Defects under Worn Surfaces

GaN has a remarkably low wear rate [126], which allows us to slide for many cycles with little damage to the surface. The degree to which the surface is damaged will be incredibly important if devices are ever made using this tribodoping method. We employed TEM/EDS to visualize the crystalline structure, chemical states, and defects formed underneath the shear-modified surface. As shown in Fig. 7-3a, the shear-modified surface was mapped by EDS and a rich oxygen signal was clearly observed. As marked by the dashed lines, the thickness of this layer was less than 2 nm and also had a deficient nitrogen signal and partially deficient signal of gallium. As reported by Watkins et al. [28], only about 0.9 monolayers of oxygen was found on the GaN surface at room temperature; this is due to the similar bond lengths for Ga-N and Ga-O, which makes the GaN surface difficult to oxidize further. In our study, a larger gallium-oxygen layer was formed, likely by shear-assisted oxidation; it is unclear if this is gallium oxide or gallium oxynitride. The backward shift of the Ga peaks for the 50,000-cycle (Figs. 7-1d) can be attributed to increased oxidation. Longer sliding gave rise to a thicker gallium-oxygen layer. This is consistent with what we found in Fig. 7-1b and Fig. 7-1d, *i.e.*, the XPS peak shift was not caused by band bending nor chemical shift (oxidation) alone, but rather a competition between chemical and band bending shift.

Fig. 7-4b shows the lattice underneath the shear-modified surface by STEM high-angle annular dark field (HAADF) imaging. The GaN lattice maintained its wurtzite epitaxy after 30,000 sliding cycles under ~2 GPa maximum Hertzian contact pressure. From the relatively lower magnification TEM dark field imaging (Fig. 7-4c), it is also clear that dislocations were generated due to the shear stress. It has been experimentally and computationally demonstrated that vacancies can often be found at dislocation cores in GaN, and behave as an acceptor (Ga vacancy) or donor (N vacancy) [237]–[241]. The lower binding energy shift observed in Fig. 7-1 indicates an upward band bending [53], [242]–[244]. The upward band bending indicates the presence of Ga vacancies (V_{Ga}) in the GaN surface due to the shearing process. This hypothesis is also consistent with what we found from normal load dependence, *i.e.*, higher load can generate more defects during the test and leads to larger degree of band bending, and vice versa.

In stark contrast to the traditional point of view that defects have a deleterious effect by hindering transportation of charge carriers, Zhang et al. [245] revealed a benign role of defects in semiconductor devices, *i.e.*, defects in QDs can guide the charge percolation process. In our discovery, the presence of defects contributes to further surface band bending, which can potentially be implemented favorably into photocatalysis and chemical sensing devices.

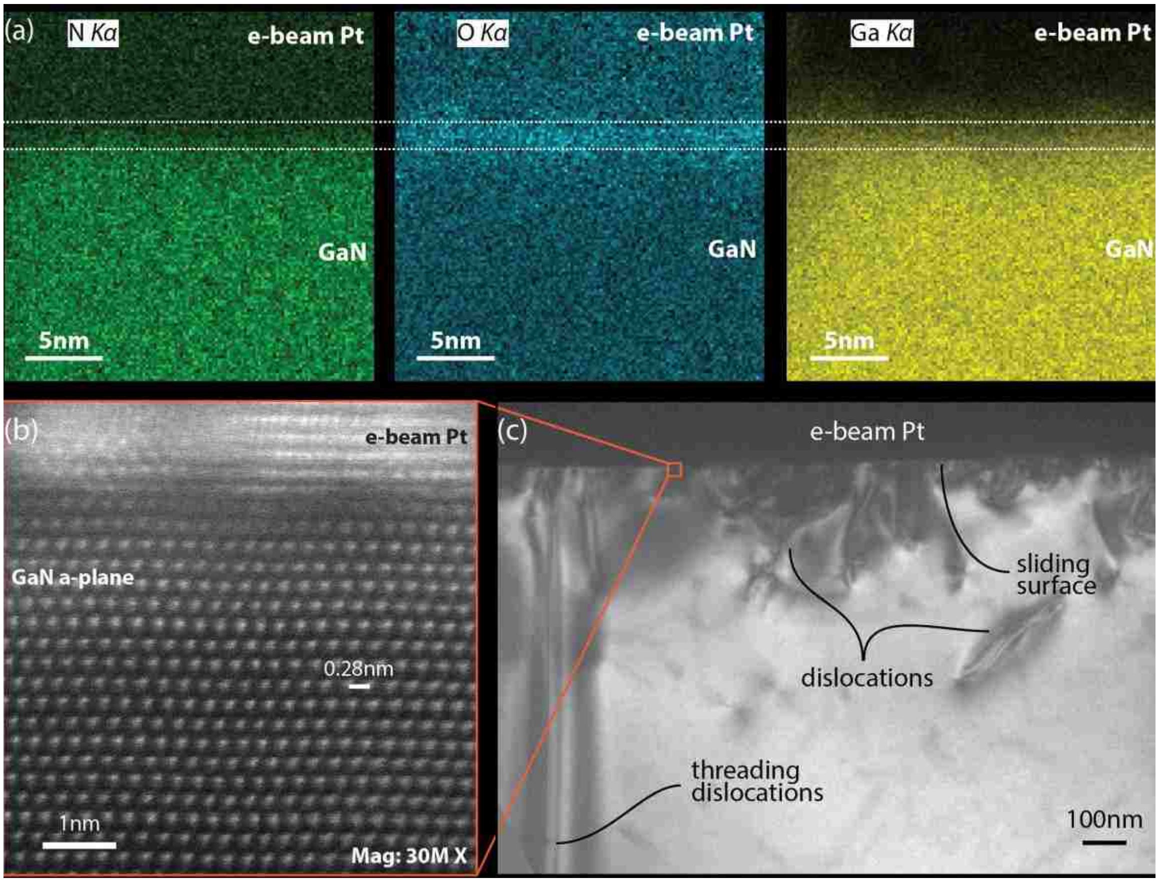

Figure 7-4 TEM of Shear-Modified Surface (a) EDS showing nitrogen, oxygen and gallium; dashed lines represent approximate location of GaN surface (b) HR-TEM image of GaN lattice after shear stress modification. (c) TEM image of sliding surface after shear stress modification.

7.4 Visualization of Surface Band Bending by LVSEM

The inhomogeneity of the surface states was visualized and confirmed with low voltage scanning electron microscopy (LVSEM) in Fig. 7-5. Upward band bending will build up an electrical field pointing from the bulk to the surface. When applying a low accelerating voltage, this electrical field will suppress the emission of secondary electrons from the top surface and give rise to a secondary electron (SE) contrast (*i.e.*, dark area in micrograph, see Fig. 7-5a). However, when the accelerating voltage is above a critical value, 2 kV, the SE contrast will reverse, due to the existing oxide [246], [247]. In Fig. 7-5, the accelerating voltage of the primary electron beam is increased from Figs. 7-5a to 7-5f and the contrast of the shear-modified region flipped as the accelerating voltage transitions from 1 to 3 kV.

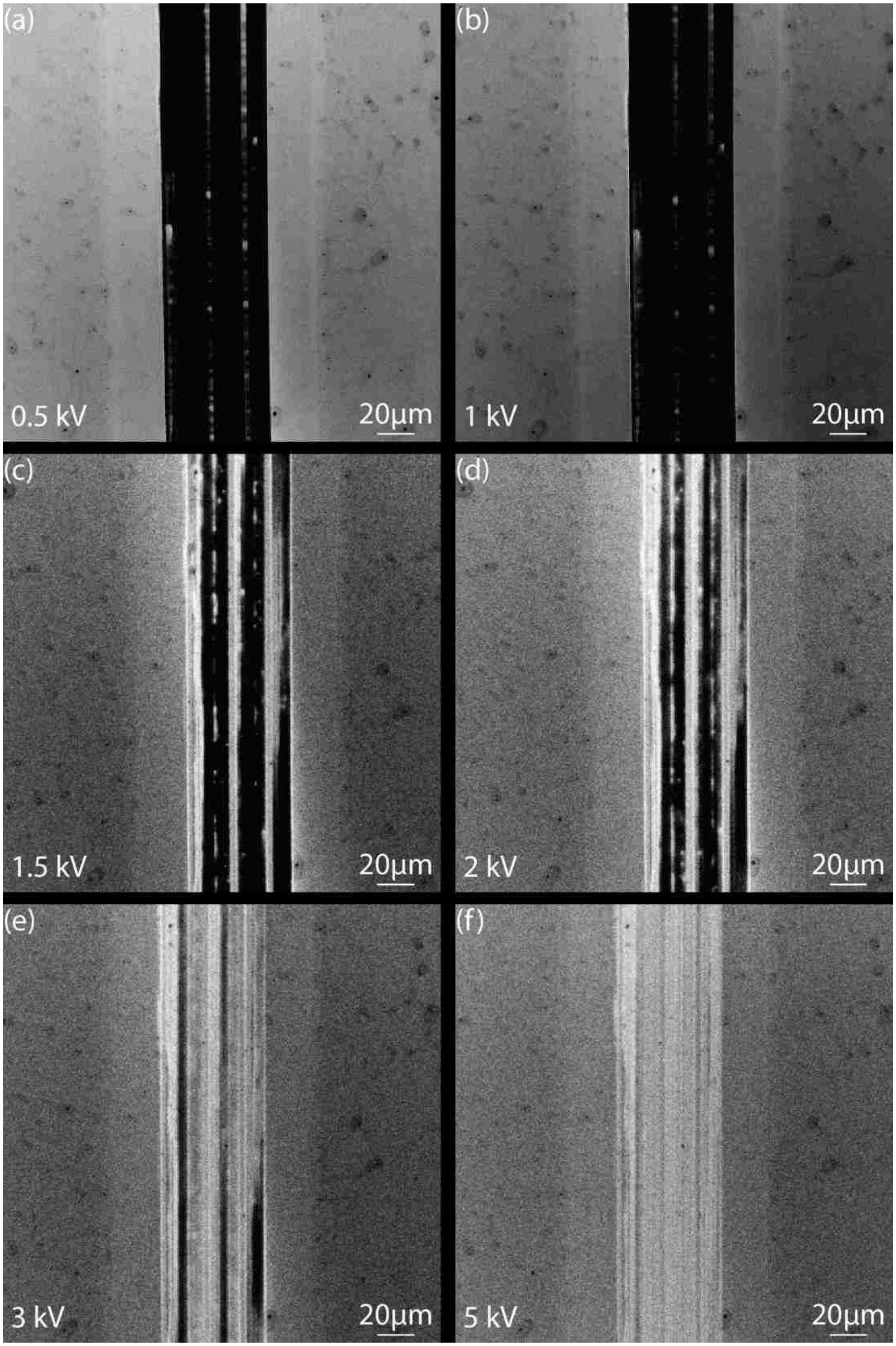

Figure 7-5 Secondary electron contrast with different accelerating voltage (a) 0.5 kV; (b) 1 kV; (c) 1.5 kV; (d) 2 kV; (e) 3 kV and (f) 5 kV.

7.5 Demonstration of Applicability of Tribodoping-induced Band Bending

By applying noble metals (*e.g.*, Au) on semiconductor materials to form heterogeneous photocatalysts, the photoexcited surface plasmon resonance (SPR) can be achieved. This results in a significant improvement of the reaction rate in various photocatalysis process, when compared to those pure semiconductor counterparts [248]–[258]. It has been reported that the photoexcited electron-hole pairs can be effectively separated by bent-band region (space charge region) at the metal/semiconductor heterojunction; this is used to improve the efficiency of sunlight harvesting and conversion, water splitting, *etc*. [47], [259]. To test the potential application of the shear-induced band bending (as reported above) in photocatalysis, a < 2 nm gold film was coated on the surface of both as-grown GaN and the shear-modified GaN. XPS revealed that the Au 4f doublet peaks from the shear-modified surface shift slightly (~0.11 eV) from the as-grown surface (Fig. 7-6a). A 0.11 eV peak shift is small, but significant, when considering that Au is one of the most conductive metals and has been widely used in metal/GaN contact for Fermi level alignment [260]. Firstly, this shifting indicates that, even though the degree of band bending is reduced by such thin layer of Au, the electric field origin from the shear-modified GaN surface can still affect the Au layer. This effect can lead to suppression of electron-hole pair recombination in Au films/nanoparticles, results in improvement of the efficiency of Au-nanostructure-based photocatalysis. Secondly, this result also demonstrates that the Au supported on shear-modified GaN provides a way to tune the electronic property of the Au, which potentially leads to altered binding strength to the surface adsorbates and improved catalytic properties of the Au [261]. Finally, XPS spectra of Ga 3d shown in Fig. 7-6b exhibits a similar shift amount when compared to the Au 4f. The Ga 3d of the Au-coated shear-modified GaN surface shows not only a smaller shift (~ 0.11 eV), but also shows a narrower peak when compared to the uncoated, shear-modified GaN surface (~ 0.5 eV; Fig. 7-1a). This is in-line with our hypothesis that the broad shifted peaks of Ga 3d consist of multiple sub-peaks instead of chemical shift; a thin Au layer helps align the Fermi-level, reducing the band bending variance and narrowing the peak.

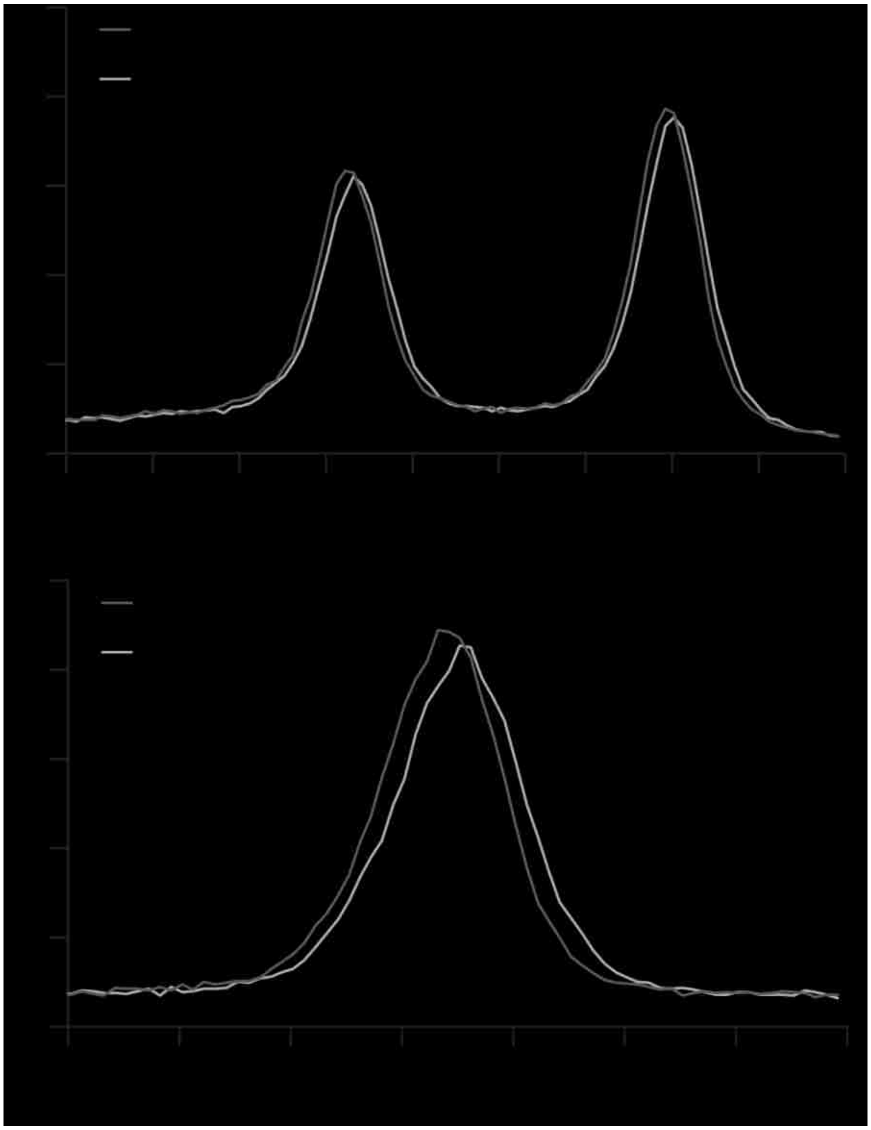

Figure 7-6 XPS of GaN with Thin Au Film on Top of As-deposited and Shear-modified Surface (a) Au 4f XPS spectra; (b) Ga 3d XPS spectra. Au film <2nm to align Fermi level

In this study, we discovered a new phenomenon, “tribodoping”, which has been reported for the first time, *i.e.*, by means of tribological sliding, the electronic property of GaN can be modified. Explicitly, the dynamic mechanical contact can lead to defect generation underneath the surface, which can alter the Fermi level of the surface. This results in the Fermi level re-alignment (surface band bending), and visualized as XPS peak shift, as illustrated in Fig. 7-7.

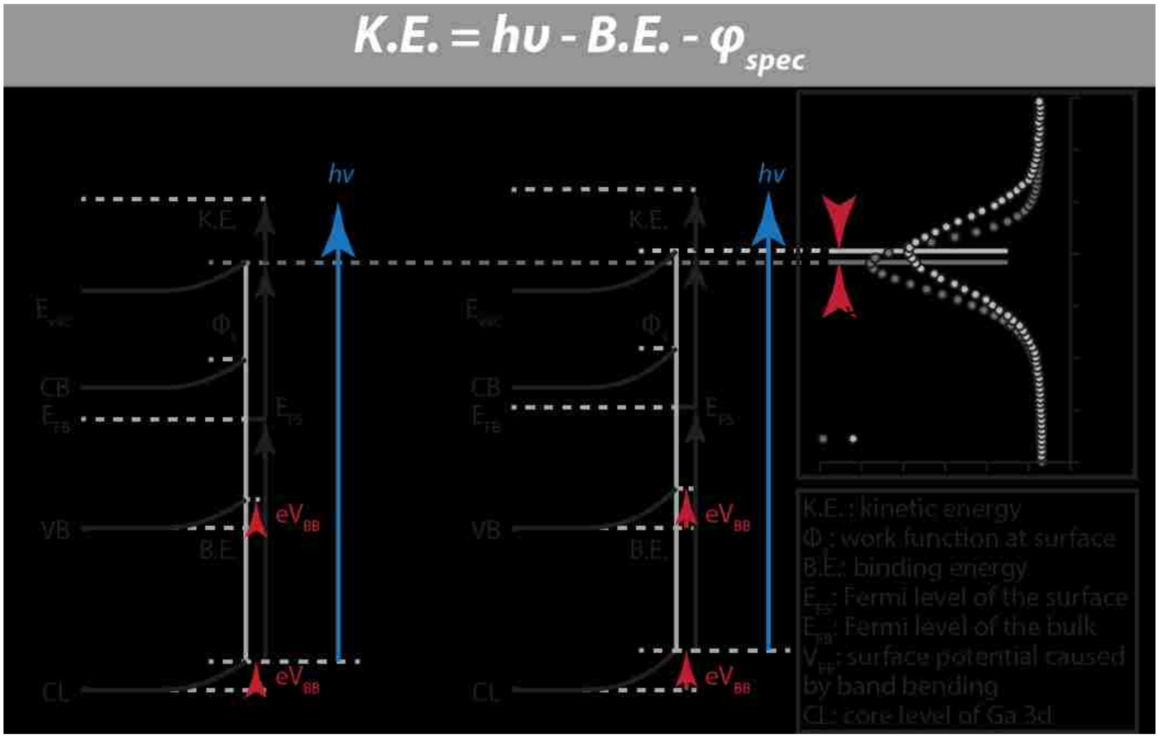

Figure 7-7 Schematic of band diagram for comparison between as deposited surface and worn surface.

8 Conclusions and Future Works

Inorganic crystalline solids including nitrides and other ceramic materials have historically been ideal candidates for solid-state lubricants because of their high melting temperatures, hardness and wear resistance. As technologies for use and production of GaN and similar materials emerge for optoelectronic devices, the availability and cost of these materials will benefit their use in tribological applications. In this study, we mainly focus on the tribological (wear and friction) properties of GaN and allied III-Nitride semiconductor materials. We discovered that the GaN had the ultralow wear nature that approached to that of diamond when tested under certain environment. The wear rate of GaN is affected by several factors, including crystallographic direction, humidity, composition, defect density, etc. Furthermore, the tribological sliding will modify the surface charge property of GaN, which opens up new direction on the important possibility of preparing and integrating GaN semiconductors with modified surface - under the right compositions, environments, and crystal orientation – for new electro-chemical, electro-mechanical and optoelectro-mechanical applications. Proposed mechanisms for such orientation effect, humidity effect and shear-induced band bending (“tribodoping”) are summarized as below:

(1) We explored the full map of crystallographic orientation dependence of GaN’s wear behavior by means of both experimental and computational methods. This demonstration of the crystallographic orientation wear dependence of GaN provides the further understanding beyond our initial discovery on the low wear rate of this material. From the experimental results, we can observe that wear performance of GaN exhibits a strong directionality with a periodicity of 60°, with local lowest always appeared in <$1\bar{1}00$> family direction and local highest wear

rate in $<1\bar{2}10>$ family direction. Molecular static simulation helps us to explain the physics behind crystallographic dependence. Higher energy barrier density and height along $<1\bar{1}00>$ family direction than in $<1\bar{2}10>$ require more work to move around the wear cluster, which in turn explains the reason why $<1\bar{2}10>$ family direction has higher wear rate than $<1\bar{1}00>$ family direction. Consequently, the current finding provides further insight into crystallographic orientation dependence of wear behavior of GaN and benefits the GaN society during device designs and applications.

(2) Wear rate of GaN expanded over two orders of magnitude when tested under different humidity levels. tribochemistry of GaN under different testing environments were analyzed and the wear mechanism of GaN has been discussed. Wear rate of GaN expanded over two orders of magnitude when tested under different humidity levels. Wear scar obtained under humid environment has the highest wear rate and moderate friction coefficient. Dry nitrogen environment has the lowest wear rate and highest friction coefficient. The low humidity environment has the lowest and most stable friction during the stable stage and its wear rate is only two time higher than the dry nitrogen environment. SEM/EDS revealed that GaN responded differently to different environments and these were attributed to the difference in GaN wear behavior under different testing environments. More wear debris was found on the ruby probe for the humid testing environment while some material transfers were imaged for low humidity and dry nitrogen environments. This finding together with the AFM scan support the grooving

abrasion wear mode in the humid environment and adhesive wear mode in dry nitrogen environment.

(3) Changes in composition of the coating by changing cations is a promising way to alter wear performance as demonstrated by the GaN, InN and InGaN system comparisons. It is noteworthy that, while the substitution of 17% Ga with In appears to be a large increase in wear rate, it is still fifty times lower than the wear rate of pure InN; this points to the opportunity to optimize coatings by balancing optoelectronic properties with wear properties using InGaN alloys. Furthermore, if the correlation between hardness and wear rate with changing group 13 cation persists, there is a clear benefit to pursue studies in wear of AlN or even attempts to stabilize wurtzite BN alloy coatings. This points to opportunities to design even more wear resistant materials by alloying with other group 13 cations (Al and even B), with the possibility of even surpassing diamond.

(4) For the shear-induced band bending phenomenon, we have discovered and shown that sliding on the surface of GaN can modify the band states, resulting in altered electrical properties (*i.e.* upward band bending of more than 0.5 eV). Many factors can control the degree to which band states are modified, including humidity, sliding cycles, and normal load. The shearing process modifies band bending at the GaN surface locally, which results in a large contrast of the free carriers between the sheared-surface and as-grown surface. This tribodoping effect has potential for application in a number of semiconductor devices, including those for surface-sensitive sensors (including gas sensing), photocatalysis (including water splitting), multifunctional device materials (touchscreen electronics), and potentially sheared-

modified circuits on GaN, however its utility and scalability in industrial device fabrication still must be confirmed. This newly reported phenomenon leaves many open questions for the interdisciplinary science and engineering community, including: 1) What is the mechanism of defects to alter band states? 2) What are the key material parameters defining the response of band bending to shear-processes? 3) How can this discovery be used to develop new devices? 4) How to obtain larger degree of band bending to further separate electron-hole pair for photochemistry applications; and 5) can this tribodoping method be applied to other semiconductor materials? Addressing these questions will challenge and engage an interdisciplinary chemistry, physics, materials science, tribology and semiconductor device communities.

The future works of GaN wear mechanism and tribodoping will focuses on the following aspects:

(1) Tribological test under high temperature. GaN is a thermal stable material with melting point of ~2400 °C and decomposition around ~1300 °C. Furthermore, water molecules will desorb at ~200 °C. Testing GaN under high temperature will not only minimize the moisture effect, but also can look into the wear behavior under such harsh environment. What will happen when the bond strength being lowered down is of our interests.

(2) Composition mapping. For now, only InGaN with 17% In has been studied. All other ternary composites, such as AlGaN, AlInN, have not been studied yet. Their tribochemistry as well as wear performance are critical when optimizing the III-Nitride-based device design and fabrication.

(3) Oxidation on different planes. As discussed in Chapter 6, a- and m-planes showed heavier oxidation than c-planes. A systematic study, including DFT simulation and surface chemistry experiments (XPS, AES in well controlled environment) needs to be performed to quantitatively study the oxidation susceptibility of different planes of GaN. This study will be conducive in understanding the performance of GaN device when different planes are utilized and working under various harsh environments.

(4) Doping effect on surface band bending and wear rate. It has been reported that the Fermi level of a semiconductor will affect the dislocation velocity. This has not been confirmed yet on III-Nitrides. Furthermore, n-type GaN has its band bends upwards while p-type GaN bends downwards. If we repeat the sliding on doped GaN, how the surface band bending will be altered?

(5) Besides high temperature growth, low temperature and low pressure growth of GaN has emerged. This various growth condition can effectively alter the dislocation density of GaN. As discussed in Chapter 6 and Chapter 7, dislocation density will not only influence the wear rate of this material, but also affect the surface band bending. Conducting tribological test on GaN grown with different temperature and pressure can directly link the defect effect to the wear performance and help us better understand the role of defect in GaN wear mechanism as well as its surface band bending alteration.

(6) Crystallographic dependency of GaN band bending. As discussed previously in Chapter 1.2.2 and Chapter 7, reconstruction, polarization and arrangement of atoms at different crystal planes are so different from each other, results in different

bending of energy band. This is the intrinsic surface charge property of GaN that gives rise to different band bending at different planes. Furthermore, dislocation has its favorite slip planes for further propagation, sliding on different crystal planes will generate different amount of defects underneath the surface. Therefore, both of these factors will influence the tribodoping effect on GaN.

Tribological study of GaN is an interdisciplinary research area that covers the material science, mechanical engineering, electronic engineering, physics and surface chemistry. Since our work is the first time providing the insight into this area, there are still humongous questions need to be answered. We hope that this pioneering work can attract more attention into this new area. With better understanding of the wear performance of GaN as well as tribodoping phenomenon, more applications of GaN and possibly other allied III-Nitrides can be expected to emerge in the near future.

9 References

[1] B. Bhushan, *Introduction to tribology*. John Wiley & Sons, 2013.

[2] T. Mang, K. Bobzin, and T. Bartels, *Industrial Tribology: Tribosystems, Friction, Wear and Surface Engineering, Lubrication*. Wiley-VCH, 2011.

[3] "Tribology," 2017. [Online]. Available: https://en.wikipedia.org/wiki/Tribology.

[4] "http://www.nobelprize.org/nobel_prizes/physics/laureates/2014/." .

[5] U. K. Mishra, L. Shen, T. E. Kazior, and Y. F. Wu, "GaN-based RF power devices and amplifiers," *Proc. IEEE*, vol. 96, no. 2, pp. 287–305, 2008.

[6] P. Pust, P. J. Schmidt, and W. Schnick, "A revolution in lighting," *Nat. Mater.*, vol. 14, pp. 454–458, 2015.

[7] M. H. Crawford, "LEDs for solid-state lighting: performance challenges and recent advances," *IEEE J. Sel. Top. Quantum Electron.*, vol. 15, no. 4, pp. 1028–1040, 2009.

[8] N. Tansu, H. P. Zhao, G. Y. Liu, X. H. Li, J. Zhang, H. Tong, and Y. K. Ee, "III-nitride photonics," *IEEE Photonics J.*, vol. 2, pp. 241–248, 2010.

[9] J. Y. Tsao, M. H. Crawford, M. E. Coltrin, A. J. Fischer, D. D. Koleske, G. S. Subramania, G. T. Wang, J. J. Wierer, and R. F. Karlicek Jr., "Toward smart and ultra-efficient solid-state lighting," *Adv. Opt. Mater.*, vol. 2, pp. 809–836, 2014.

[10] S. J. Pearton, F. Ren, Y. L. Wang, B. H. Chu, K. H. Chen, C. Y. Chang, W. Lim, J. Lin, and D. P. Norton, "Recent advances in wide bandgap semiconductor biological and gas sensors," *Prog. Mater. Sci.*, vol. 55, no. 1, pp. 1–59, 2010.

[11] J. Piprek, *Nitride Semiconductor Devices: Principles and Simulation*. Wiley-VCH, 2007.

[12] R. Dingle, D. D. Sell, S. E. Stokowski, and M. Ilegems, “Absorption, reflectance, and luminescence of GaN epitaxial layers,” *Phys. Rev. B*, vol. 4, no. 4, pp. 1211–1218, 1971.

[13] B. Monemar, “Fundamental energy gap of GaN from photoluminescence excitation spectra,” *Phys. Rev. B*, vol. 10, pp. 676–681, 1974.

[14] W. Shan, T. J. Schmidt, X. H. Yang, S. J. Hwang, J. J. Song, and B. Goldenberg, “Temperature dependence of interband transitions in GaN grown by metalorganic chemical vapor deposition,” *Appl. Phys. Lett.*, vol. 985, no. 1995, p. 985, 1995.

[15] C. F. Li, Y. S. Huang, L. Malikova, and F. H. Pollak, “Temperature dependence of the energies and broadening parameters of the interband excitonic transitions in wurtzite GaN,” *Phys. Rev. B*, vol. 55, no. 15, pp. 9251–9254, 1997.

[16] A. Shikanai, T. Azuhata, T. Sota, S. Chichibu, A. Kuramata, K. Horino, and S. Nakamura, “Biaxial strain dependence of exciton resonance energies in wurtzite GaN,” *J. Appl. Phys.*, vol. 81, no. 1, p. 417, 1997.

[17] S. Pereira, M. R. Correia, E. Pereira, K. P. O’Donnell, E. Alves, a. D. Sequeira, N. Franco, I. M. Watson, and C. J. Deatcher, “Strain and composition distributions in wurtzite InGaN/GaN layers extracted from x-ray reciprocal space mapping,” *Appl. Phys. Lett.*, vol. 80, no. 21, pp. 3913–3915, 2002.

[18] A. Castaldini, A. Cavallini, and L. Polenta, “Thickness-related features observed in GaN epitaxial layers,” *Appl. Phys. Lett.*, vol. 84, no. 24, p. 4851, 2004.

[19] J. Bai, T. Wang, and S. Sakai, "Study of the strain relaxation in InGaN/GaN multiple quantum well structures," *J. Appl. Phys.*, vol. 90, no. 4, pp. 1740–1744, 2001.

[20] O. Ambacher, J. Majewski, C. Miskys, A. Link, M. Hermann, M. Eickhoff, M. Stutzmann, F. Bernardini, V. Fiorentini, V. Tilak, B. Schaff, and L. F. Eastman, "Pyroelectric properties of Al(In)GaN/GaN hetero- and quantum well structures," *J. Phys. Condens. Matter*, vol. 14, pp. 3399–3434, 2002.

[21] R. A. Arif, Y. K. Ee, and N. Tansu, "Polarization engineering via staggered InGaN quantum wells for radiative efficiency enhancement of light emitting diodes," *Appl. Phys. Lett.*, vol. 91, no. 9, pp. 2005–2008, 2007.

[22] H. Zhao, G. Liu, J. Zhang, J. D. Poplawsky, V. Dierolf, and N. Tansu, "Approaches for high internal quantum efficiency green InGaN light-emitting diodes with large overlap quantum wells," *Opt. Express*, vol. 19, no. S4, pp. A991–A1007, 2011.

[23] M. G. Kibria, S. Zhao, F. A. Chowdhury, Q. Wang, H. P. Nguyen, M. L. Trudeau, H. Guo, and Z. Mi, "Tuning the surface Fermi level on p-type gallium nitride nanowires for efficient overall water splitting," *Nat. Commun.*, vol. 5, p. 3825, 2014.

[24] X. Li, J. Yu, J. Low, Y. Fang, J. Xiao, and X. Chen, "Engineering heterogeneous semiconductors for solar water splitting," *J. Mater. Chem. A*, vol. 3, pp. 2485–2534, 2015.

[25] C. J. Neufeld, N. G. Toledo, S. C. Cruz, M. Iza, S. P. DenBaars, and U. K. Mishra, "High quantum efficiency InGaN/GaN solar cells with 2.95 eV band gap," *Appl. Phys. Lett.*, vol. 93, no. 14, pp. 91–94, 2008.

[26] R. Dahal, B. Pantha, J. Li, J. Y. Lin, and H. X. Jiang, "InGaN/GaN multiple quantum

well solar cells with long operating wavelengths," *Appl. Phys. Lett.*, vol. 94, no. 6, 2009.

[27] X. Zhang and S. Ptasinska, "Electronic and chemical structure of the H2O/GaN(0001) interface under ambient conditions," *Sci. Rep.*, no. April, pp. 1–7, 2016.

[28] N. J. Watkins, G. W. Wicks, and Y. Gao, "Oxidation study of GaN using x-ray photoemission spectroscopy," *Appl. Phys. Lett.*, vol. 75, no. 17, pp. 2602–2604, 1999.

[29] V. M. Bermudez, "Study of oxygen chemisorption on the GaN(0001)-(1×1) surface," *J. Appl. Phys.*, vol. 80, no. 2, pp. 1190–1200, 1996.

[30] M. Z. Iqbal, M. a. Reshchikov, L. He, and H. Morkoç, "Effect of ambient on photoluminescence from GaN grown by molecular-beam epitaxy," *J. Electron. Mater.*, vol. 32, no. 5, pp. 346–349, 2003.

[31] S. D. Wolter, J. M. DeLucca, S. E. Mohney, R. S. Kern, and C. P. Kuo, "An investigation into the early stages of oxide growth on gallium nitride," *Thin Solid Films*, vol. 371, no. 1–2, pp. 153–160, 2000.

[32] I. Shalish, Y. Shapira, L. Burstein, and J. Salzman, "Surface states and surface oxide in GaN layers," *J. Appl. Phys.*, vol. 89, no. 1, pp. 390–395, 2001.

[33] H. S. Oon and K. Y. Cheong, "Recent development of gallium oxide thin film on GaN," *Mater. Sci. Semicond. Process.*, vol. 16, no. 5, pp. 1217–1231, 2013.

[34] D. P. Williams, S. Schulz, a. D. Andreev, and E. P. O'Reilly, "Theory of GaN Quantum Dots for Optical Applications," *IEEE J. Sel. Top. Quantum Electron.*, vol.

15, no. 4, pp. 1092–1103, 2009.

[35] M. Mishra, S. K. Tc, N. Aggarwal, and G. Gupta, “Surface chemistry and electronic structure of nonpolar and polar GaN films,” *Appl. Surf. Sci.*, vol. 345, pp. 440–447, 2015.

[36] M. A. Garcia, S. D. Wolter, T. H. Kim, S. Choi, J. Baier, A. Brown, M. Losurdo, and G. Bruno, “Surface oxide relationships to band bending in GaN,” *Appl. Phys. Lett.*, vol. 88, p. 13506, 2006.

[37] K. Prabhakaran, T. G. Andersson, and K. Nozawa, “Nature of native oxide on GaN surface and its reaction with Al,” *Appl. Phys. Lett.*, vol. 69, no. 21, p. 3212, 1996.

[38] V. M. Bermudez, “Chemisorption of NH3 on GaN (0001)-(1×1),” *Chem. Phys. Lett.*, vol. 317, pp. 290–295, 2000.

[39] T. K. Zywietz, J. Neugebauer, and M. Scheffler, “The adsorption of oxygen at GaN surfaces,” *Appl. Phys. Lett.*, vol. 74, no. 12, p. 1695, 1999.

[40] H. Ye, G. Chen, H. Niu, Y. Zhu, L. Shao, and Z. Qiao, “Structures and Mechanisms of Water Adsorption on ZnO (0001) and GaN (0001) Surface,” *J Phys Chem C*, vol. 117, no. 1, p. 15976, 2013.

[41] X. Shen, P. B. Allen, M. S. Hybertsen, and J. T. Muckerman, “Water Adsorption on the GaN (101-0) Nonpolar Surface,” *J. Phys. Chem. C*, vol. 113, no. 9, pp. 3365–3368, 2009.

[42] F. Gao, D. Chen, H. L. Tuller, C. V. Thompson, and T. Palacios, “On the redox origin of surface trapping in AlGaN/GaN high electron mobility transistors,” *J. Appl. Phys.*, vol. 115, no. 12, 2014.

[43] S. W. King, J. P. Barnak, M. D. Bremser, K. M. Tracy, C. Ronning, R. F. Davis, and R. J. Nemanich, "Cleaning of AlN and GaN surfaces," *J. Appl. Phys.*, vol. 84, no. 9, pp. 5248–5260, 1998.

[44] V. M. Bermudez, "Functionalizing the GaN(0001)-(1×1) surface I. Chemisorption of aniline," vol. 499, pp. 109–123, 2002.

[45] V. M. Bermudez, "Functionalizing the GaN(0001)-(1×1) surface II. Chemisorption of 3-pyrroline," *Surf. Sci.*, vol. 499, pp. 124–134, 2002.

[46] V. M. Bermudez, "Adsorption of 1-octanethiol on the GaN(0001) surface," *Langmuir*, vol. 19, no. 17, pp. 6813–6819, 2003.

[47] Z. Zhang and J. T. Yates, "Band Bending in Semiconductor Chemical and Physical Consequences at Surfaces and Interfaces.pdf," *Chem. Rev.*, vol. 112, pp. 5520–5551, 2012.

[48] W. Schottky, "Zur Halbleitertheorie der Sperrschicht- und Spitzengleichrichter," *Zeitschrift für Phys.*, vol. 113, no. 5–6, pp. 367–414, May 1939.

[49] N. F. Mott, "Note on the contact between a metal and an insulator or semi-conductor," *Math. Proc. Cambridge Philos. Soc.*, vol. 34, no. 4, p. 568, Oct. 1938.

[50] F. Flores and C. Tejedor, "On the formation of semiconductor interfaces," *J. Phys. C Solid State Phys.*, vol. 20, no. 2, pp. 145–175, Jan. 1987.

[51] A. Zangwill, *Physics at surfaces*. Cambridge university press, 1988.

[52] Z. Zhang and J. T. Yates, "Effect of adsorbed donor and acceptor molecules on electron stimulated desorption: O_2/TiO_2(110)," *J. Phys. Chem. Lett.*, vol. 1, no. 14, pp. 2185–2188, 2010.

[53] D. Caliskan, H. Sezen, E. Ozbay, and S. Suzer, “Chemical Visualization of a GaN p-n junction by XPS,” *Sci. Rep.*, vol. 5, p. 10040, 2015.

[54] D. Wang, A. Pierre, M. G. Kibria, K. Cui, X. Han, K. H. Bevan, H. Guo, S. Paradis, A. R. Hakima, and Z. Mi, “Wafer-level photocatalytic water splitting on gan nanowire arrays grown by molecular beam epitaxy,” *Nano Lett.*, vol. 11, no. 6, pp. 2353–2357, 2011.

[55] X. Shen, Y. A. Small, J. Wang, P. B. Allen, M. V Fernandez-Serra, M. S. Hybertsen, and J. T. Muckerman, “Photocatalytic Water Oxidation at the GaN(1010)-Water Interface,” *J. Phys. Chem. C*, vol. 114, no. 32, pp. 13695–13704, 2010.

[56] B. AlOtaibi, H. P. T. Nguyen, S. Zhao, M. G. Kibria, S. Fan, and Z. Mi, “Highly stable photoelectrochemical water splitting and hydrogen generation using a double-band InGaN/GaN core/shell nanowire photoanode,” *Nano Lett.*, vol. 13, no. 9, pp. 4356–4361, 2013.

[57] M. McEllistrem, G. Haase, D. Chen, and R. J. Hamers, “Electrostatic sample-tip interactions in the scanning tunneling microscope,” *Phys. Rev. Lett.*, vol. 70, no. 16, pp. 2471–2474, Apr. 1993.

[58] X. Ma, P. Chen, D. Li, Y. Zhang, and D. Yang, “Electrically pumped ZnO film ultraviolet random lasers on silicon substrate,” *Appl. Phys. Lett.*, vol. 91, no. 25, p. 251109, 2007.

[59] M. Ghosh and A. K. Raychaudhuri, “Electric field induced reversible control of visible photoluminescence from ZnO nanoparticles,” *Appl. Phys. Lett.*, vol. 98, no. 15, p. 153109, 2011.

[60] H. Onishi, T. Aruga, C. Egawa, and Y. Iwasawa, “Adsorption of CH_3OH, HCOOH and SO_2 on TiO_2(110) and stepped TiO_2(441) surfaces,” *Surf. Sci.*, vol. 193, no. 1–2, pp. 33–46, 1988.

[61] J. Zhao, J. Yang, and H. Petek, “Theoretical study of the molecular and electronic structure of methanol on a TiO_2(110) surface,” *Phys. Rev. B*, vol. 80, no. 23, p. 235416, 2009.

[62] A. Furube, T. Asahi, H. Masuhara, H. Yamashita, and M. Anpo, “Charge Carrier Dynamics of Standard TiO_2 Catalysts Revealed by Femtosecond Diffuse Reflectance Spectroscopy,” *J. Phys. Chem. B*, vol. 103, no. 16, pp. 3120–3127, 1999.

[63] T. Berger, M. Sterrer, O. Diwald, and E. Knözinger, “Charge trapping and photoadsorption of O_2 on dehydroxylated TiO_2 nanocrystals - An electron paramagnetic resonance study,” *ChemPhysChem*, vol. 6, no. 10, pp. 2104–2112, 2005.

[64] M. Setvin, J. Hulva, G. S. Parkinson, M. Schmid, and U. Diebold, “Electron transfer between anatase TiO_2 and an O_2 molecule directly observed by atomic force microscopy,” *Proc. Natl. Acad. Sci.*, p. 201618723, 2017.

[65] C. Engler and W. Lorenz, “Chemisorption on semiconductor surfaces: generalized expression of partial charge injection and adsorption energy,” *Surf. Sci.*, vol. 104, pp. 549–558, 1981.

[66] P. B. Weisz, “Effects of Electronic Charge Transfer between Adsorbate and Solid on Chemisorption and Catalysis,” *J. Chem. Phys.*, vol. 21, p. 1531, 1953.

[67] P. B. Weisz, “Electronic Barrier Layer Phenomena in Chemisorption and Catalysis,” *J. Chem. Phys.*, vol. 20, p. 1483, 1952.

[68] U. Diebold, “The surface science of titanium dioxide,” *Surf. Sci. Rep.*, vol. 48, no. 5–8, pp. 53–229, 2003.

[69] H.-F. Ji, W.-K. Liu, S. Li, Y. Li, Z.-F. Shi, Y.-T. Tian, and X.-J. Li, “High-performance methanol sensor based on GaN nanostructures grown on silicon nanoporous pillar array,” *Sensors Actuators B Chem.*, vol. 250, pp. 518–524, 2017.

[70] G. S. Aluri, A. Motayed, A. V Davydov, V. P. Oleshko, K. A. Bertness, N. A. Sanford, and M. V Rao, “Highly selective GaN-nanowire/TiO2-nanocluster hybrid sensors for detection of benzene and related environment pollutants,” *Nanotechnology*, vol. 22, no. 29, p. 295503, 2011.

[71] G. S. Aluri, A. Motayed, A. V Davydov, V. Oleshko, K. A. Bertness, N. A. Sanford, and M. V Rao, “GaN-nanowire/TiO2-nanocluster hybrid sensors for detection of Benzene and related aromatic compounds,” in *Proc. of SPIE Vol*, 2010, vol. 8024, p. 80240M–1.

[72] Y. Halfaya, C. Bishop, A. Soltani, S. Sundaram, V. Aubry, P. L. Voss, J.-P. Salvestrini, and A. Ougazzaden, “Investigation of the performance of HEMT-based NO, NO2 and NH3 exhaust gas sensors for automotive antipollution systems,” *Sensors*, vol. 16, no. 3, p. 273, 2016.

[73] K. P. Beh, F. K. Yam, L. K. Tan, S. W. Ng, C. W. Chin, and Z. Hassan, “Photoelectrochemical fabrication of porous GaN and their applications in ultraviolet and ammonia sensing,” *Jpn. J. Appl. Phys.*, vol. 52, no. 8S, p. 08JK03,

2013.

[74] P.-C. Chou, H.-I. Chen, I.-P. Liu, C.-W. Hung, C.-C. Chen, J.-K. Liou, and W.-C. Liu, “Study of an electroless plating (EP)-based Pt/AlGaN/GaN Schottky diode-type ammonia sensor,” *Sensors Actuators B Chem.*, vol. 203, pp. 258–262, 2014.

[75] A. Patsha, P. Sahoo, S. Amirthapandian, A. K. Prasad, A. Das, A. K. Tyagi, M. A. Cotta, and S. Dhara, “Localized Charge Transfer Process and Surface Band Bending in Methane Sensing by GaN Nanowires,” *J. Phys. Chem. C*, vol. 119, no. 36, pp. 21251–21260, 2015.

[76] Y. Xi, L. Liu, F. Ren, S. J. Pearton, J. Kim, A. Dabiran, and P. P. Chow, “Methane detection using Pt-gated AlGaN/GaN high electron mobility transistor based Schottky diodes,” *J. Vac. Sci. Technol. B, Nanotechnol. Microelectron. Mater. Process. Meas. Phenom.*, vol. 31, no. 3, p. 32203, 2013.

[77] R. S. Chen, C. Y. Lu, K. H. Chen, and L. C. Chen, “Molecule-modulated photoconductivity and gain-amplified selective gas sensing in polar GaN nanowires,” *Appl. Phys. Lett.*, vol. 95, no. 23, p. 233119, 2009.

[78] A. Ramizy, Z. Hassan, and K. Omar, “Porous GaN on Si (111) and its application to hydrogen gas sensor,” *Sensors Actuators B Chem.*, vol. 155, no. 2, pp. 699–708, 2011.

[79] T. Anderson, F. Ren, S. Pearton, B. S. Kang, H.-T. Wang, C.-Y. Chang, and J. Lin, “Advances in hydrogen, carbon dioxide, and hydrocarbon gas sensor technology using GaN and ZnO-based devices,” *Sensors*, vol. 9, no. 6, pp. 4669–4694, 2009.

[80] J. S. Wright, W. Lim, B. P. Gila, S. J. Pearton, J. L. Johnson, A. Ural, and F. Ren,

"Hydrogen sensing with Pt-functionalized GaN nanowires," *Sensors Actuators B Chem.*, vol. 140, no. 1, pp. 196–199, 2009.

[81] Q. N. Abdullah, F. K. Yam, Z. Hassan, and M. Bououdina, "Hydrogen gas sensing performance of GaN nanowires-based sensor at low operating temperature," *Sensors Actuators B Chem.*, vol. 204, pp. 497–506, 2014.

[82] S.-T. Hung, C.-J. Chang, C.-H. Hsu, B. H. Chu, C. F. Lo, C.-C. Hsu, S. J. Pearton, M. R. Holzworth, P. G. Whiting, and N. G. Rudawski, "SnO_2 functionalized AlGaN/GaN high electron mobility transistor for hydrogen sensing applications," *Int. J. Hydrogen Energy*, vol. 37, no. 18, pp. 13783–13788, 2012.

[83] Y.-L. Wang, F. Ren, W. Lim, S. J. Pearton, K. H. Baik, S.-M. Hwang, Y. G. Seo, and S. Jang, "Hydrogen sensing characteristics of non-polar a-plane GaN Schottky diodes," *Curr. Appl. Phys.*, vol. 10, no. 4, pp. 1029–1032, 2010.

[84] S. Jang, P. Son, J. Kim, S.-N. Lee, and K. H. Baik, "Hydrogen sensitive Schottky diode using semipolar AlGaN/GaN heterostructures," *Sensors Actuators B Chem.*, vol. 222, pp. 43–47, 2016.

[85] C. Y. Chang, B. S. Kang, H. T. Wang, F. Ren, Y. L. Wang, S. J. Pearton, D. M. Dennis, J. W. Johnson, P. Rajagopal, and J. C. Roberts, "CO_2 detection using polyethylenimine/starch functionalized Al GaN⁄ GaN high electron mobility transistors," *Appl. Phys. Lett.*, vol. 92, no. 23, p. 232102, 2008.

[86] Y.-L. Wang, B. H. Chu, C. Y. Chang, C. F. Lo, S. J. Pearton, A. Dabiran, P. P. Chow, and F. Ren, "Long-term stability study of botulinum toxin detection with AlGaN/GaN high electron mobility transistor based sensors," *Sensors Actuators B*

Chem., vol. 146, no. 1, pp. 349–352, 2010.

[87] Y.-L. Wang, B. H. Chu, K. H. Chen, C. Y. Chang, T. P. Lele, Y. Tseng, S. J. Pearton, J. Ramage, D. Hooten, and A. Dabiran, "Botulinum toxin detection using AlGaN/ GaN high electron mobility transistors," *Appl. Phys. Lett.*, vol. 93, no. 26, p. 262101, 2008.

[88] K. Maeda, N. Sakamoto, T. Ikeda, H. Ohtsuka, A. Xiong, D. Lu, M. Kanehara, T. Teranishi, and K. Domen, "Preparation of Core–Shell-Structured Nanoparticles (with a Noble-Metal or Metal Oxide Core and a Chromia Shell) and Their Application in Water Splitting by Means of Visible Light," *Chem. Eur. J.*, vol. 16, no. 26, pp. 7750–7759, 2010.

[89] Y. J. Lin, Q. Ker, C. Y. Ho, H. C. Chang, and F. T. Chien, "Nitrogen-vacancy-related defects and Fermi level pinning in n-GaN Schottky diodes," *J. Appl. Phys.*, vol. 94, no. 3, pp. 1819–1822, 2003.

[90] K. Kim, J. H. Ryu, J. Kim, S. J. Cho, D. Liu, J. Park, I. K. Lee, B. Moody, W. Zhou, J. Albrecht, and Z. Ma, "Band-Bending of Ga-Polar GaN Interfaced with Al_2O_3 through Ultraviolet/Ozone Treatment," *ACS Appl. Mater. Interfaces*, vol. 9, no. 20, pp. 17576–17585, 2017.

[91] A. Hagfeldt and M. Grätzel, "Light-Induced Redox Reactions in Nanocrystalline Systems," *Chem. Rev.*, vol. 95, no. 1, pp. 49–68, 1995.

[92] C. G. Silva, R. Juárez, T. Marino, R. Molinari, and H. García, "Influence of excitation wavelength (UV or visible light) on the photocatalytic activity of titania containing gold nanoparticles for the generation of hydrogen or oxygen from

water.," *J. Am. Chem. Soc.*, vol. 133, no. 3, pp. 595–602, 2011.

[93] Z. Zhang, C. Wang, R. Zakaria, and J. Y. Ying, "Role of Particle Size in Nanocrystalline TiO_2 -Based Photocatalysts," *J. Phys. Chem. B*, vol. 102, pp. 10871–10878, 1998.

[94] N. Kislov, J. Lahiri, H. Verma, D. Y. Goswami, E. Stefanakos, and M. Batzill, "Photocatalytic Degradation of Methyl Orange over Single Crystalline ZnO : Orientation Dependence of Photoactivity and Photostability of ZnO Photocatalytic Degradation of Methyl Orange over Single Crystalline ZnO : Orientation Dependence of Photoactivity a," *Langmuir*, no. 25, pp. 3310–3315, 2009.

[95] J. Wang, L. S. Pedroza, A. Poissier, and M. V. Fernández-Serra, "Water Dissociation at the GaN($10\bar{1}0$) Surface: Structure, Dynamics and Surface Acidity," *J. Phys. Chem. C*, vol. 116, no. 27, pp. 14382–14389, 2012.

[96] V. A. Savastenko and A. U. Sheleg, "Study of the elastic properties of gallium nitride," *Phys. Status Solidi*, vol. 48, pp. K135–K139, 1978.

[97] a Polian, M. Grimsditch, and I. Grzegory, "Elastic constants of gallium nitride," *J. Appl. Phys.*, vol. 79, no. 6, pp. 3343–3344, 1996.

[98] R. B. Schwarz, K. Khachaturyan, and E. R. Weber, "Elastic moduli of gallium nitride," *Appl. Phys. Lett.*, vol. 70, no. 9, p. 1122, 1997.

[99] C. Deger, E. Born, H. Angerer, O. Ambacher, M. Stutzmann, J. Hornsteiner, E. Riha, and G. Fischerauer, "Sound velocity of AlxGa1-xN thin films obtained by surface acoustic-wave measurements," *Appl. Phys. Lett.*, vol. 72, no. 19, pp. 2400–2402, 1998.

[100] A. D. Bykhovski, B. L. Gelmont, and M. S. Shur, “Elastic strain relaxation and piezoeffect in GaN-AlN, GaN-AlGaN and GaN-InGaN superlattices,” *J. Appl. Phys.*, vol. 81, no. 9, p. 6332, 1997.

[101] U. M. E. Christmas, A. D. Andreev, and D. A. Faux, “Calculation of electric field and optical transitions in InGaN/GaN quantum wells,” *J. Appl. Phys.*, vol. 98, no. 7, 2005.

[102] Z. Yang, R. N. Wang, S. Jia, D. Wang, B. S. Zhang, K. M. Lau, and K. J. Chen, “Mechanical characterization of suspended GaN microstructures fabricated by GaN-on-patterned-silicon technique,” *Appl. Phys. Lett.*, vol. 88, no. 4, pp. 1–3, 2006.

[103] C. H. Tsai, S. R. Jian, and J. Y. Juang, “Berkovich nanoindentation and deformation mechanisms in GaN thin films,” *Appl. Surf. Sci.*, vol. 254, no. 7, pp. 1997–2002, 2008.

[104] R. Nowak, M. Pessa, M. Suganuma, M. Leszczynski, I. Grzegory, S. Porowski, and F. Yoshida, “Elastic and plastic properties of GaN determined by nano-indentation of bulk crystal,” *Appl. Phys. Lett.*, vol. 75, no. 14, p. 2070, 1999.

[105] M. D. Drory, J. W. Ager, T. Suski, I. Grzegory, and S. Porowski, “Hardness and fracture toughness of bulk single crystal gallium nitride,” *Appl. Phys. Lett.*, vol. 69, no. 26, p. 4044, 1996.

[106] S. O. Kucheyev, J. E. Bradby, J. S. Williams, C. Jagadish, M. Toth, M. R. Phillips, and M. V. Swain, “Nanoindentation of epitaxial GaN films,” *Appl. Phys. Lett.*, vol. 77, no. 21, p. 3373, 2000.

[107] J. M. Wheeler, C. Niederberger, C. Tessarek, S. Christiansen, and J. Michler,

"Extraction of plasticity parameters of GaN with high temperature, in situ micro-compression," *Int. J. Plast.*, vol. 40, pp. 140–151, 2013.

[108] P. Perlin, C. Jauberthie-Carillon, J. P. Itic, A. S. Miguel, I. Grzegory, and A. Polian, "Raman scattering and x-ray-absorption spectroscopy in gallium nitritie under high pressure," *Phys. Rev. B*, vol. 45, no. 1, pp. 83–89, 1992.

[109] M. Ueno, M. Yoshida, A. Onodera, O. Shimomura, and K. Takemura, "Stability of the wurtzite-type structure under high pressure: GaN and InN," *Phys. Rev. B*, vol. 49, no. 1, pp. 14–21, 1994.

[110] H. Xia, Q. Xia, and A. L. Ruoff, "High-pressure structure of gallium nitride: Wurtzite-to-rocksalt phase transition," *Phys. Rev. B*, vol. 47, no. 19, p. 12 925-12 928, 1993.

[111] P. E. Van Camp, V. E. Van Doren, and J. T. Devreese, "High pressure structural phase transformation in gallium nitride," *Solid State Commun.*, vol. 81, no. 1, pp. 23–26, 1992.

[112] A. Munoz and K. Kunc, "High-pressure phase of gallium nitride," *Phys. Rev. B*, vol. 44, no. 18, p. 10 372-10 373, 1991.

[113] P. Puech, F. Demangeot, J. Frandon, C. Pinquier, M. Kuball, V. Domnich, and Y. G. Gogotsi, "GaN nanoindentation: A micro-Raman spectroscopy study of local strain fields," *J. Appl. Phys.*, vol. 96, no. 5, pp. 2853–2856, 2004.

[114] M. H. Lin, H. C. Wen, Y. R. Jeng, and C. P. Chou, "Nanoscratch characterization of GaN epilayers on c- and a-Axis sapphire substrates," *Nanoscale Res. Lett.*, vol. 5, no. 11, pp. 1812–1816, 2010.

[115] H. Aida, H. Takeda, K. Koyama, H. Katakura, K. Sunakawa, and T. Doi, “Chemical Mechanical Polishing of Gallium Nitride with Colloidal Silica,” *J. Electrochem. Soc.*, vol. 158, no. 12, p. H1206, 2011.

[116] Y. Huaiyue, X. Xiangqian, L. Zhanhui, Z. Rong, H. Xuemei, X. Zili, H. Ping, S. Yi, and Z. Youdou, “Chemical mechanical polishing of freestanding GaN substrates,” *J. Semicond.*, vol. 30, no. 2, p. 23003, 2009.

[117] P. R. Tavernier, T. Margalith, L. a. Coldren, S. P. DenBaars, and D. R. Clarke, “Chemical Mechanical Polishing of Gallium Nitride,” *Electrochem. Solid-State Lett.*, vol. 5, no. 8, p. G61, 2002.

[118] S. Hayashi, T. Koga, and M. S. Goorsky, “Chemical Mechanical Polishing of GaN,” *J. Electrochem. Soc.*, vol. 155, no. 2, p. H113, 2008.

[119] H. Aida, H. Takeda, S. W. Kim, N. Aota, K. Koyama, T. Yamazaki, and T. Doi, “Evaluation of subsurface damage in GaN substrate induced by mechanical polishing with diamond abrasives,” *Appl. Surf. Sci.*, vol. 292, pp. 531–536, 2014.

[120] H. Gong, G. Pan, Y. Zhou, X. Shi, C. Zou, and S. Zhang, “Investigation on the surface characterization of Ga-faced GaN after chemical-mechanical polishing,” *Appl. Surf. Sci.*, vol. 338, pp. 85–91, 2015.

[121] H. Aida, S. -w. Kim, T. Suzuki, K. Koyama, N. Aota, T. Doi, and T. Yamazaki, “Surface Planarization of GaN-on-Sapphire Template by Chemical Mechanical Polishing for Subsequent GaN Homoepitaxy,” *ECS J. Solid State Sci. Technol.*, vol. 3, no. 5, pp. P163–P168, 2014.

[122] H. Aida, T. Doi, H. Takeda, H. Katakura, S. W. Kim, K. Koyama, T. Yamazaki, and

M. Uneda, “Ultraprecision CMP for sapphire, GaN, and SiC for advanced optoelectronics materials,” *Curr. Appl. Phys.*, vol. 12, pp. S41–S46, 2012.

[123] J. Wang, T. Wang, G. Pan, and X. Lu, “Effect of photocatalytic oxidation technology on GaN CMP,” *Appl. Surf. Sci.*, vol. 361, pp. 18–24, 2016.

[124] J. Wang, T. Wang, G. Pan, and X. Lu, “Effects of catalyst concentration and ultraviolet intensity on chemical mechanical polishing of GaN,” *Appl. Surf. Sci.*, vol. 378, pp. 130–135, 2016.

[125] H. Deng, K. Endo, and K. Yamamura, “Atomic-scale and pit-free flattening of GaN by combination of plasma pretreatment and time-controlled chemical mechanical polishing,” *Appl. Phys. Lett.*, vol. 107, no. 5, p. 51602, 2015.

[126] G. Zeng, C. K. Tan, N. Tansu, and B. A. Krick, “Ultralow wear gallium nitride,” *Appl. Phys. Lett.*, vol. 109, p. 51602, 2016.

[127] G. Zeng, X. Yang, C. H. Skinner, B. E. Koel, N. Tansu, and B. A. Krick, “Controlling factors of GaN wear,” *Tribol. Lubr. Technol.*, vol. 73, no. 3, pp. 22–28, 2017.

[128] G. Zeng, X. Yang, C.-K. Tan, C. J. Marvel, B. E. Koel, N. Tansu, and B. A. Krick, “Shear-induced band bending in GaN, under review,” *Sci. Adv.*

[129] G. Zeng, N. Tansu, and B. A. Krick, “Moisture dependent wear mechanism of gallium nitride,” *Tribol. Int.*, vol. 118, no. June 2017, pp. 120–127, 2018.

[130] G. Zeng, W. Sun, R. Song, N. Tansu, and B. A. Krick, “Crystal Orientation Dependence of Gallium Nitride Wear,” *Sci. Rep.*, vol. 7, p. 14126, 2017.

[131] S. M. Wiederhorn, “Moisture assisted crack growth in ceramics,” *Int. J. Fract.*

Mech., vol. 4, no. 2, pp. 171–177, 1968.

[132] Y. Kimura, K. Okada, and Y. Enomoto, “Sliding damage of silicon nitride in plane contact,” *Wear*, vol. 133, no. 1, pp. 147–161, 1989.

[133] H. Ishigaki, I. Kawaguchi, M. Iwasa, and Y. Toibana, “Friction and Wear of Hot Pressed Silicon Nitride and Other Ceramics,” *Trans. ASME*, vol. 108, no. October, pp. 514–521, 1986.

[134] J. Yu, L. Chen, L. Qian, D. Song, and Y. Cai, “Investigation of humidity-dependent nanotribology behaviors of Si(1 0 0)/SiO2 pair moving from stick to slip,” *Appl. Surf. Sci.*, vol. 265, pp. 192–200, 2013.

[135] J. Yu, S. H. Kim, B. Yu, L. Qian, and Z. Zhou, “Role of tribochemistry in nanowear of single-crystalline silicon,” *ACS Appl. Mater. Interfaces*, vol. 4, no. 3, pp. 1585–1593, 2012.

[136] K. Adachi, K. Kato, and N. Chen, “Wear map of ceramics,” *Wear*, vol. 203–204, pp. 291–301, 1997.

[137] N. S. J. Eiss and R. C. Fabiniak, “Chemical and Mechanical Mechanisms in Wear of Sapphire on Steel,” *J. Am. Ceram. Soc.*, vol. 49, no. 4, pp. 221–226, 1966.

[138] B. Yu, J. Gao, C. Jin, C. Xiao, J. Wu, H. Liu, S. Jiang, L. Chen, and L. Qian, “Humidity effects on tribochemical removal of GaAs surfaces,” *Appl. Phys. Express*, vol. 9, no. 6, 2016.

[139] B. Yu, J. Gao, L. Chen, and L. Qian, “Effect of sliding velocity on tribochemical removal of gallium arsenide surface,” *Wear*, vol. 331, pp. 59–63, 2014.

[140] T. E. Fischer and W. M. Mullins, “Chemical aspects of ceramic tribology,” *J. Phys.*

Chem., vol. 96, no. 14, pp. 5690–5701, 1992.

[141] A. Erdemir, S. Li, and Y. Jin, “Relation of certain quantum chemical parameters to lubrication behavior of solid oxides,” *Int. J. Mol. Sci.*, vol. 6, no. 6–8, pp. 203–218, 2005.

[142] V. S. R. Murthy, H. Kobayashi, S. Tsurekawa, N. Tamari, T. Watanabe, and K. Kato, “Influence of humidity and doping elements on the friction and wear of SiC in unlubricated sliding,” *Tribol. Int.*, vol. 37, pp. 353–364, 2004.

[143] X. Dong and S. Jahanmir, “Wear transition diagram for silicon nitride,” *Wear*, vol. 165, pp. 169–180, 1993.

[144] J. Yeon, A. C. T. Van Duin, and S. H. Kim, “Effects of Water on Tribochemical Wear of Silicon Oxide Interface: Molecular Dynamics (MD) Study with Reactive Force Field (ReaxFF),” *Langmuir*, vol. 32, no. 4, pp. 1018–1026, 2016.

[145] H. He, L. Qian, C. G. Pantano, and S. H. Kim, “Effects of humidity and counter-surface on tribochemical wear of soda-lime-silica glass,” *Wear*, vol. 342–343, pp. 100–106, 2015.

[146] M. G. Gee, “The formation of aluminium hydroxide in the sliding wear of alumina,” *Wear*, vol. 153, pp. 201–207, 1992.

[147] A. J. Perez-Unzueta, J. H. Beynon, and M. G. Gee, “Effects of surrounding atmosphere on the wear of sintered alumina,” *Wear*, vol. 146, pp. 179–196, 1991.

[148] M. G. Gee and N. M. Jennett, “High resolution characterisation of tribochemical films on alumina,” *Wear*, vol. 193, no. 2, pp. 133–145, 1996.

[149] M. A. Sidebottom, A. A. Pitenis, C. P. Junk, D. J. Kasprzak, G. S. Blackman, H. E.

Burch, K. L. Harris, W. G. Sawyer, and B. A. Krick, "Ultralow wear Perfluoroalkoxy (PFA) and alumina composites," *Wear*, vol. 362–363, pp. 179–185, 2016.

[150] A. a. Pitenis, K. L. Harris, C. P. Junk, G. S. Blackman, W. G. Sawyer, and B. A. Krick, "Ultralow Wear PTFE and Alumina Composites: It is All About Tribochemistry," *Tribol. Lett.*, vol. 57, no. 1, 2015.

[151] W. G. Sawyer, N. Argibay, D. L. Burris, and B. A. Krick, "Mechanistic Studies in Friction and Wear of Bulk Materials," *Annu. Rev. Mater. Res.*, vol. 44, no. 1, pp. 395–427, 2014.

[152] B. A. Krick, A. A. Pitenis, K. L. Harris, C. P. Junk, W. G. Sawyer, S. C. Brown, H. D. Rosenfeld, D. J. Kasprzak, R. S. Johnson, C. D. Chan, and G. S. Blackman, "Ultralow wear fluoropolymer composites: Nanoscale functionality from microscale fillers," *Tribol. Int.*, vol. 95, pp. 245–255, 2016.

[153] S.-R. Jian, C.-Y. Huang, and W.-C. Ke, "Nanoindentation responses of InN thin films," *J. Alloys Compd.*, vol. 609, pp. 125–128, 2014.

[154] I. Manika and J. Maniks, "Effect of substrate hardness and film structure on indentation depth criteria for film hardness testing," *J. Phys. D. Appl. Phys.*, vol. 41, no. 7, p. 74010, 2008.

[155] K. M. Taylor and C. Lenie, "Some properties of aluminum nitride," *J. Electrochem. Soc.*, vol. 107, no. 4, pp. 308–314, 1960.

[156] H. Amano, N. Sawaki, I. Akasaki, and Y. Toyoda, "Metalorganic vapor phase epitaxial growth of a high quality GaN film using an AlN buffer layer," *Appl. Phys.*

Lett., vol. 48, no. 5, pp. 353–355, 1986.

[157] S. Nakamura, “GaN growth using GaN buffer layer,” *Jpn. J. Appl. Phys.*, vol. 30, no. 10A, pp. L1705–L1707, 1991.

[158] I. Akasaki, H. Amano, K. Itoh, N. Koide, and K. Manabe, “GaN-based ultraviolet/blue light emitting devices,” *Inst. Phys. Conf. Ser.*, vol. 129, pp. 851–856, 1992.

[159] S. Nakamura, M. Senoh, and T. Mukai, “P-GaN/n-InGaN/n-GaN double-heterostructure blue-light-emitting diodes,” *Jpn. J. Appl. Phys.*, vol. 32, no. 1A/B, pp. L8–L11, 1993.

[160] O. H. Nam, M. D. Dremser, T. S. Zheleva, and R. F. Davis, “Lateral epitaxy of low defect density GaN layers via organometallic vapor phase epitaxy,” *Appl. Phys. Lett.*, vol. 71, no. 18, pp. 2638–2640, 1997.

[161] S. Nakamura, M. Senoh, S. Nagahama, N. Iwasa, T. Yamada, T. Matsushita, Y. Sugimoto, and H. Kiyoku, “Room-temperature continuous-wave operation of InGaN multi-quantum-well structure laser diodes,” *Appl. Phys. Lett.*, vol. 69, no. 26, pp. 4056–4058, 1996.

[162] I. Akasaki, H. Amano, M. Kito, and K. Hiramatsu, “Photoluminescence of Mg-doped p-type GaN and electroluminescence of GaN p-n junction LED,” *J. Lumin.*, vol. 48–49, pp. 666–670, 1991.

[163] S. Nakamura, M. Senoh, and T. Mukai, “Highly p-typed Mg-doped GaN films grown with GaN buffer layers,” *Jpn. J. Appl. Phys.*, vol. 30, no. 10A, pp. L1708–L1711, 1991.

[164] S. Nakamura, T. Mukai, M. Senoh, and N. Iwasa, “Thermal annealing effect on p-type Mg-doped GaN films,” *Jpn. J. Appl. Phys.*, vol. 31, no. 2B, pp. L139–L142, 1992.

[165] D. Feezell, J. S. Speck, S. P. DenBaars, and S. Nakamura, “Semipolar (20-2-1) InGaN/GaN light-emitting diodes for high-efficiency solid-state lighting,” *J. Disp. Tech*, vol. 9, no. 4, pp. 190–198, 2013.

[166] T. W. Yeh, Y. T. Lin, L. S. Stewart, P. D. Dapkus, R. Sarkissian, J. D. O’Brien, B. Ahn, and S. R. Nutt, “InGaN/GaN multiple quantum wells grown on nonpolar facets of vertical GaN nanorod arrays,” *Nano Lett.*, vol. 12, no. 6, pp. 3257–3262, 2012.

[167] C. K. Tan and N. Tansu, “Nanostructured lasers: electrons and holes get closer,” *Nat. Nanotechnol.*, vol. 10, no. 2, pp. 107–109, 2015.

[168] H. J. Kim, S. Choi, S. S. Kim, J. H. Ryou, P. D. Yoder, R. D. Dupuis, A. M. Fischer, K. W. Sun, and F. A. Ponce, “Improvement of quantum efficiency by employing active-layer-friendly lattice-matched InAlN electron blocking layer in green light-emitting diodes,” *Appl. Phys. Lett.*, vol. 96, no. 10, p. 101102, 2010.

[169] Y. Liu, A. Erdemir, and E. I. Meletis, “A study of the wear mechanism of diamond-like carbon films,” *Surf. Coatings Technol.*, vol. 82, no. 1–2, pp. 48–56, 1996.

[170] A. G. Khurshudov, K. Kato, and H. Koide, “Nano-wear of the diamond AFM probing tip under scratching of silicon, studied by AFM,” *Tribol. Lett.*, vol. 2, pp. 345–354, 1996.

[171] A. G. Khurshudov, K. Kato, and H. Koide, “Wear of the AFM diamond tip sliding against silicon,” *Wear*, vol. 203–204, pp. 22–27, 1997.

[172] P. Y. Yu and M. Cardona, *Fundamentals of Semiconductors*. Springer, 2010.

[173] J. Singh, *Electronic and Optoelectronic Properties of Semiconductor Structures*. Cambridge University Press, 2003.

[174] T. S. Cheng, L. C. Jenkins, S. E. Hooper, C. T. Foxon, J. W. Orton, and D. E. Lacklison, "Selective growth of zinc-blende, wurtzite, or a mixed phase of gallium nitride by molecular beam epitaxy," *Appl. Phys. Lett.*, vol. 66, no. 12, pp. 1509–1511, 1995.

[175] M. J. Paisley, Z. Sitar, J. B. Posthill, and R. F. Davis, "Growth of cubic phase gallium nitride by modified molecular-beam epitaxy," *J. Vac. Sci. Technol. A Vacuum, Surfaces, Film.*, vol. 7, no. 3, pp. 701–705, 1989.

[176] L. A. Bendersky, D. V. Tsvetkov, and Y. V. Melnik, "Transmission electron microscopy study of a defected zone in GaN on a SiC substrate grown by hydride vapor phase epitaxy," *J. Appl. Phys.*, vol. 94, no. 3, pp. 1676–1685, 2003.

[177] R. J. Molnara, W. Götz, L. T. Romano, and N. M. Johnson, "Growth of gallium nitride by hydride vapor-phase epitaxy," *J. Cryst. Growth*, vol. 178, no. 1–2, pp. 147–156, Jun. 1997.

[178] A. Usui, H. Sunakawa, A. Sakai, and A. Y. Atsushi, "Thick GaN Epitaxial Growth with Low Dislocation Density by Hydride Vapor Phase Epitaxy," *Jpn. J. Appl. Phys.*, vol. 36, no. 7B, pp. L899–L902, 1997.

[179] K. Naniwae, S. Itoh, H. Amano, K. Itoh, K. Hiramatsu, and I. Akasaki, "Growth of single crystal GaN substrate using hydride vapor phase epitaxy," *J. Cryst. Growth*, vol. 99, no. 1–4, pp. 381–384, 1990.

[180] S. Figge, T. Böttcher, S. Einfeldt, and D. Hommel, “In situ and ex situ evaluation of the film coalescence for GaN growth on GaN nucleation layers,” *J. Cryst. Growth*, vol. 221, no. 1–4, pp. 262–266, 2000.

[181] F. Brunner, H. Protzmann, M. Heuken, A. Knauer, M. Weyers, and M. Kneissl, “High temperature growth of AlN in a production scale 11×2’ MOVPE reactor,” *Phys. Status Solidi*, vol. 5, no. 6, pp. 1799–1801, 2008.

[182] W. C. Oliver and G. M. Pharr, “An Improved Technique for Determining Hardness and Elastic Modulus using Load and Displacement Sensing Indentation Experiments,” *J. Mater. Res.*, vol. 7, no. 6, pp. 1564–1583, 1992.

[183] H. Luth, *Solid Surfaces, Interfaces and Thin Films*. Springer, 2010.

[184] “Atomic-force microscopy.” [Online]. Available: https://en.wikipedia.org/wiki/Atomic-force_microscopy.

[185] K. Harafuji, T. Tsuchiya, and K. Kawamura, “Molecular dynamics simulation for evaluating melting point of wurtzite-type GaN crystal,” *J. Appl. Phys.*, vol. 96, no. 5, pp. 2501–2512, 2004.

[186] R. Martin, *Electronic Structure: Basic Theory and Practical Methods*. Cambridge University Press, 2004.

[187] L. H. Thomas, “The calculation of atomic fields,” *Proc. Cambridge Philos. Soc.*, vol. 23, no. 5, pp. 542–548, 1927.

[188] E. Fermi, “Un metodo statistico per la determinazione di alcune priorieta dell’ atome,” *Rend. Accad. Naz. Lincei*, vol. 6, pp. 602–607, 1927.

[189] P. Hohenberg and W. Kohn, “Inhomogeneous electron gas,” *Phys. Rev.*, vol. 136,

no. 864–871, 1964.

[190] W. Kohn and L. J. Sham, “Self-consistent equations including exchange and correlation effects,” *Phys. Rev.*, vol. 140, p. A1133, 1965.

[191] C. E. Dreyer, A. Janotti, and C. G. Van de Walle, “Absolute surface energies of polar and nonpolar planes of GaN,” *Phys. Rev. B*, vol. 89, p. 081305(R), 2014.

[192] Y. A. Du, Y.-W. Chen, and J.-L. Kuo, “First principles studies on the redox ability of (Ga(1-x)Zn(x))N(1-x)O(x) solid solutions and thermal reactions for H2 and O2 production on their surfaces,” *Phys. Chem. Chem. Phys.*, vol. 15, no. 45, pp. 19807–18, 2013.

[193] “Materials Design, Inc.” [Online]. Available: www.materialsdesign.com.

[194] Q. Guo and A. Yoshida, “Microhardness of indium nitride single crystal films,” *Jpn. J. Appl. Phys.*, vol. 33, no. Part 1, No.1A, pp. 90–91, 1994.

[195] F. Gao, J. He, E. Wu, S. Liu, D. Yu, D. Li, S. Zhang, and Y. Tian, “Hardness of covalent crystals,” *Phys. Rev. Lett.*, vol. 91, no. 1, p. 15502, 2003.

[196] J. H. Edgar, C. H. Wei, D. T. Smith, T. J. Kistenmacher, and W. A. Bryden, “Hardness, elastic modulus and structure of indium nitride thin films on AlN-nucleated sapphire substrates,” *J. Mater. Sci. Mater. Electron.*, vol. 8, pp. 307–312, 1997.

[197] F. P. Bowden, C. A. Brookes, and A. E. Hanwell, “Anisotropy of Friction in Crystals,” *Nature*, vol. 203, pp. 27–30, 1964.

[198] R. P. Steijn, “Friction and Wear of Single Crystals,” *Wear*, vol. 7, pp. 48–66, 1964.

[199] R. P. Steijn, “On the wear of sapphire,” *J. Appl. Phys.*, vol. 32, no. 10, pp. 1951–1958, 1961.

[200] E. J. Duwell, “Friction and wear of single-crystal sapphire sliding on steel,” *J. Appl. Phys.*, vol. 33, no. 9, pp. 2691–2698, 1962.

[201] E. W. Taylor and M. Cooke, “Correlation of the Mohs’s Scale of Hardness with the Vickers’s Hardness Numbers,” *Mineral. Mag.*, vol. 28, pp. 718–721, 1949.

[202] D. H. Buckley and K. Miyoshi, “Friction and wear of ceramics,” *Wear*, vol. 100, no. 1–3, pp. 333–353, 1984.

[203] F. P. Bowden and C. A. Brookes, “Frictional anisotropy in nonmetallic crystals,” *Proc. R. Soc. A Math. Phys. Eng. Sci.*, vol. 295, no. 1442, pp. 244–258, 1966.

[204] S. El-Hadad, H. Sato, and Y. Watanabe, “Investigation of wear anisotropy in a severely deformed Al-Al3Ti composite,” *Metall. Mater. Trans. A Phys. Metall. Mater. Sci.*, vol. 43, no. 9, pp. 3249–3256, 2012.

[205] H. H. Gatzen and M. Beck, “Investigations on the friction force anisotropy of the silicon lattice,” *Wear*, vol. 254, no. 11, pp. 1122–1126, 2003.

[206] S. E. Kadijk and A. B. V. A. N. Groenou, “Wear anisotropy of MnZn ferrite part I: recorder and sphere-on-tape experiments,” *Wear*, vol. 139, pp. 93–113, 1990.

[207] M. Liley, “Friction Anisotropy and Asymmetry of a Compliant Monolayer Induced by a Small Molecular Tilt,” *Science (80-.).*, vol. 280, no. 5361, pp. 273–275, 1998.

[208] K. Miyoshi and D. H. Buckley, “Anisotropic tribological properties of SiC,” *Wear*, vol. 75, no. 2, pp. 253–268, 1982.

[209] Y. Namai and H. Shindo, “Frictional force microscopic anisotropy on (001) surfaces of alkali halides and MgO,” *Jpn. J. Appl. Phys.*, vol. 39, no. 7 B, pp. 4497–4500, 2000.

[210] J. Y. Park, D. F. Ogletree, M. Salmeron, R. A. Ribeiro, P. C. Canfield, C. J. Jenks, and P. A. Thiel, “High frictional anisotropy of periodic and aperiodic directions on a quasicrystal surface,” *Science*, vol. 309, no. 5739, pp. 1354–1356, 2005.

[211] L. Pastewka, S. Moser, P. Gumbsch, and M. Moseler, “Anisotropic mechanical amorphization drives wear in diamond,” *Nat. Mater.*, vol. 10, no. 1, pp. 34–38, 2011.

[212] P. Stempfle and J. Takadoum, “Multi-asperity nanotribological behavior of single-crystal silicon: Crystallography-induced anisotropy in friction and wear,” *Tribol. Int.*, vol. 48, pp. 35–43, 2012.

[213] B. Yu and L. Qian, “Effect of crystal plane orientation on the friction-induced nanofabrication on monocrystalline silicon,” *Nanoscale Res. Lett.*, vol. 8, pp. 137–144, 2013.

[214] R. S. Colbert, B. A. Krick, A. C. Dunn, J. R. Vail, N. Argibay, and W. G. Sawyer, “Uncertainty in Pin-on-Disk Wear Volume Measurements Using Surface Scanning Techniques,” *Tribol. Lett.*, vol. 42, no. 1, pp. 129–131, 2011.

[215] T. D. B. Jacobs and R. W. Carpick, “Nanoscale wear as a stress-assisted chemical reaction,” *Nat. Nanotechnol.*, vol. 8, no. 2, pp. 108–12, 2013.

[216] M. K. Beyer and H. Clausen-schaumann, “Mechanochemistry : The Mechanical Activation of Covalent Bonds,” *Chem. Rev.*, vol. 105, no. 8, pp. 2921–2944, 2005.

[217] H. L. Adams, M. T. Garvey, U. S. Ramasamy, Z. Ye, A. Martini, and W. T. Tysoe,

"Shear induced mechanochemistry: Pushing molecules around," *J. Phys. Chem. C*, vol. 119, no. 13, pp. 7115–7123, 2015.

[218] R. W. Hertzberg, R. P. Vinci, and J. L. Hertzberg, *Deformation and Fracture Mechanics of Engineering Materials*, 5th editio. John Wiley & Sons, Inc., 2012.

[219] M. Rais-Zadeh, V. J. Gokhale, A. Ansari, M. Faucher, D. Theron, Y. Cordier, and L. Buchaillot, "Gallium nitride as an electromechanical material," *J. Microelectromechanical Syst.*, vol. 23, no. 6, pp. 1252–1271, 2014.

[220] O. Ambacher, "Growth and applications of Group III-nitrides," *J. Phys. D Appl. Phys.*, vol. 31, pp. 2653–2710, 1998.

[221] X. Xu, R. P. Vaudo, and G. R. Brandes, "Fabrication of GaN wafers for electronic and optoelectronic devices," *Opt. Mater. (Amst).*, vol. 23, pp. 1–5, 2003.

[222] J. L. Weyher, S. Müller, I. Grzegory, and S. Porowski, "Chemical polishing of bulk and epitaxial GaN," *J. Cryst. Growth*, vol. 182, pp. 17–22, 1997.

[223] P. G. Caldas, E. M. Silva, R. Prioli, J. Y. Huang, R. Juday, A. M. Fischer, and F. A. Ponce, "Plasticity and optical properties of GaN under highly localized nanoindentation stress fields," *J. Appl. Phys.*, vol. 121, no. 12, p. 125105, 2017.

[224] O. Z. Tan, M. C. H. Wu, V. Chihaia, and J.-L. Kuo, "Physisorption structure of water on the GaN polar surface: Force field development and molecular dynamics simulations," *J. Phys. Chem. C*, vol. 115, pp. 11684–11693, 2011.

[225] V. M. Bermudez and J. P. Long, "Chemisorption of H2O on GaN (0001)," *Surf. Sci.*, vol. 450, pp. 98–105, 2000.

[226] A. H. Chin, T. S. Ahn, H. Li, S. Vaddiraju, C. J. Bardeen, C. Z. Ning, and M. K.

Sunkara, “Photoluminescence of GaN nanowires of different crystallographic orientations,” *Nano Lett.*, vol. 7, no. 3, pp. 626–631, 2007.

[227] A. W. Adamson, *Physical Chemistry of Surfaces*, 4th ed. New York: John Wiley, 1982.

[228] Y. K. Ee, X. H. Li, J. Biser, W. Cao, H. M. Chan, R. P. Vinci, and N. Tansu, “Abbreviated MOVPE nucleation of III-nitride light-emitting diodes on nano-patterned sapphire,” *J. Cryst. Growth*, vol. 312, no. 8, pp. 1311–1315, 2010.

[229] C. Schulz, S. Kuhr, H. Geffers, T. Schmidt, J. I. Flege, T. Aschenbrenner, D. Hommel, and J. Falta, “Cleaning of GaN(2110) surfaces,” *J. Vac. Sci. Technol. A Vacuum, Surfaces, Film.*, vol. 29, no. 1, p. 11013, 2011.

[230] M. Mishra, T. C. S. Krishna, N. Aggarwal, and G. Gupta, “Surface chemistry and electronic structure of nonpolar and polar GaN films,” *Appl. Surf. Sci.*, vol. 345, pp. 440–447, 2015.

[231] P. Lorenz, R. Gutt, T. Haensel, M. Himmerlich, J. A. Schaefer, and S. Krischok, “Interaction of GaN(0001)-2×2 surfaces with H2O,” *Phys. Status Solidi*, vol. 7, no. 2, pp. 169–172, 2010.

[232] S. D. Wolter, B. P. Luther, D. L. Waltemyer, C. Önneby, S. E. Mohney, and R. J. Molnar, “X-ray photoelectron spectroscopy and x-ray diffraction study of the thermal oxide on gallium nitride,” *Appl. Phys. Lett.*, vol. 70, no. 16, p. 2156, 1997.

[233] S. Poulston, P. M. Parlett, P. Stone, and M. Bowker, “Surface oxidation and reduction of CuO and Cu2O studied using XPS and XAES,” *Surf. Interface Anal.*, vol. 24, pp. 811–820, 1996.

[234] G. Moldovan, M. J. Roe, I. Harrison, M. Kappers, C. J. Humphreys, and P. D. Brown, “Effects of KOH etching on the properties of Ga-polar n-GaN surfaces,” *Philos. Mag.*, vol. 86, no. 16, pp. 2315–2327, Jun. 2006.

[235] C. D. Wagner, “Chemical shifts of Auger lines, and the Auger parameter,” *Faraday Discuss. Chem. Soc.*, vol. 60, pp. 291–300, 1975.

[236] M. A. Reshchikov, M. Foussekis, and A. A. Baski, “Surface photovoltage in undoped n-type GaN,” *J. Appl. Phys.*, vol. 107, no. 11, p. 113535, 2010.

[237] J. Elsner, R. Jones, M. Heggie, P. Sitch, M. Haugk, T. Frauenheim, S. Öberg, and P. Briddon, “Deep acceptors trapped at threading-edge dislocations in GaN,” *Phys. Rev. B*, vol. 58, no. 19, pp. 12571–12574, 1998.

[238] N. G. Weimann, L. F. Eastman, D. Doppalapudi, H. M. Ng, and T. D. Moustakas, “Scattering of electrons at threading dislocations in GaN,” *J. Appl. Phys.*, vol. 83, no. 7, p. 3656, 1998.

[239] D. C. Look and J. R. Sizelove, “Dislocation scattering in GaN,” *Phys. Rev. Lett.*, vol. 82, no. 6, pp. 1237–1240, 1999.

[240] A. F. Wright and U. Grossner, “The effect of doping and growth stoichiometry on the core structure of a threading edge dislocation in GaN,” *Appl. Phys. Lett.*, vol. 73, no. 19, pp. 2751–2753, 1998.

[241] C. G. Van de Walle and J. Neugebauer, “First-principles calculations for defects and impurities: Applications to III-nitrides,” *J. Appl. Phys.*, vol. 95, no. 8, pp. 3851–3879, 2004.

[242] S. Barbet, R. Aubry, M. A. Di Forte-Poisson, J. C. Jacquet, D. Deresmes, T. Ḿlin,

and D. Th́ron, “Surface potential of n - and p -type GaN measured by Kelvin force microscopy,” *Appl. Phys. Lett.*, vol. 93, no. 21, p. 212107, 2008.

[243] M. Vasilopoulou, D. G. Georgiadou, A. Soultati, N. Boukos, S. Gardelis, L. C. Palilis, M. Fakis, G. Skoulatakis, S. Kennou, M. Botzakaki, S. Georga, C. A. Krontiras, F. Auras, D. Fattakhova-Rohlfing, T. Bein, T. A. Papadopoulos, D. Davazoglou, and P. Argitis, “Atomic-Layer-Deposited Aluminum and Zirconium Oxides for Surface Passivation of TiO2 in High-Efficiency Organic Photovoltaics,” *Adv. Energy Mater.*, vol. 4, no. 15, pp. 1–12, 2014.

[244] D. C. Gleason-rohrer, B. S. Brunschwig, and N. S. Lewis, “Measurement of the band bending and surface dipole at chemically functionalized Si(111)/vacuum interfaces,” *J. Phys. Chem. C*, vol. 117, pp. 18031–18042, 2013.

[245] Y. Zhang, D. Zherebetskyy, N. D. Bronstein, S. Barja, L. Lichtenstein, D. Schuppisser, L. W. Wang, A. P. Alivisatos, and M. Salmeron, “Charge percolation pathways guided by defects in quantum dot solids,” *Nano Lett.*, vol. 15, no. 5, pp. 3249–3253, 2015.

[246] M. El-Gomati, F. Zaggout, H. Jayacody, S. Tear, and K. Wilson, “Why is it possible to detect doped regions of semiconductors in low voltage SEM: A review and update,” *Surf. Interface Anal.*, vol. 37, no. 11, pp. 901–911, 2005.

[247] M. M. El-Gomati and T. C. R. Wells, “Very-low-energy electron microscopy of doped semiconductors,” *Appl. Phys. Lett.*, vol. 79, no. 18, pp. 2931–2933, 2001.

[248] S. Linic, P. Christopher, and D. B. Ingram, “Plasmonic-metal nanostructures for efficient conversion of solar to chemical energy,” *Nat. Mater.*, vol. 10, no. 12, pp.

911–921, 2011.

[249] T. Kim, M. Lee, T. G. Kim, W. Kim, and Y. Sung, "Surface Plasmon Resonance (SPR) Electron and Energy Transfer in Noble Metal − Zinc Oxide Composite Nanocrystals," no. November 2015, pp. 10079–10082, 2008.

[250] K. Awazu, M. Fujimaki, C. Rockstuhl, J. Tominaga, H. Murakami, Y. Ohki, N. Yoshida, and T. Watanabe, "A Plasmonic Photocatalyst Consisting of Silver Nanoparticles Embedded in Titanium Dioxide," *J. Am. Chem. Soc.*, vol. 130, no. 5, pp. 1676–1680, 2008.

[251] Z. Liu, W. Hou, P. Pavaskar, M. Aykol, and S. B. Cronin, "Plasmon Resonant Enhancement of Photocatalytic Water Splitting Under Visible Illumination," *Nano Lett.*, vol. 11, no. 3, pp. 1111–1116, Mar. 2011.

[252] E. Thimsen, F. Le Formal, M. Grätzel, and S. C. Warren, "Influence of Plasmonic Au Nanoparticles on the Photoactivity of Fe_2O_3 Electrodes for Water Splitting," *Nano Lett.*, vol. 11, no. 1, pp. 35–43, Jan. 2011.

[253] D. B. Ingram and S. Linic, "Water Splitting on Composite Plasmonic-Metal/Semiconductor Photoelectrodes: Evidence for Selective Plasmon-Induced Formation of Charge Carriers near the Semiconductor Surface," *J. Am. Chem. Soc.*, vol. 133, no. 14, pp. 5202–5205, Apr. 2011.

[254] A. Primo, T. Marino, A. Corma, R. Molinari, and H. García, "Efficient Visible-Light Photocatalytic Water Splitting by Minute Amounts of Gold Supported on Nanoparticulate CeO_2 Obtained by a Biopolymer Templating Method," *J. Am. Chem. Soc.*, vol. 133, no. 18, pp. 6930–6933, May 2011.

[255] C. Gomes Silva, R. Juárez, T. Marino, R. Molinari, and H. García, “Influence of Excitation Wavelength (UV or Visible Light) on the Photocatalytic Activity of Titania Containing Gold Nanoparticles for the Generation of Hydrogen or Oxygen from Water,” *J. Am. Chem. Soc.*, vol. 133, no. 3, pp. 595–602, Jan. 2011.

[256] M. Fedurco, J. Augustynski, C. Indiani, G. Smulevich, M. Antalík, M. Bánó, E. Sedlák, M. C. Glascock, and J. H. Dawson, “Electrochemistry of Unfolded Cytochrome *c* in Neutral and Acidic Urea Solutions,” *J. Am. Chem. Soc.*, vol. 127, no. 20, pp. 7638–7646, May 2005.

[257] Z. Mucsi, A. Szabó, I. Hermecz, Á. Kucsman, and I. G. Csizmadia, “Modeling Rate-Controlling Solvent Effects. The Pericyclic Meisenheimer Rearrangement of *N* -Propargylmorpholine *N* -Oxide,” *J. Am. Chem. Soc.*, vol. 127, no. 20, pp. 7615–7631, May 2005.

[258] Y. Tian and T. Tatsuma, “Mechanisms and Applications of Plasmon-Induced Charge Separation at TiO_2 Films Loaded with Gold Nanoparticles,” *J. Am. Chem. Soc.*, vol. 127, no. 20, pp. 7632–7637, May 2005.

[259] A. L. Linsebigler, G. Lu, and J. T. Yates, “Photocatalysis on TiO2 Surfaces: Principles, Mechanisms, and Selected Results,” *Chem. Rev.*, vol. 95, no. 3, pp. 735–758, 1995.

[260] Q. Z. Liu and S. S. Lau, “A review of the metal–GaN contact technology,” *Solid. State. Electron.*, vol. 42, no. 5, pp. 677–691, 1998.

[261] X. Yang, S. Kattel, S. D. Senanayake, J. A. Boscoboinik, X. Nie, J. Graciani, J. A. Rodriguez, P. Liu, D. J. Stacchiola, and J. G. Chen, “Low Pressure CO2

Hydrogenation to Methanol over Gold Nanoparticles Activated on a CeO_x/TiO_2 Interface," *J. Am. Chem. Soc.*, vol. 137, no. 32, pp. 10104–10107, 2015.

10 Vita

Guosong Zeng was born in Guilin, Guangxi, China in 1987. He was raised in Guilin, and spent 6 years in Foreign Language School Attached to Guangxi Normal University. During that period of time, he developed the ability to study and think independently, as well as strong interests in physical science. He also had great interests in basketball, soccer and some other sports. He went to Tianjin University in 2006 for his undergraduate study. He worked on FIB milling and SERS-based sensor design and fabrication in Prof. Fengzhou Fang's group since 2009. In 2010, he came to Lehigh to pursue the master of science degree under supervision of Professor Herman Nied. In 2014, Guosong joined Lehigh Tribology Laboratory to pursue the PhD degree under supervision of Professor Brandon A. Krick. In the tribology lab, he mainly focused on study of tribological properties of III-Nitrides and shear-induced modification of electronic properties of GaN. His work also includes the characterization of other materials, such as ALD coatings, steels, and some other ceramics. He received his Doctorate of Philosophy in mechanical engineering in 2017. Guosong has a goal of continuing his future work in academia and interfacing his research in an interdisciplinary area that covers tribology, surface chemistry and semiconductor materials.